EVALUATION OF COMPACT POLARIMETRIC SAR DATA OVER DUAL-POL AND QUAD-POL FOR CLASSIFICATION OF LAND TARGETS

Submitted in partial fulfillment of the requirements for the award of the degree of

Doctor of Philosophy

by

Kiran Dasari

(Roll No. 701425)

Supervisor

Prof. L. Anjaneyulu

Department of ECE, NIT Warangal

DEPARTMENT OF ELECTRONICS AND COMMUNICATION ENGINEERING

NATIONAL INSTITUTE OF TECHNOLOGY

WARANGAL – 506004, INDIA

December (2020)

APPROVAL SHEET

This thesis entitled **“Evaluation of Compact Polarimetric SAR Data over Dual-Pol and Quad-Pol for Classification of Land Targets”** by **Mr. Kiran Dasari** is approved for the degree of **Doctor of Philosophy**.

Examiners

____

____

Supervisors

Prof. L. Anjaneyulu

Department of ECE, NIT WARANGAL

Chairman

Prof. L. Anjaneyulu

Head, Department of ECE, NIT WARANGAL

Date:

Place:

DECLARATION

This is to certify that the work presented in the thesis entitled **“Evaluation of Compact Polarimetric SAR Data Over Dual-Pol And Quad-Pol For Classification of Land Targets”** is a bonafide Work done by me under the supervision of **Prof. L. Anjaneyulu** was not submitted elsewhere for the award of any degree.

I declare that this written submission represents my ideas in my own words and other’s ideas or works have not been included, I have adequately cited and referenced the original sources. I also declare that I have adhered to all principles of academic honesty and integrity and have not misinterpreted or fabricated or falsified any idea/data/fact/source in my submission. I understand that any violation of the above will be a cause for disciplinary action by the Institute and can also evoke penal action from the sources which have thus not been properly cited or from whom proper permission has not taken when needed.

Kiran Dasari
Roll No: 701425

Date:

Place:

Department of Electronics and Communication Engineering

National Institute of Technology

Warangal Telangana State-506004, India

CERTIFICATE

This is to certify that the thesis entitled **“Evaluation of Compact Polarimetric SAR Data Over Dual-Pol And Quad-Pol For Classification of Land Targets”** which is being submitted by **Mr. Kiran Dasari (Roll No: 701425)**, in partial fulfillment for the award of the degree of Doctor of Philosophy to the department of Electronics & Communication Engineering of National Institute of Technology Warangal, is a record of bonafide research work carried out by him under our supervision. To the best of our knowledge, the work incorporated in this thesis has not been submitted elsewhere for the award of any degree.

Prof. L. Anjaneyulu (Supervisor)
Department of Electronics and Communication

Date:

Dedicated to

Late Jyostna, Late Beulah,

Father Syamarao, Mother Elizabeth,

Wife Mercy Joy Kiran and

Brother Praveen Dasari

Contents

ACKNOWLEDGMENT

This thesis would not have become a reality without my **LORD JESUS CHRIST** and I would like to extend my sincere gratitude to all of them who encouraged me, and continuously supporting me.

First, I would like to express deep and sincere gratitude to my supervisor Prof. L.Anjaneyulu for his decisive guidance, kindness and constant encouragement throughout this PhD study and research. His enthusiasm, friendly accessibility and never-say-give-up attitude has been a constant source of inspiration for me to put up my best in research. Under his guidance I not only learnt how to do research but also learnt many approaches in life. I could not have imagined having a best advisor and mentor in my Ph.D. study and even in this pandemic situation. He has been a source of motivation, inspiration, enlightenment and encouragement. He is responsible for making the period of my research work as an educative and enjoyable experience.

I acknowledge my deepest gratitude to all the members of my doctoral committee for their valuable comments on my thesis work. I sincerely thank Prof .Sydulu, Prof. D.Srinivasacharya and Dr.V.V Mani for their kindness and valuable suggestions.

I thank scientists of ISRO (SAC/NRSC/IIRS) Shri A.V.V. Prasad, Smt. M. Jayasri, Smt. Sita kumari, Shri Srikant, NRSC, ISRO for guiding me technically and also during SAR data purchase.

I thank European Space Agency (ESA) for conducting online courses (Echoes in Space) and tutorials, webinars and also for conducting workshops.

I Thank Dr. Venu Madhav, Dr. Siva Prasad Nandayala, Dr. Sulakshana, Dr. M.Ranjeeth, Dr. M.Ellison, Dr. B.Shravan, for their continuous support, help and motivation. And I also thank my co-scholars B. Pranitha, R. Swetha, M. Sandhya for their help and support for carrying out my research work.

In my early days of Ph.D., I was very fortunate to meet Late. Prof. Wolfgang-Martin Boerner, a stalwart of our field who motivated me to work on Hybrid Polarimetry.

Every evening during the conference we used to have a long conversation regarding the SAR polarimetry. As a beginner I used to ask many questions but Prof Martin Boerner was very kind enough to answer all my queries with patience.

In 2019, I got a chance to visit the world-renowned European Space Agency (ESA) with the support and sponsorship of my supervisor Dr. L. Anjaneyulu. There I met Prof. Dr. Hab. Eric Pottier, whose books and articles have inspired me as a researcher.

I express my gratefulness to every person who has been instrumental in making my Ph.D. journey a memorable one. I would also like to thank ESA, JAXA, CSA, DLR, NASA, and ISRO for providing valuable data for my research. I would also like to acknowledge the financial support from MHRD, Govt. of India for funding towards my doctoral studies.

I would also like to acknowledge the financial support from the institute (Director), Prof.Anjaneyulu and other administrative staff for funding a European Space Agency Conference, Italy.

I would like to thank my cousin Mr. Prem Kumar for his guidance in collecting the ground truth data.

I am thankful and blessed for my brother Mr. Praveen, Dr. Dilip, K. kreeshna, G. Solomon for taking care of my parents in my absence.

I am very thankful to K. atha Devi for taking care of me and also Dr. V. Rama for her encouragement.

ABSTRACT

Earth Observation (EO) from space has been recognized as an invaluable way of monitoring the Earth. Today the necessity of Earth Observation Missions has increased rapidly due to its wide applications in many fields. Using EO systems, one can monitor Earth’s climate change, ocean surfaces, disaster management, mapping, land usage (such as agriculture, urban, and forestry). Particularly, Earth Observation using Synthetic Aperture Radar (SAR) is gaining importance due to its all-weather capability and day-night acquisitions. For continuous monitoring, SAR systems require a huge amount of storage, higher transmission power, and larger swath width. SEASAT, the first-ever civilian space-borne radar remote sensing system, was launched by NASA/JPL, in the year 1978. Depending on the type of polarization of signals these radars use for transmission and reception, they are known to be operating in full polarimetry, single polarimetry, dual polarimetry, and compact polarimetry modes. From the earlier studies, it is known that the performance of fully polarimetric SAR systems is the highest in the SAR application due to its complete radar target information content. However, Fully Polarimetric SAR systems have half the swath width, requires double the transmitting power, and complex architecture when compared to single and dual-polarized SAR systems.

Compact Polarimetry (Hybrid Polarimetry) has gained significant importance in recent years among other earth observation missions due to its low power consumption, simple architecture, and larger swath width. For Space-based SAR systems, these parameters are vital to monitor the earth's surface continuously for various applications. Therefore, many International Space Agencies such as Canada Space Agency (CSA), Japan Aerospace Exploration Agency (JAXA), National Aeronautics and Space Administration (NASA), European Space Agency (ESA) and Indian Space Research Organization (ISRO) are interested to implement Hybrid polarimetry modes in their upcoming missions. Compact polarimetry offers a tradeoff with fully polarimetric systems in terms of swath width, power, architecture, budget, and information content. Initially, Compact polarimetry data was used for Lunar and Planetary explorations such as Mini SAR (Chandrayaan-1) mission and Mini-RF (Lunar Reconnaissance Orbiter) mission. RISAT-1 was the first space-borne EO mission with Hybrid Polarimetry and was launched by ISRO in 2012. The main difference of Hybrid polarimetry from fully polarimetric systems is transmitting a circularly polarized signal towards the target and receiving the linearly polarized returns.

In this research, the performance assessment of Compact Polarimetry (Hybrid Polarimetry) over dual-pol and quad-pol data for land cover classification, urban land cover, and crop classification has been attempted. Evaluation of hybrid polarimetry was done on various ground targets such as agriculture land, forest land, urban land, and semi-urban land, over dual polarimetry, and quad polarimetry data. Speckle filtering is performed over the datasets using various polarimetric speckle filters. A comparative study of different polarimetric speckle filters with variable window size and the impact of their selection from the point of view of edge preservation, information content, and classification has been done. To understand the scattering mechanism of the targets, target decomposition theorems such as three-component Freeman-Durden, four-component Yamaguchi decomposition, Raney decomposition, Pseudo Three-Component decomposition, m-delta, and m-chi decompositions were performed on the SAR datasets. The m-chi decomposition has proven to be robust when the transmitting component is not perfectly circularly polarized. A comparative study among the different modes of compact polarimetry was performed, hybrid-pol mode gave good results for various ground targets. The C-band hybrid polarimetry data and dual polarimetry linear data are also compared to study the response of circular transmission over a linear transmission from the target. It is observed that the transmitted circular component interaction with targets gave more detailed information than transmitting a linear component. The penetration capability of microwave frequencies using C-band, and L-band into the targets has also been studied, and it was observed L-band hybrid polarimetry gave more accuracy than C-band hybrid polarimetry data.

Support Vector Machine (SVM) classifier, and Wishart classifier, and other machine learning algorithms were used to classify the datasets. SVM classifier gave good results when compared to Wishart classifier on Hybrid pol data. The datasets were compared using three different SVM kernel parameters, i.e., Radial Basis Function (RBF), Polynomial with degree '2', and Linear. It is observed that SVM with RBF kernel parameter gave the highest Overall Accuracy (OA) of 92.34% for hybrid-Pol RISAT-1 data. Similarly, SVM with RBF kernel parameter gave an Overall Accuracy (OA) of 76.83% for dual-Pol RISAT-1 data. The results obtained from a comparative study of dual-pol vs hybrid pol RISAT-1 are very promising. The OA of Hybrid-pol data was 83.03% and for dual-pol, data was 54.75%. A wide variety of datasets with different areas of interest have opted for this study to evaluate the hybrid pol data over dual and quad pol data. Using SVM classifier the OA of Hybrid pol data on an urban area, was the best recorded to OA 84.10 %. To compare the information content and target penetration capability, C-band RISAT-1(Hybrid-pol) data and L-band Alos Palsar-2 (quad-pol) have opted in this study. It is observed that Hybrid-pol data gave almost similar accuracy to that of quad pol data. The evaluation of data was performed using the confusion matrix for accuracy assessment. For validating the results, after the classification, the images are compared with the optical imagery, Google Earth, and In-situ information that was collected synchronously to the satellite pass.

This study was initiated to compare the information content of Compact-pol (Hybrid-pol) over dual-pol, pseudo-quad-pol, and quad-pol datasets and also to improve the overall accuracy using machine learning algorithms for accuracy assessment. From the overall study, it was recorded that hybrid pol data gave very good results when compared to linear dual-pol data and almost the same to that of quad- pol data. Few studies in the literature exclusively on Hybrid-pol data were reported only to (80-85) % accuracy. The SVM classifier was not used for classification in the literature. The majority of the work carried on Hybrid-pol were simulated from quad pol data. In this study, original hybrid pol data from RISAT-1 has been used.

For this research, six SAR datasets viz., RISAT-1, Alos Palsar-1, Alos Palsar-2, Radarsat-2, Sentinel-1A, Sentinel-1B and three optical datasets (Resourcesat-2, Landsat-8, and Sentinel-2) and In-situ data are used. Quad-pol, Compact-pol, and Dual-pol datasets are also used in this study. RISAT-1 Hybrid-pol data, RISAT-1 Dual-pol data, RISAT-1 Quad-pol, and Resourcesat-2 datasets have been purchased from NRSC/ ISRO, Hyderabad and other datasets are obtained from (ESA) and (JAXA). A combination of SAR missions and polarimetry were selected upon the study requirement. Optical datasets were used as a reference and also compared for the evaluation of SAR datasets.

The research outcome has been published in the journal related to the subject of research. Very few studies with results have been reported in the literature on the performance of Compact polarimetry data over dual and quad pol data. These results will fill the gap in the literature to some extent.

Keywords: Earth Observation, Synthetic Aperture Radar, Compact Polarimetry, Hybrid polarimetry, Circular transmission, Land cover classification, SVM classifier.

LIST OF FIGURES

LIST OF TABLES

List of Abbreviations

ASAR	Advanced Synthetic Aperture Radar
ASF	Alaska Satellite Facility
AirSAR	Airborne SAR
ALOS	Advanced Land Observing Satellite
CP	Compact Polarimetry
CL	Circular-Linear
CP	Compact Polarimetric
CTLR	Circular Transmit Linear Receive
CSA	Canadian Space Agency
dB	Decibel
DEM	Digital Elevation Model
DCP	Dual Circular Polarimetry
DLR	German Aerospace Center
DoD	Degree of Depolarization
DoP	Degree of Polarization
ENL	Equivalent Number of Looks
ESA	European Space Agency
GRD	Ground Range Multi-Look Detected
GSFC	Goddard Space Flight Center
GeoTIFF	Geographic extensions to the Tagged Image File Format
HH	Horizontal-Horizontal
HV	Horizontal-Vertical
IEEE	Institute of Electrical and Electronics Engineers

ISPRS	International Society for Photogrammetry and Remote Sensing
JAROS	Japan Resources Observation System Organization
JAXA	Japan Aerospace Exploration Agency
JPL	Jet Propulsion Laboratory
LIDAR	Light Detection and Ranging (system)
MDA	MacDonald, Dettwiler and Associates Ltd.
ML	Maximum Likelihood
NASA	National Aeronautics and Space Administration
PRF	Pulse Repetition Frequency
PALSAR	Phased Array type L-band SAR
PolSAR	Polarimetric SAR
RCM	RADARSAT-2 Constellation Mission
RCM	RADARSAT Constellation Mission
RH	Right circular transmit and Horizontal receive
RL	Right circular transmit and Left circular receive
RMSEs	Root Mean Square Errors
RR	Right circular transmit and Right circular receive
RV	Right circular transmit and Vertical receive
SAR	Synthetic Aperture Radar
SIR	Space-borne Imaging Radar
SGF	SAR Georeferenced Fine product (also known as Path Image)
SGX	SAR Georeferenced Extra product (also known as Path Image Plus)
SLC	Single Look Complex product
USGS	United States Geological Service

TIFF	Tagged Image File Format
UAVSAR	Uninhabited Aerial Vehicle Synthetic Aperture Radar
VH	Vertical-Horizontal
VV	Vertical-Vertical
WGS	World Geodetic System
WGS84	World Geodetic System Revision 84

Chapter 1

Introduction

1.1 Earth Observation

Earth observation missions are designed to continuously monitor the earth to monitor the environment, land surface, biosphere, solid Earth, atmosphere, and oceans. The first earth observing satellite (Sputnik-1) was launched on October 4, 1957, by the Soviet Union [1]. Explorer-1 was the first American satellite launched by NASA on January 31, 1958 [2]. Indian Space Research Organization (ISRO) has launched many Earth-observing (EO) satellites since 1979, beginning with Bhaskara - I, as it was the first experimental remote sensing satellite built by ISRO [3]. Indian Remote Sensing Satellite (IRS-1A) was the first series of indigenous remote sensing satellites launched into orbit on March 15, 1988. As of today, ISRO has launched 30 (27 optical and 3 Radar) Earth Observation missions and also has the largest constellation of remote sensing satellites in operation [4]–[5]. Earth-observing satellites are mainly used for remote sensing purposes to monitor the earth continuously. Satellites with optical sensors were providing the data from the past three decades with limitations.

1.1.1 Microwave Remote Sensing

Remote Sensing is the art and science of acquiring information without any physical contact. EO missions use remote sensing techniques to capture and analyze the Earth's terrain continuously using Space-borne satellites. Remote Sensing is categorized into two parts: 1) Passive Remote Sensing, 2) Active Remote Sensing. Passive Remote Sensing uses the sun as the source of illumination and captures the return radiance response onboard. Active remote sensing uses its source of illumination without depending on the sun as a source of energy [6]. Passive remote sensing uses optical cameras and scanners for imaging. Common passive sensors are Landsat-7, Geo Eye, Quick Bird, Ikonos, and IRS. Active remote sensing uses RADAR, SONAR, and LIDAR to capture the earth's surface. Alos palsar-2, Radarsat-2, Sentinel-1 are the commonly used Active sensors. Remote sensing can be performed on various platforms such as spacecraft, aircraft. In remote sensing, the resolution depends on the sensor's height; the higher the height lower the resolution [7].

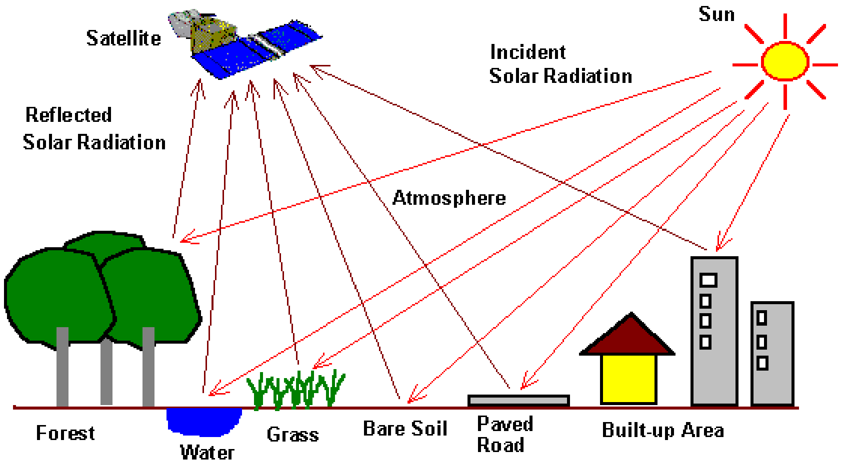

Fig 1.1 Illustration of Optical Remote Sensing ©CRISP2001

In Optical remote sensing, the sun is the source of illumination. The sensors on the satellite make use of visible, near-infrared, and short wave infrared rays to form the images of the earth's surface by detecting the reflected solar radiation from the targets (water, forest, grass, building, and bare soil) on the ground as shown in Fig 1.1. The sensors mounted on the satellite can image only in daylight and in perfect weather conditions with limitations.

In Microwave Remote sensing, sensors use the microwave region of the electromagnetic spectrum. The sensor in microwave remote sensing is called an antenna. RADAR is an acronym for RAdio Detection and Ranging. RADAR is a type of antenna which can transmit and receive the electromagnetic signal from the targets. RADAR uses the microwave region of the electromagnetic spectrum from P-band (0.3 GHz) to K_a-band (40 GHz) to transmit and receive, as shown in Figure 1.2. The Development of RADAR took place during World War II for navigation and target location. Imaging radars are operated in the range of 1mm to 1-meter wavelength, as longer wavelengths improve signal penetration through the atmosphere and clouds [9]. In the microwave, remote sensing resolution is independent of the sensor mounted altitude but dependent on the length of the antenna. The longer the antenna length, the greater the resolution, but practically it is difficult to deploy a longer antenna into space [7].

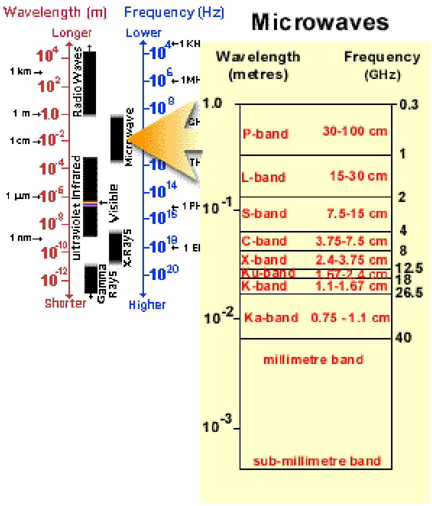

© CCRS / CCT

Fig 1.2 Electromagnetic spectrum Canada Centre for Remote Science © (CCRS)

1.1.2 Why Microwaves for Remote Sensing

Microwaves can penetrate through clouds and, to an extent, rain. Microwaves do not rely on sunlight as a source of illumination. These attributes allow sensing the earth's surface independently of the day and almost in all weather conditions [8]. Microwaves can penetrate through vegetation, soil, ice than optical waves. Longer microwave penetrates much better than shorter wavelengths, as shown in Figure

1.3, the most crucial reason for the use of microwaves is the information content available is different from visible and infrared regions of the electromagnetic spectrum.

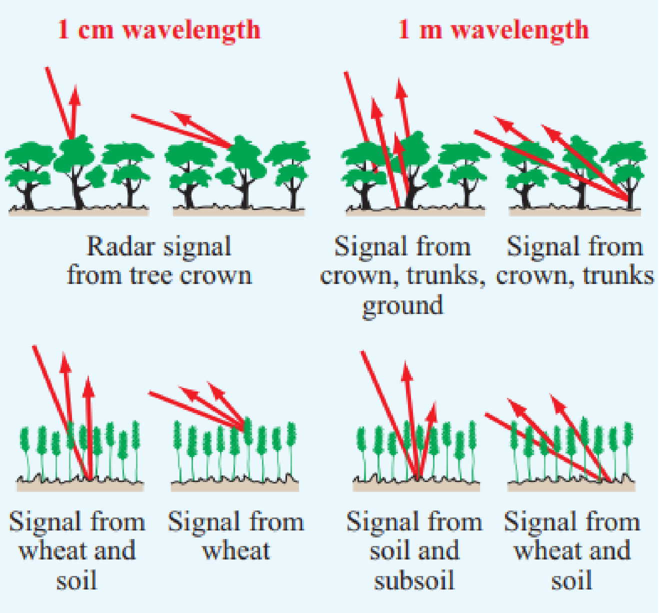

Fig 1.3 Radar signal penetration for different wavelengths

1.1.3 Advantages and disadvantages of Microwaves Remote Sensing over Optical Remote Sensing

Advantages	**Disadvantages**
Nearly all-weather capability	The Information content is different from Optical
Day or Night capability	Difficult to interpret the information
Penetration through vegetation Canopy	Speckle effects
Penetration through soil	Topographic effects
Minimal Atmospheric effects	
Sensitivity to dielectric properties of the target	
Sensitivity to structure of the targets	
Unique Sensitivity to moisture content of the target	
Unique Sensitivity towards the orientation of the target	

Table 1.1- Advantage and disadvantages of Microwave Remote sensing

1.2 Overview and History of Microwave Remote Sensing

P-band, L-band, S-band, C-band, and X-band are the frequently used microwave bands for imaging. Active microwave sensors are categorized into imaging and non-imaging sensors. Altimeters and scatter meters are the non-imaging sensors. Imaging Radar is operated in two platforms a) Airborne platform b) Space-borne platform. From these platforms, RADAR can be used in nadir looking, Side looking. Real Aperture Radar (RAR) is an example of nadir looking sensors. Side Looking Airborne Radar (SLAR) and Synthetic Aperture Radar (SAR) are examples of side-looking sensors.

1.2.1 Imaging Radar

James clerk Maxwell (1831-1879) provided the fundamental mathematical descriptions of the magnetic and electric fields associated with electromagnetic radiation. In the year 1886, Hertz demonstrated the transmission of Radio microwaves and reflections from various objects. Hertz also studied the interaction of radio waves with a metallic surface. Based on the fundamental physics principles discovered by Maxwell and Hertz, M. Marconi (1874 -1937) constructed an antenna that transmitted and received radio signals. A.H Taylor and L.C investigated RADAR. Young in the year 1922. RADAR was initially used to detect targets such as ships and aircraft, both friendly and enemy. In 1935, Young and Taylor and Sir Robert Watson-Watt independently combined antenna transmitter and receiver in the same instrument. These advancements in RADAR laid the ground-work for the development of RADAR in World War [9].

The imaging radar's origin came from the first airborne scanning radar system, H2S, developed by the Royal Air force Bomber Command during World War II. It helped to identify the targets on the ground surface in all weather and even through clouds. The critical development was to use high frequencies long antennas capable of producing narrow beams projecting sideways from the aircraft. This resulted in extensive coverage by scanning along the flight path known as Side Looking Airborne Radar (SLAR). In 1952, the critical development of the technique "Doppler beam sharpening" took place in the Goodyear Aircraft Corporation by Carl Wiley. In the mid-1960s, there are two types of SLAR: Real Aperture Radar and Synthetic Aperture Radar.

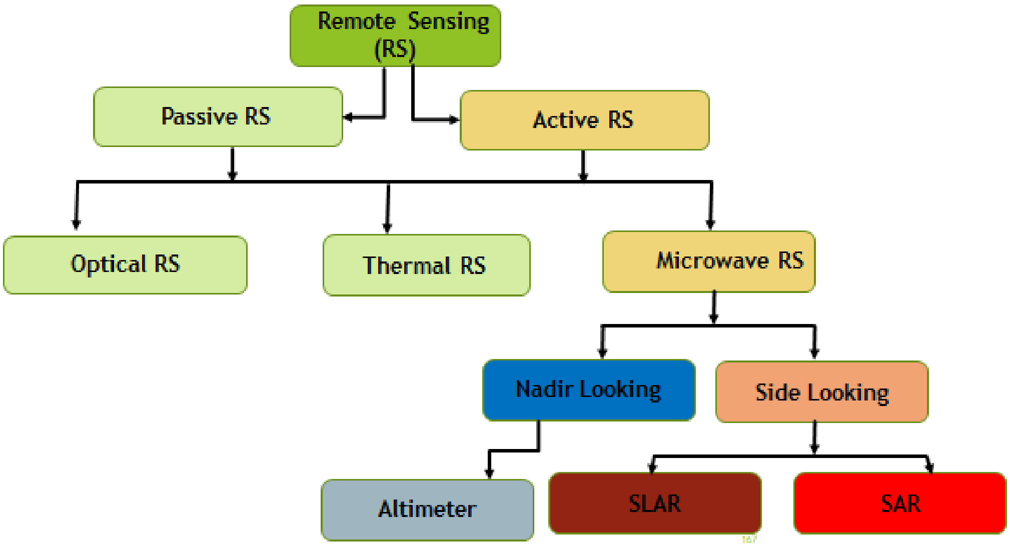

Fig 1.4 Family of Remote Sensing

1.2.2 Radar Image construction

The Radar instrument is placed on a spacecraft/aircraft and pointing the antenna sideways, i.e. tilting the antenna with a viewing angle as shown in Fig 1.5. The basic idea was to introduce to make spatial measurement of the backscattered signal from the target using a scatterometer. The distance on the ground is related to the time delay of the backscatter. Thus the construction of a two dimensional image is generated by utilizing the motion of the radar antenna to scan the earth surface along with the motion of the sensor.

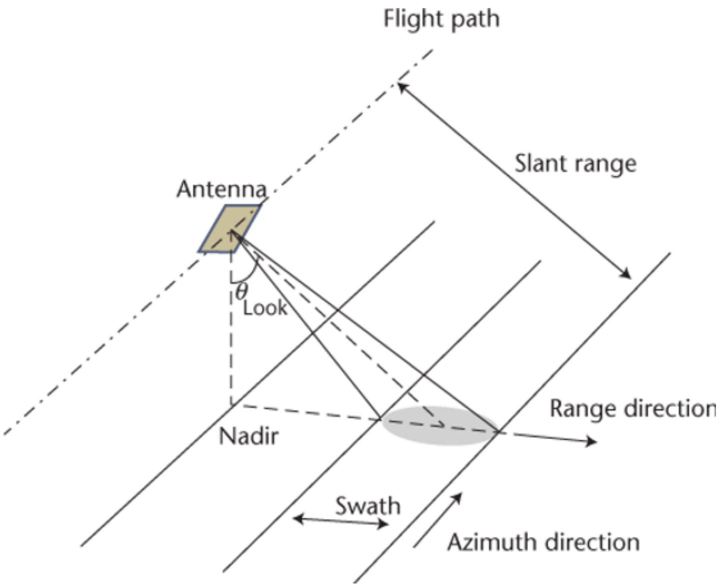

Fig 1.5 Radar Imaging Geometry © NASA

Azimuth Direction: The direction in which Flight is travelling.

Near Range: Minimum distance between target and antenna.

Far Range: Maximum distance between target and antenna.

Range Direction: Antenna beam direction from near range to far range

Nadir: Perpendicular direction to the flight path

Swath: Distance between near range and far range

Incidence angle: Angle to nadir.

Radars are classified depending upon their look direction

a) Nadir Looking
b) Side Looking

In Nadir looking, the antenna is placed perpendicular to the flight path, as the footprint is circular the range between near range and far range will be the same. But in side looking, the antenna is tilted towards the flight direction shown in Figure 1.6.

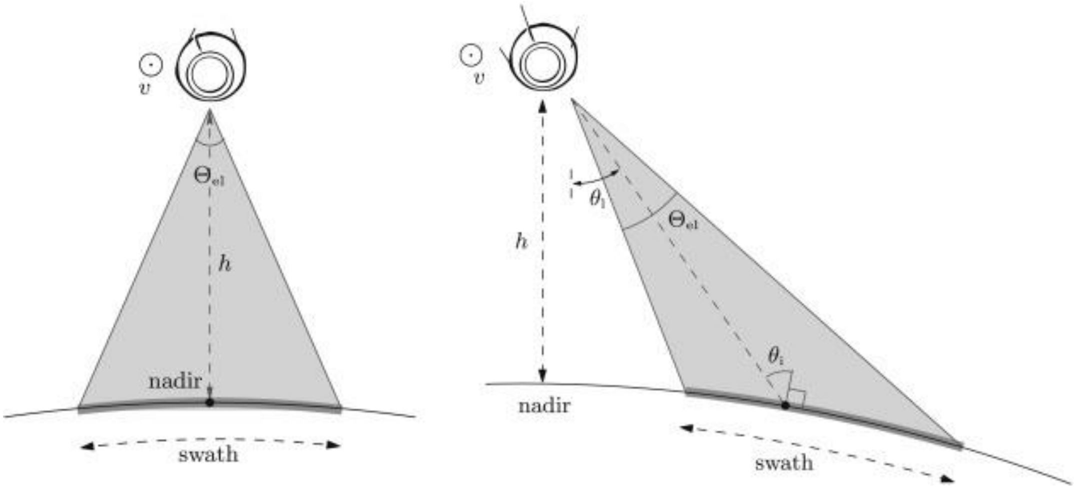

Fig 1.6 Nadir looking Radar and Side looking Radar

1.3 Synthetic Aperture Radar (SAR)

Synthetic aperture radar (SAR) is one of the most advanced engineering inventions in the twentieth century. SAR is a powerful remote sensing tool. The idea of SAR was initially mentioned in a Good year Aircraft report by Carl.A.Wiley in the year 1951 and was put into operation in early 1952 [10]. A SAR is an active sensor that first transmits a microwave signal and returns the backscattered signal from the earth's surface. In general, the larger the antenna's size, the unique information can be obtained by the SAR scientist. The more information, the better the image resolution. The space-borne or the airborne platform should deploy the larger antenna (10 m) to obtain better resolution. But, practically deploying such a larger antenna is infeasible. The scientist, therefore, used the motion of the spacecraft, along with the advanced signal processing techniques they simulated a larger antenna. Microwave imaging (Microwave Remote Sensing) 's motivation came from its unique features such as weather independent, day and night imaging capability, geometric resolution independent of the distance, penetration of radar waves through atmosphere, clouds, vegetation, and even though the soil. SEASAT was the first-ever civilian spaceborne radar remote sensing system launched by NASA/JPL in 1978. Later, few SAR missions such as ERS-1, 2 from Europe, JERS-1 from Japan, and Radarsat-1 from Canada were launched in the '90s and proved the potential of SAR Remote Sensing [11].

1.3.1 SAR Principle

SAR transmits a radar pulse towards the target and reflects back the pulse towards the transmitter, which depends on the type of scattering. Suppose the scatter, the surface is smooth. In that case, the incident energy will be reflected away from the sensor. If the scattering surface is rough, then the incident energy will be diffused in all directions, and the sensor will receive only a part of the reflected power. The amount of backscattered energy depends on the properties of ground targets.

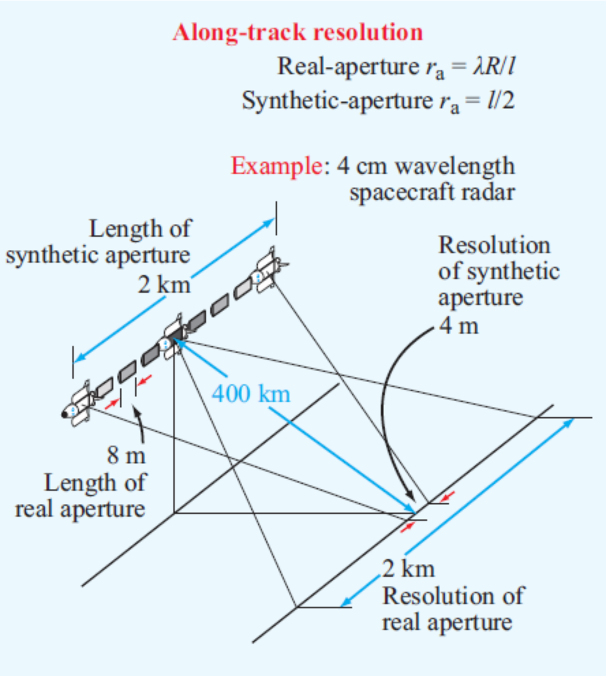

Fig. 1.7- Aperture Synthesis

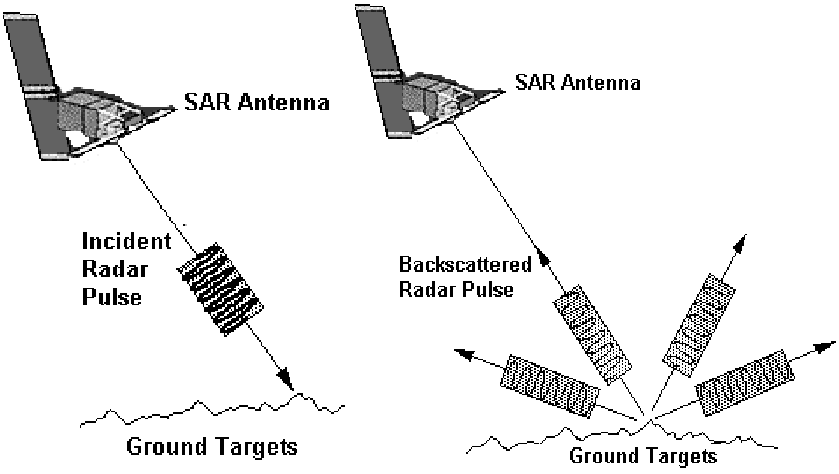

Fig 1.8 SAR principle © CRISP

1.3.2 Resolution

The capability of a sensor to discriminate the smallest object on the ground. In SAR, there are two types of resolution. 1) Range Resolution 2) Azimuth Resolution [12].

1.3.2.1 Range Resolution

To determine the spatial resolution at any point is a radar image, it is necessary to compute the resolution in two dimensions. Range and Azmimuth resolution. Radar is a ranging device that measures the distance to objects in the terrain using sending out and receiving pulses of active microwave energy. The range resolution in the across-track direction is proportional to the length of the microwave pulse. The shorter the pulse length, the finer the range resolution. Pulse length is a function of the speed of light multiplied by the duration of the transmission τ . The length of time that the microwave energy is transmitted is measured in microseconds and typically ranges from 0.4 -1.0microseconds and translates into a pulse length ranging from 8 – 210m. The pulse length must travel to the target and back to the sensor. Therefore it is necessary to divide by 2 to measure the slant-rang resolution. And to scale it to ground-range, it is multiplied by the cosine of the depression angle (γ).

Thus the equation for computing the range resolution is:

$$R_r = \frac{\tau \cdot c}{2\cos\gamma} \tag{1.1}$$

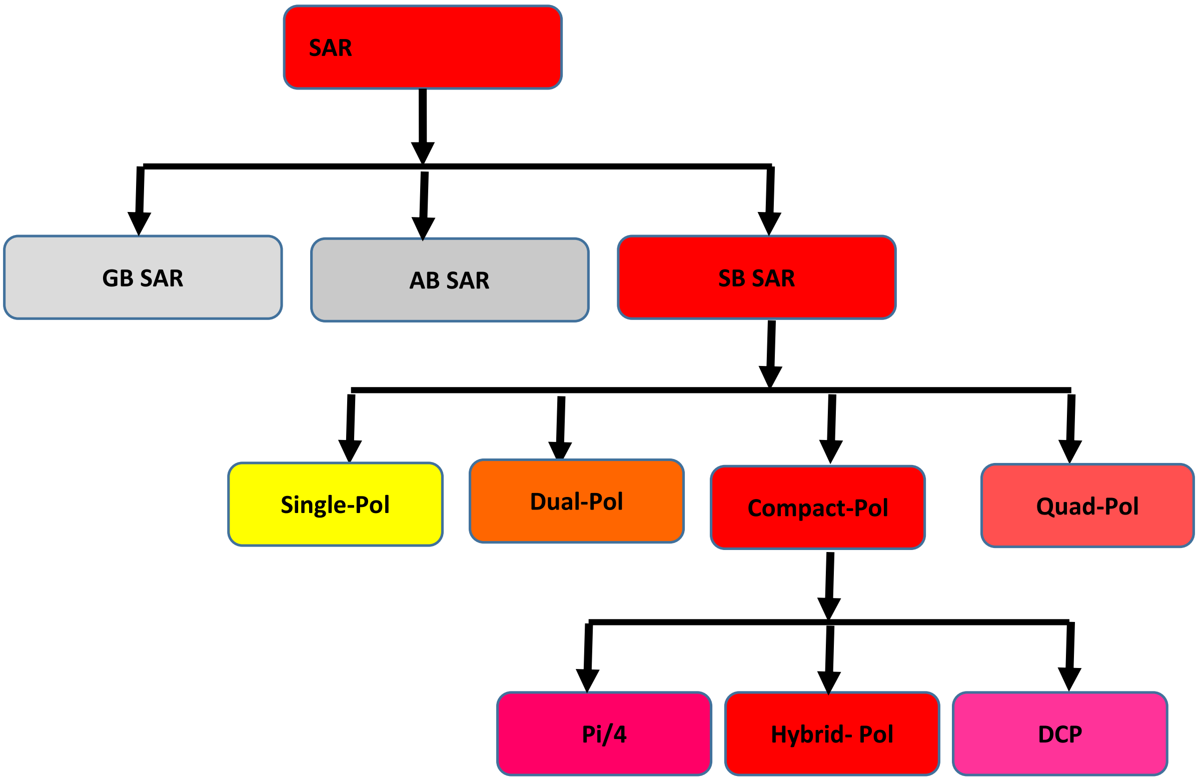

Fig 1.9 Family of Synthetic Aperture Radar

1.3.2.2 Azimuth Resolution

Thus far, we have only identified the length in meters of an active microwave resolution element at a specific depression angle and pulse length in the range direction. To know both the resolution element's length and width, we must also compute the width of the resolution element in the craft flying direction. Azimuth resolution (R_a) is determined by computing the terrain strip's width that is illuminated by the radar beam. Real aperture active microwave radars produce a lob-shaped beam.

$$R_a = \left(\frac{H}{\sin\gamma}\right)\frac{\lambda}{L} \tag{1.2}$$

1.4 Radar Polarimetry

It is a science of acquiring, processing, and analyzing the polarization state of an electromagnetic field. The polarization information contained in the backscattered wave from a given medium is related to its geometrical structure, reflectivity, shape, and orientation. There are four types of polarization 1) Single polarization, 2) Dual polarization, 3) Quad polarization 4) Compact polarization. In general, a single pol system transmits and receives only one polarization, viz. horizontal (H) or vertical (V). Similarly, a dual-pol SAR transmits one polarization and receives the backscatter in a pair of orthogonal polarization viz. transmit (H) and receives (H, V) vice versa. In quad-pol SAR, two orthogonal polarizations H and V, are coherently transmitted and received. In compact polarization, one linear polarization is transmitted, and two mutually coherent circular polarization is received. Complete polarimetric scattering information can be obtained from the target from quad-pol SAR, and hence, better analysis and classification can be performed.

1.5 Scattering mechanism

They are four types of scattering mechanisms 1) Specular 2) Surface 3) Double bounce 4) Volume scattering.

Specular

When a radar signal is transmitted on flat terrain, the reflection angle is the same as the incidence angle; it is called specular reflection. These areas in the radar image appear very dark, e.g., smooth water body or tarmac.

Surface scattering

When a radar signal hits on a rough surface, some energy will be backscattered to the sensor. Example: vegetation, bare soil.

Double Bounce

When the radar pulse hits to smooth surface that is perpendicular to each other, the returned signal will be strong and appears brighter in a SAR image. Example: Buildings and manmade structures.

Volume Scattering

When a man's radar pulse hits a three-dimensional body, the energy gets reflected multiple times in multiple directions. Examples are dense snow, forests.

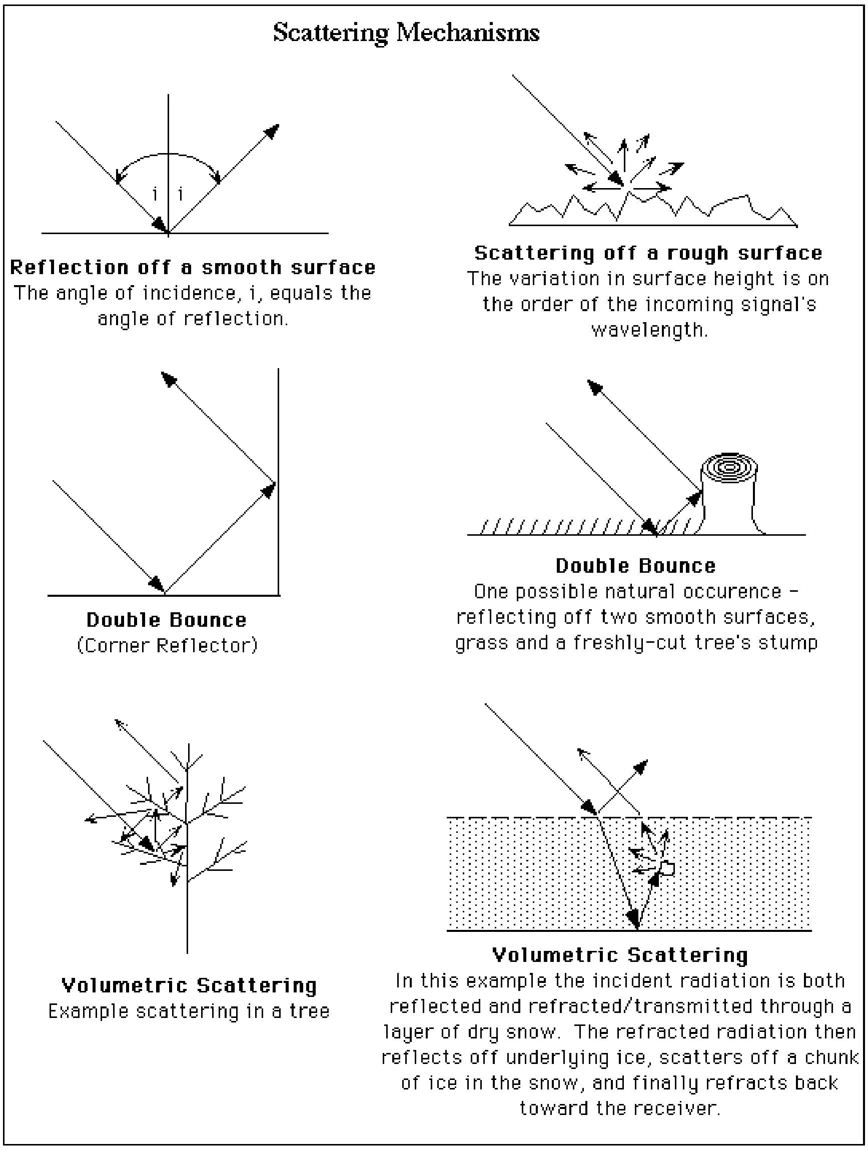

Fig 1.10 Scattering Mechanism © esa

1.6 Motivation

Earth Observation (EO) Missions are meant for continuous monitoring, and thus the SAR systems require a huge amount of storage, higher transmission power, and larger swath width. SAR systems can image the Earth during rainy seasons and in the absence of sunlight, which is an advantage over traditional optical imaging systems. Therefore the data can be well utilized in disaster management. Generally, dual-pol SAR and quad-pol SAR are used for EO Missions. The dual-pol SAR cannot give more information than the quad-pol SAR, and the quad-pol SAR consumes a huge amount of energy with less swath width and complex architecture. Compact polarimetry offers a tradeoff with fully polarimetric systems in terms of swath width, power, architecture, budget, and information content [13]. Compact polarimetry (Hybrid-pol) 's main difference from fully polarimetric systems is transmitting a circularly polarized signal towards the target and receiving linearly polarized returns [14]. While transmitting a circular component, ionosphere interaction will be reduced. RISAT-1 was the first EO mission built on Hybrid-pol

Architecture; therefore, original Hybrid-pol RISAT-1 data was used in this study [15]. It was compared to dual-pol and quad-pol data in the literature to explore the performance of simulated Compact-Pol data. All the studies so far performed on Hybrid-pol were simulated from quad-pol data [16]. This motivated us to investigate the performance of original Hybrid-pol data over dual-pol and quad-pol data. In the literature, a Comparison of Dual-pol and Hybrid-pol has been made using the data from different missions. The availability of Dual-pol and Hybrid-pol data from the same RISAT-1 mission with the exact resolution made us work on this topic. To compare the penetration capability, Alos palsar-2 (L-band) data and RISAT-1 (C-band) data have opted on the standard test site Sanfransico city.

Parameter	Launch date	Country	Wavelength, cm	Incident Angle	Polarization	Azimuth resolution	Range resolution	Swath width, km	Altitude km
SEASAT	June 26, 1978	USA	L-(23.5)	[23^0]	HH	25	25	100	800
SIR-A	Nov 12, 1981	USA	L-(23.5)	[50^0]	HH	40	40	50	260
SIR-B	Oct 5, 1984	USA	L-(23.5)	[15^0-64]	HH	17-58	25	10-60	225 and 350
SIR-C/X-SIR	April 1994 Oct 1994	USA	X-(3.0) C-(5.8) L-(23.5)	[15^0-55^0]	HH, HV, VV,VH	30	10-30	15-90	225
ALMAZ-1	March 31, 1991	Soviet Union	S-(9.6)	[30^0-60^0]	HH	15	15-30	20-45	300
ERS-1,2	1991 1995	Europe	C-(5.6)	[23^0]	VV	30	26	100	785
JERS-1	Feb 11, 1992	Japan	L-(23.5)	[39^0]	HH	18	18	75	568
RADARSAT-1	November 1995	Canada	C-(5.6)	[10^0-60^0]	HH	8-100	8-100	50-500	798
ALOS PALSAR-2	May 2014	Japan	L-(22.9)	[8-70^0]	HH, HV, VV,VH	4.3	5.1	70km	691
RADARSAT-2	Dec 2007	Canada	C-(5.6)	[20-45^0]	HH, HV, VV,VH	3-80	1-100	18-500	798
RISAT-1	April 2012	India	C-(5.6)	[26.35^0]	RH, RV HH-HV	2.34	3.33		540

Table 1.2 Earth Observing (EO) SAR Missions

1.7 Literature Survey

This chapter presents a detailed literature survey on the Speckle filtering, the target decomposition theorems and classification algorithms, compact polarimetry with existing state-of-art methods for processing and analyzing SAR images. We also discuss the literature around partial polarimetry. The author has collected ten base research articles

The concept of dual partial polarimetric mode was proposed by Je Souyris et al., the authors have assessed the performance of SAR compact Polarimetry architectures based on mixed basis measurement, i.e., transmitting polarization is either circular or oriented at an angle of 45°, and the receiver is at horizontal or vertical polarization. The performance is assessed in two folds: the first is concerned about the information content preserved with comparing to FP SAR, and the second is to address the space implementation complexity in terms of swath width, power budget, calibration, and ionospheric effects. Because of the mismatch between transmitter and receiver bias, the power budget is deteriorated by a factor of 3dB [17].

Raney was the first person to build the Hybrid-Polarity SAR architecture on a space-borne platform. In this, SAR transmits only one circular polarization and receives two mutually orthogonal linear polarizations. The author has introduced the m-delta decomposition technique in this paper. This paper's objective is full characterization and exploitation of backscattered response with a monostatic radar that transmits in one polarization is invariant to geometrical orientations in the scene. The Stokes parameters require measuring the relative phase, and the amplitudes of the received backscattered signal. The Hybrid-pol architecture minimizes sensitivity to relative errors, crosstalk, and optimizes relative phase and amplitude calibration. This architecture requires less RF hardware, less weight with fewer losses. The Hybrid-pol architecture systems will be an alternative for Earth Observations missions and a prime architecture for extraterrestrial missions. The study has demonstrated that hybrid-pol systems provide double swath width and less transmission power with simple architecture over quad-pol systems [13].

Michael E Nord, Thomas l, Ainsworth et al., (2009), the authors have compared the three compact polarimetric modes. The authors have studied different transmit/receive configuration to determine which configuration allows for superior construction of full polarimetric data. The authors have noted that DCP and CLTR modes are related via bias change on the received signal. The authors have opted for L-band E-SAR data and simulated compact polarimetric modes. The single linear transmit will not excite returns from linear oriented structures, causing loss of polarimetric information. While transmitting a circular component misses some helical structure, which is less compared to a linear structure [18].

T.L Ainsworth, J.P.Kelly, J.S.Lee (2009), et al. Presented a study of the polarimetric information content of dual-pol imaging modes and dual-pol imaging extended by polarimetric scattering models. The authors have compared with Wishart classification on both partial polarimetric and full quad-pol datasets. In this study, NASA/JPL AIRSAR L-band airborne SAR data was used for the Flevoland region and L band E-SAR imagery of Oberpfaffenhofen. The authors have concluded that quad-pol data gave the most accurate results while performing Wishart classification and dual-pol data gave the most unsatisfactory results. The compact-pol data and pseudo-quad-pol data are the intermediates between dual-pol and quad-pol data. From the results on the Flevoland image, quad-pol data gave 81.8% accuracy, dual-pol data gave 59.1% accuracy, compact-pol (Pi/4) data gave 80.9%, CLTR mode gave 81.8% accuracy, Pseudo quad-pol data (Pi/4) and CLTR gave 80.1%, and 73.5% accuracy respectively. From the results on Oberpfaffenhofen image, quad-pol data gave 97.5% accuracy, dual-pol data gave 96.1% accuracy, compact-pol (Pi/4) data gave 97.3%, CLTR mode gave 96.8% accuracy, Pseudo quad-pol data (Pi/4) and

CLTR gave 97.2% and 95.1% accuracy respectively. The Hybrid dual-pol modes (Pi/4 and CLTR) not always perform better for image classification than standard linear dual-pol transmission [19].

A SAR system with Compact-pol architecture transmits a circular component and receives two mutually orthogonal coherent linear components, which is one manifestation of Compact polarimetry. The authors have utilized Radarsat-2 full polarimetric data to simulate Compact polarimetry. A research team composed of various departments of the Government of Canada evaluated compact- pol mode for various applications. Besides, the study has demonstrated the potential of Compact-pol for ship detection, soil moisture estimation, crop identification, and sea ice classification. The Compact-pol system provided a wider swath than a quad-pol system with simple architecture [20].

Rajib Kumar Panigrahi & Amit Kumar Mishra have compared hybrid-pol data with quad-pol schemes on the airborne GTRI dataset. This paper describes the benefits of using a hybrid-pol scheme. The comparison was made based on the information content, and it was concluded that the information of hybrid-pol is found to be comparable to that of the quad-pol airborne SAR system. However, hybrid-pol is the optimum choice when there is a requirement of wide swath cover, low transmission power [16].

Rajib Kumar Panigrahi & Amit Kumar Mishra have presented a comparison of Hybrid-pol and quad pol synthetic Aperture data (SAR) data for information content. First, the Hybrid-pol data was converted to pseudo quad pol data using compact polarimetric scattering models. The scattering mechanism was evaluated using Freeman and Durden decomposition techniques. In this study, NASA/JPL AIRSAR L-band airborne SAR data was used for the Flevoland region. The authors have evaluated and compared the scattering contribution for clusters of the pixels in SAR images. The authors have concluded that the information content in pseudo quad pol is found to be comparable to quad pol data. Hybrid-pol data is the optimum choice when wider swath coverage and average transmitted power are the constraints [21].

Haldar, D., Das, A., Mohan, S., Pal, O., Hooda, R.S., and Chakraborty, M have evaluated L-band SAR data different polarization combinations, i.e., linear, circular, and Hybrid-polarimetric modes. The authors have opted for Alos-palsar full polarimetric data and simulated pi/4 mode and circular mode. The authors performed supervised classification using the maximum likelihood classifier on various polarimetric combinations. It has been observed linear full polarimetric mode gave an OA of (92%) followed by circular –full (89%), dual-circular (87%), hybrid-pol (7-75%), and linear dual-pol with (63-71%).The Hybrid-pol data with different modes found to be good for crop classification apart from fully polarimetric data [22].

Lardeux, C., Frison, P.L., Tison, C., Souyris, J.C, have addressed the potential of the SVM algorithm for classifying the polarimetric SAR data. The authors have used L-band, P-band, and C-band data in this study and have obtained an OA of 87%, 82%, and 99%, respectively. SVM classifier has recorded a great improvement of about 20% compared to Wishart classification [23].

Yekkehkhany, B., A. Safari, S. Homayouni, and M. Hasanlou have presented a comparative study on the classification of multi-temporal L-band SAR data using different SVM kernels. In this study, the authors have opted for kernel functions such as RBF, Linear, and Polynomial. RBF Kernel performed better than the other two kernels. They have concluded that using two data OA increased by 14%, and by using three multi-temporal data, OA increased by 5%. Moreover, the effect of multi-temporal data is expensive and time-consuming [24].

1.8 Research Objectives

The thesis deals with the three main applications of Microwave Remote sensing Viz. Land Use Land Cover, Urban Land Cover, and Crop Discrimination.

(i) The first objective is to draw the Importance of Speckle filtering and the impact of speckle filter window size on speckle reduction in SAR images.
(ii) The second objective is to characterize the ground targets of Compact polarimetry data using robust m-chi and m-delta decomposition.
(iii) The third objective is to improve the overall classification accuracy of Hybrid-pol data using various machine learning algorithms.
(iv) The fourth objective of this study is to explore the potential of compact polarimetry and compare it with other compact polarimetry modes.
(v) The fifth objective is to record, compare, and analyze the response of circular transmission over linear transmission and its interaction with the targets.
(vi) The sixth objective is to compare the penetration capability and information content of L-band Alos Palsar-2 and C-band RISAT-1 data.

1.9 Thesis Organization

The thesis is organized into seven chapters. The first chapter presents the introduction, background, motivation for the research work, problem statement, and literature survey. The second, third, and fourth chapters and fifth provide the contributions of the research work. The sixth chapter provides the conclusions of the research work. The summary of each chapter is given below.

- Chapter 1: The First chapter deals with the introduction to Microwave Remote Sensing, and Radar Polarimetry. The motivation for the research is explained and the corresponding problem statement is derived. A literature survey is carried out for the problem statement identified.

- Chapter 2: The Second Chapter deals with the importance of speckle filtering and the effect of speckle window size on speckle reduction. Polarimetric Speckle filters preserve the information without a smoothing effect. Dual-pol, Hybrid-pol, Quad-pol, and Psuedo Quad pol data were used for speckle filtering for various land targets [25-38].
- Chapter 3: The Third Chapter deals with the Target Decomposition theorems which characterizes the targets. In this chapter, a Four-component decomposition along with the robust m-delta and m-chi decomposition are explained in detail [39-56].
- Chapter 4: The Fourth Chapter deals with improving the classification accuracy on Hybrid-pol data using Supervised clasifier. In this chapter, an SVM parameterization effect on classification accuracy will be discussed in detail. A comparison of SVM classifier with Wishart classifier and other machine learning algorithms will be analyzed [57-70].
- Chapter 5: The Fifth Chapter deals with Exploring the Capability of Compact Polarimetry over other modes [71-92].
- Chapter 6: The sixth chapter deals with a comparison of Hybrid-Pol, C band RISAT-1 data over dual-pol and quad-pol for Land Cover Classification and Crop Identification [92-95].
- Chapter 7: A summary of the contributions and the conclusions drawn from the earlier chapters were discussed. The future extension of the proposed work is also discussed.

1.10 Imaging modes

SAR Images in three different modes depending on the application and the user requirement as shown in Fig 1.11 and Table 1.3.

Stripmap SAR: In this mode, the antenna pointing direction is constant as the radar platform moves. The beam sweeps along the ground at an approximately uniform rate, and a contiguous image is formed. A strip ground is imaged, and the length of the strip is only limited by how far the sensor moves or how long the radar is left on. The azimuth resolution is governed by the antenna length.

Scansar: This mode is a variation of stripmap SAR, whereby the antenna is scanned in range several times during a synthetic aperture. In this way, a much wide swath is obtained, but the azimuth resolution is degraded (or the number of looks is reduced). The best azimuth resolution can be obtained in that of the stripmap mode multiplied by the number of swaths scanned.

Spotlight: The resolution of the stripmap mode can be improved by increasing the angular extent of the illumination on the area of interest (a spot on the ground). This can be done by steering the beam gradually backwards as the sensor passes the scene. The beam steering has the transient effect of simulating a wider antenna beam (i.e., a shorter antenna). However, the antenna must ultimately be steered forward again, and a part of the ground is missed. This means that the coverage is not contiguous; only one spot on the ground is imaged at a time.

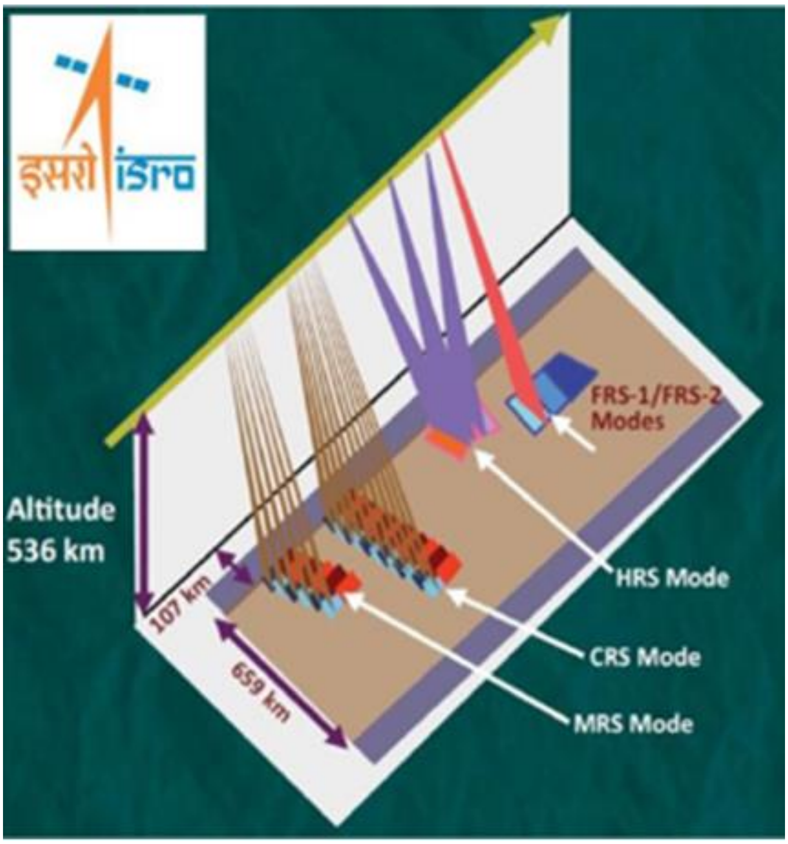

Fig 1.11 RISAT-1 Imaging Modes © ISRO

Mode	HRS	FRS-1	FRS-2	MRS	CRS
swath	10m	25km	25km	115km	223
Pol	Single, Dual, Circular	Single, Dual, Circular	Quad circular	Single, Dual, Circular	Single, Dual, Circular
Resolution	1*1(m)	3*2(m)	9*4 (m)	21-23*8 (m)	41-55*8 (m)
	spotlight mode	stripmap	stripmap	scansar	scansar

Table 1.3 Acquisition Modes of RISAT-1

The datasets and study area used in this work is shown in Table 1.4.

1.11 Datasets and Study Area

Dataset	Band	Date of Acquisition	Acquisition mode	Resolution
RISAT-1 (Ghanpur Vil, Warangal Dst, Telangana, India. Compact pol Dual-pol	C C	5-07-2016 5-12-2015	FRS-1 FRS-1	3 meters
RISAT-1 (Hyderabad),India Hybrid Quad	C	29-09-2016 26-09-2014	FRS-1 FRS-1 FRS-2	3 meters
Alos Palsar -1 (Hyderabad) Alos Palsar-2 (Sanfransico, Mt Fuji, Tokyo)	L	23-08-2010	Dual-pol Quad-pol	Better than 1meter
Sentinel 1A, 1B (Chennai), India	C	18-12-16	Dual-pol	

Table 1.4 Datasets and Study Area

1.12 Land Use and Land Cover (LULC)

Land cover: physical and biological cover of earth surface including artificial surfaces, agriculture areas, forests, wetlands, water bodies.

Land use: territory characterized according to its current and feature planned dimensions or socio-economic purpose (residential, commercial industrial, agriculture, forestry).

1.13 Scientific tool used for processing

- Envi SARscape [103]
- PolSARpro [104]
- SNAP [105]

Chapter 2

Importance of Speckle Filtering in Image Classification of SAR Data

Contributions and citations of this chapter

Publication: 4

Citations: 9

2.1 Introduction

In this chapter, the research was performed on dual-pol, Hybrid-pol, and quad-pol SAR datasets. Furthermore, the selection of polarization channels and the selection of amplitude and intensity images in SAR images are discussed in this chapter. This study specifies data selection in terms of the filter size, polarization, and amplitude or intensity for a SAR image. This chapter deals with the importance of speckle filtering in SAR images for classification. This chapter describes the effect of speckle window sizing with respect to speckle reduction. In this chapter, speckle filter analysis was performed on urban targets, i.e., Tokyo City, Japan, Quebec City, Vegetation target, i.e., Amazon forest, Heterogeneous target, i.e., Mt Fuji, Japan. We presented a comparative study between several speckle filters that are widely used in the radar imaging community. Speckle evaluation is done by Speckle Suppression Index (SSI) ENL, SMPI. Based on the SSI values for a filter, image classification was performed using K Mean cluster analysis.

2.2 Speckle

Speckle is a grainy salt and pepper pattern in the image due to the interference of the backscattered signal from the target. SAR images suffer from Speckle, and it is a general phenomenon in all imaging systems [25]. Therefore, the presence of speckles in the data reduces its capability for advanced analysis, e.g. image segmentation, image classification, image fusion with optical data etc., and makes it difficult for the analyst to interpret [26]. The Speckle can be reduced by processing separate portions of an aperture and recombining them so that the interference does not occur. This process is called Multilooking.

2.2.1 Speckle Filtering

The reduction of Speckle is made using Speckle Suppression Techniques in two approaches. The first technique involves an average process, generally known as Multilook. The Multilook reduces speckle-noise at the cost of spatial resolution. There is a trade-off between the reduction of speckle noise and the loss of the SAR image's spatial properties. The second technique involves smoothing the image using digital image processing techniques, and it can be performed after the image is obtained [27]. When a filter is selected for speckle reduction, it should smooth homogenous area while preserving linear features, edges, point targets. A filter should remove speckles without sacrificing image structure such as edges, linear features. The most commonly used filters are:

Mean Filter

This filter calculates the mean value of the pixels of the neighbor window. The mean value will replace the center pixel value window. This filter cannot preserve information and resolution.

Median Filter

This filter calculates the median value of the pixels of the neighbor window. The median value will replace the center pixel value window. The common problems of this filter, its cause's edge blurring, and the thin linear features will disappear, and object shape distortion takes place.

Frost filter

This filter calculates exponentially weighted averaging based on the coefficient of variation, which is the local standard deviation ratio to the local mean.

This filter preserves sharp features by retaining its original pixel value while at low coefficient variation.

Lee Filter

The Lee filters compute a linear combination of the center pixel intensity in a filter window with an average intensity of the window. This filter is based on the minimum mean square error (MMSE)

2.2.2 Polarimetric Filters

Refined Lee Filter

The Minimum Mean Square Error (MMSE) filter cannot remove the Speckle near the edges effectively. To overcome this problem, the refined lee filter uses a no square window to match the edges' direction. Pixels that are in the non-edge area are used for computation. Refined lee filter follows three processing steps, 1) selection of edge aligned window, 2) Computation of filtering weight (b) from the span image, 3) Filtering each element in the covariance matrix [Y] with the weight (b). The filtered matrix is given by

$$Y^\wedge = \bar{Y} + b\left(Y - \bar{Y}\right) \tag{1.1}$$

Where $\bar{Y}$ is the local mean of matrices computed with pixels in the same edge directed window. We have opted for a 3x3 window size kernel for speckle filtering.

Boxcar filter:

It is a spatial averaging filter; it averages the pixels in the neighborhood of the pixel mask. It replaces the value of every pixel with the average of neighborhood pixels. It improves the radiometric resolution at the expense of spatial resolution.

Intensity-driven adaptive-neighborhood (IDAN):

Instead of employing edged aligned windows, a set of stationary pixels surrounding the pixel under analysis, adapting to the data's local morphology. The filtering process considers only the information provided by the diagonal elements of the covariance or coherency matrices to determine stationary pixels. The stationary neighborhood's search process is started by a seed pixel derived from the 3×3 median values of the diagonal elements. The covariance or coherency matrix's estimated value is obtained through the mean value of the pixels within the adaptive neighborhood.

2.2.3 Study Area and SAR Dataset

The study area used in this paper is of Mt Fuji, Japan**.** The Geo-coordinates of the study area are 35 °.27'30"N and 138 °.44'6"E, and also Amazon forest in the state of Roraima, South America. The Geo-coordinates of the study area are 0 °.53'44"N center latitude and 59 °.19'25"W, center longitude.

SAR Dataset: The SAR dataset used in this work is ALOSPALSAR-2 of Level 1.5 CEOS (Committee on Earth Observing Sensors) format and was provided by JAXA, Japan.

ALOS-PALSAR-2

Advanced Land Observation Satellite Phased Array type L-band Synthetic Aperture Radar was launched on 24 May 2014 by JAXA. Alos was the first L band spaceborne SAR mission, launched by ALOS-2 satellite with PALSAR-2 sensor. The satellite has SAR with dual-polarization modes (HH-HV).

Fig 2.1 is the flow chart of the proposed work in this chapter.

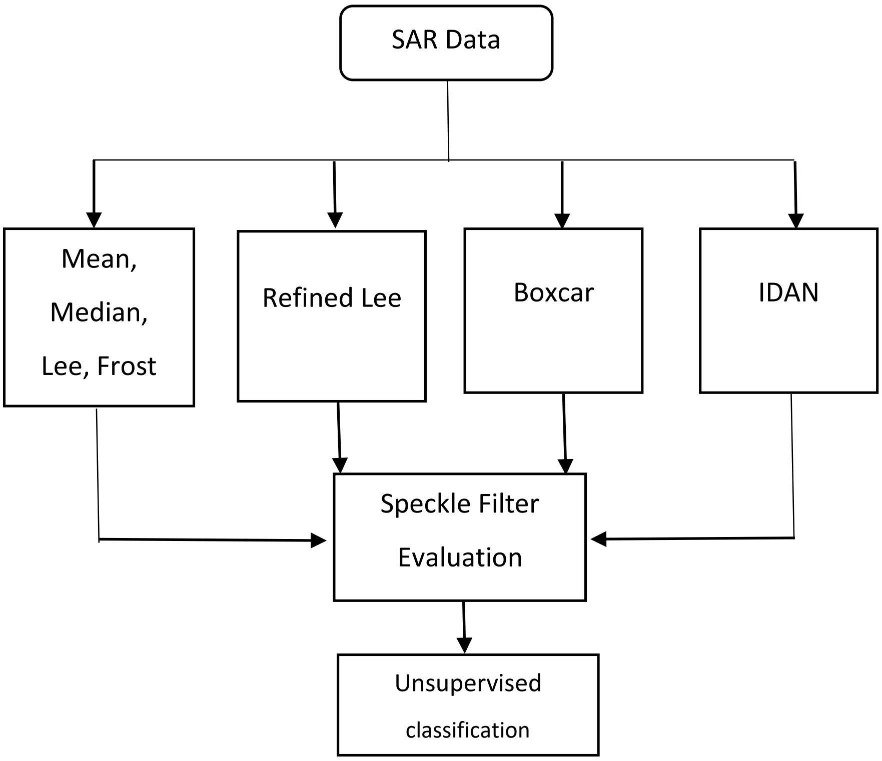

Fig 2.1 Flowchart of the proposed work

2.3. Importance and Impact of Speckle Filter Window Size in Speckle Reduction

2.3.1 Methodology

The process of removal of Speckle in a SAR image is essential for the analyst to interpret. A filter should remove speckle noise without sacrificing image structure such as edges, linear features. The performance can be verified with the commonly available commercial image processing software such as PolSARpro [104], ENVI [103], and NEST [105]. Fig 2.1 shows the pre-processing procedure of the proposed work.

NEST (Next ESA SAR Toolbox) 5.0 β is developed by Array systems computing Inc. of Toronto, Canada, under ESA (European Space Agency). It is an open-source toolbox for reading, post-processing, analyzing, and visualizing an extensive archive of data of level 1 from ESA and also includes SAR missions like ERS-1, 2, ENVISAT, Sentinel-1. NEST 5.0 β has six speckle filters, Mean, Median, Frost, Lee, Refined Lee, and Gamma-Map. Multilooking, radiometric correction, and conversion of slant range to the ground range can also be performed. In this work, the speckle filters of NEST 5.0 β have been used on SAR datasets of ALOSPALSAR-2.

Fig. 2.2 shows the step by step procedure for the proposed work. Level 1.5 format is preferred because it is already slanted range to ground range converted data. As the level 1.5 format data consists of Speckle, it isn't easy to interpret the data and classify it. Using the speckle filters in NEST, data has to be filtered. The ALOS PALSAR-2 operates with dual-polarization, i.e., HH, HV polarizations. For example, HV means transmit in horizontal (H) polarization and receive in vertical (V) polarization. Each polarized data consists of amplitude and intensity images. Selection of images can be done using indices and visually.

We opted 3x3, 5x5, 7x7, 9x9, 11x11 filter window size for speckle filtering in this study. As the window size of the speckle filter increases, Speckle in the image reduces, as window size increases, we may lose the image's details [27]. Filter evaluation is done using three indices, ENL (Equivalent Number of Looks), SSI (Speckle suppression index) [28], and SMPI (Speckle Suppression and Mean Preservation Index) [29]. Finally, the best filter is selected based on these indices values. Speckle Filter Assessment Indices.

2.3.2 Filter Evaluation

Speckle Filter Assessment Indices

Generally, evaluation of speckle reduction in SAR images is done using indices and visually. These indices help us to evaluate different speckle filters using their values.

1) Speckle suppression index (SSI):

SSI is defined as

$$SSI = \frac{\sqrt{\operatorname{var}iance\left(I_f\right)}}{mean\left(I_f\right)} * \frac{mean\left(I_o\right)}{\sqrt{\operatorname{var}iance\left(I_o\right)}} \tag{1.2}$$

Where I_f = Filtered image, I_o = Noisy image.

The SSI value should always be less than one and hence can be considered that filter is efficient in reducing the speckle noise. Lower values indicate better performance of the speckle filter.

2) Equivalent Number of Looks (ENL):

$$ENL = \left(\frac{mean}{standard\ deviation} \right)^2 \tag{1.3}$$

For a speckle-free image, the value must be high.

3) Speckle Suppression and Mean Preservation Index (SMPI):

$$SMPI = Q * \frac{\sqrt{\operatorname{var}iance\left(I_f\right)}}{\sqrt{\operatorname{var}iance\left(I_o\right)}} \tag{1.4}$$

$Q = 1 + \left| mean(\mathrm{I}_0) - mean(\mathrm{I}_f) \right|$, Where I_f = Filtered image, I_o = Noisy image

Lower values of SMPI indicates better performance in terms of speckle reduction and mean preservation.

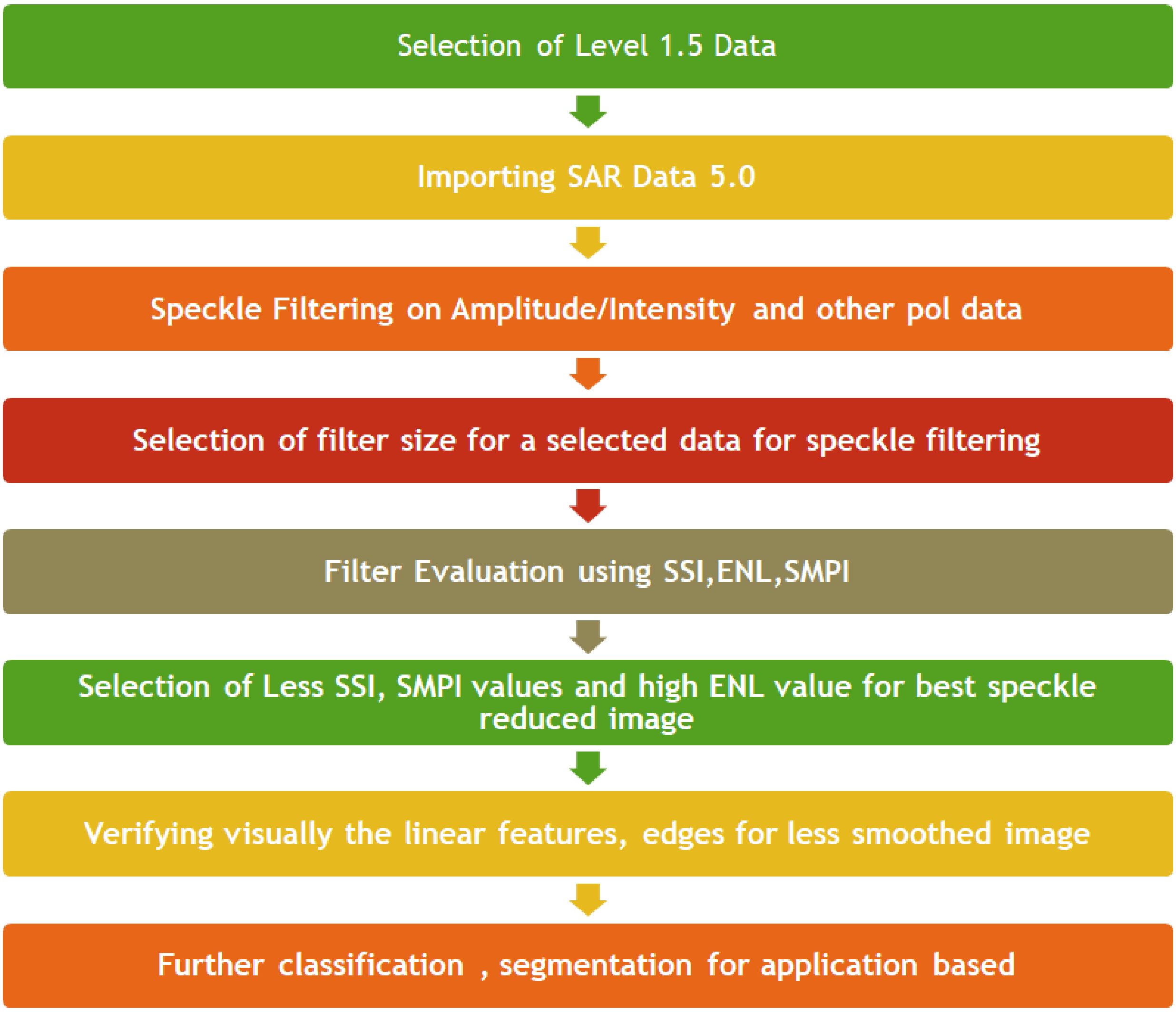

Fig. 2.2 preprocessing procedure.

2.4. Results and Discussions:

Fig 2.3 shows ALOS PALSAR-2 dual-pol data with amplitude and intensity (HH and HV) for level 1.5 of Mt Fuji, Japan, with a median filter (3x3). For better visual clarity, median filtered images are shown instead of original images (level 1), containing Speckle.

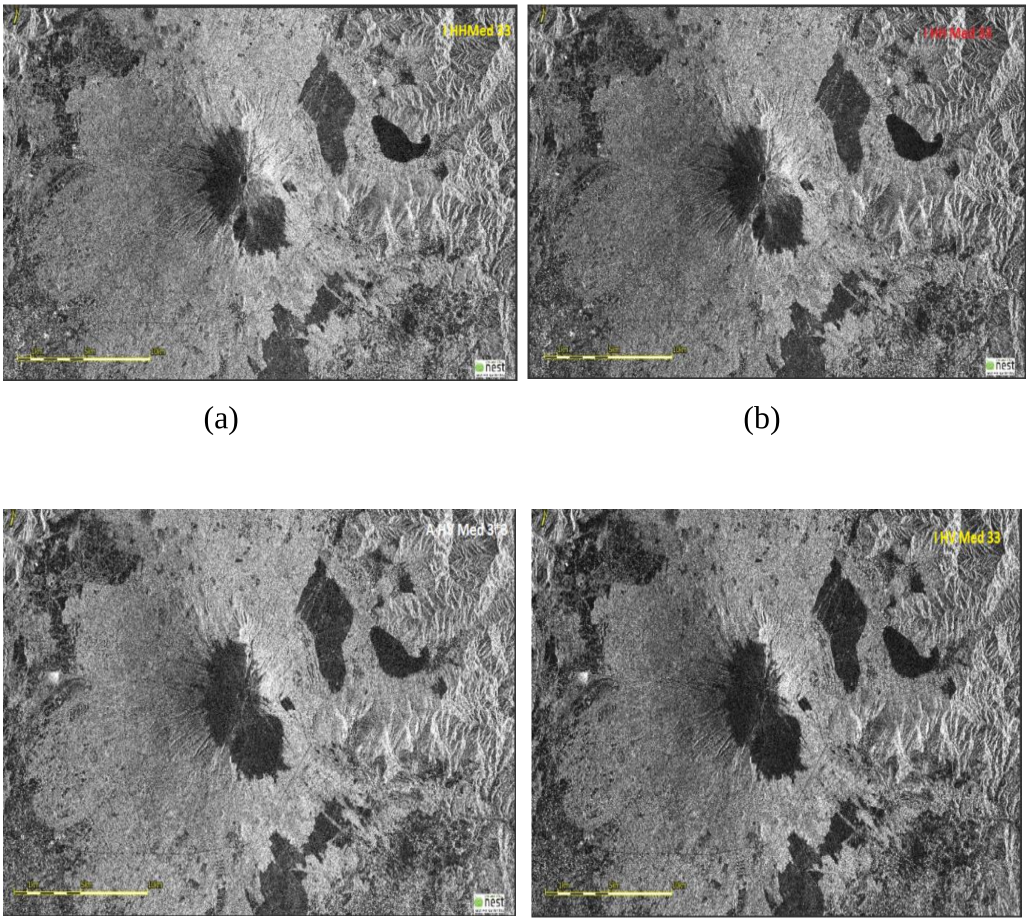

(a) (b)

(c) (d)

Fig. 2.3 Illustration of amplitude and intensity images in Alos Palsar-2

The images in Fig 2.4 show the impact of speckle filter size on speckle reduction. Fig 2.4(a) is the study area shown in Google Maps, Figure 2.4(b) is the original image with Speckle. Table 2.1 shows the values of SSI, ENL, SMPI for Amplitude (AHH, AHV), and Intensity (IHH, IHV) images for various speckle filters. As the filter window size increases, SSI values decreases, ENL values increases, and SMPI value decreases.

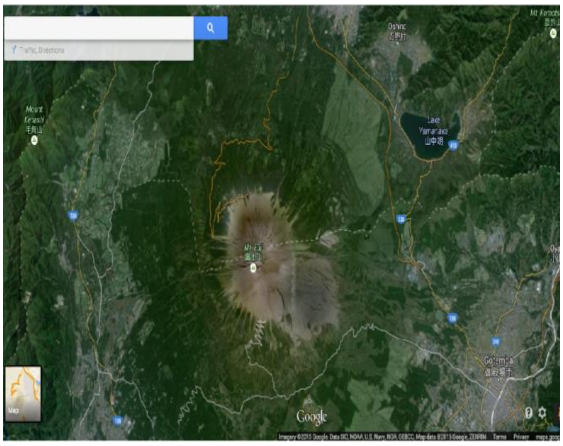
Oshino
Lake Yamanaka
山中湖
Mount Fuji
富士山
Gotemba
御殿場市
Google

(a)

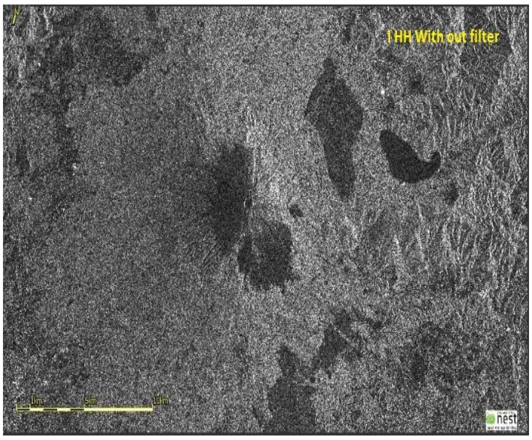
I HH With out filter
nest

(b)

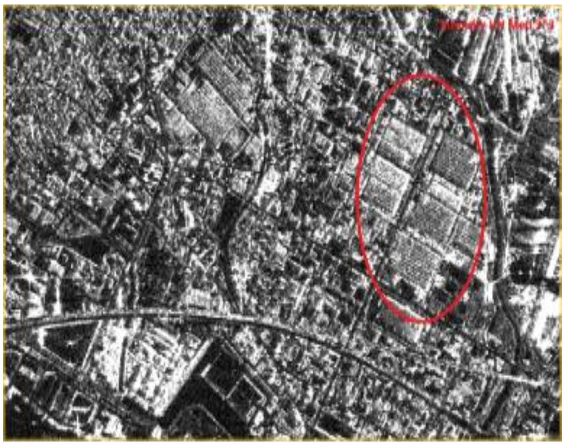
Intensity HH Med 3*3

(c)


Intensity HH Med 5*5

(d)


Intensity HH Med 7*7

(e)


Intensity HH Med 99

(f)

(a): Google Maps

(b): Original Image

(c): Med 3x3, (d) Med 5x5, (e): Med 7x7,

(f): Med 9x9, (g):11x11

(g)

Fig. 2.4. Effect of filter window size and edge smoothing during speckle filtering on I HH image.

Fig 2.4(c) – 2.4 (g) of the median filter indicates the reduction in Speckle. However, as the filter size increases, smoothing of the image occurs, and the linear features like edges disappear. Selection of best speckle filter with good preservation can be done using indices value. When an image is classified with Speckle, the classification will not be accurate, and it will be difficult for the analyst to understand an image. We can easily find out the impact of filter window size in classification [30-32]. From Table 2.1, I HH image shows less SSI value for the 7x7 median filter, followed by a mean filter and Lee filter. Filter window size 7x7 shows good results than 5x5 and 3x3; similarly, ENL value increases with an increase in filter window size. The ENL values of amplitude images are more than an intensity image.

Similarly, I HV median filter with a 7x7 filter size shows a high ENL value. Even though 11x11 size shows a value higher than 7x7, 7x7 is selected because it has a less smoothing effect. SMPI value in both images decreases with an increase in filter size. I HH median 7x7 shows less SMPI value, indicating better performance in terms of speckle reduction and mean preservation [33].

Fig 2.5 shows the graphical representation of the values given in Table 2.1. It is a graphical representation of ENL, SSI, and SMPI values for amplitude and intensity images for various filters with various filter window sizes. Frost filter has high SSI values due to the damping factor (2, 4); the SSI values are very high, different from other filters. So, for a Frost filter, a less damping factor is preferred. The Gamma filter with filter size 11x11 is not preferred because its SSI value is more. The median filter shows less SMPI value indicating mean preservation.

		Amplitude HH					Intensity HH					Amplitude HV					Intensity HV				
		Mean	Std	Ssi	SMPI	ENL	Mean	std	Ssi	SMPI	ENL	Mean	Std	SSI	SMPI	ENL	Mean	Std	SSI	SMPI	ENL
without filter		1264.239	424.015				850627.5	1491674				974.5534	305.2594				720301	713887.1			
Mean	3x3	1277.966	264.5318	0.617172	8.563914	23.33902	1434215	1008771	0.401092	0.256414	2.02136	981.0814	178.6604	0.58138	3.825864	30.15459	894440	429254.2	0.484226	104708.4	4.341835
	5x5	1284.175	234.3926	0.544212	11.02037	30.01652	1651378	860223.3	0.29705	0.218655	3.685282	984.0589	157.4331	0.510754	4.906903	39.0706	960562.1	370712.1	0.3894	124764.5	6.713938
	7x7	1285.228	220.0674	0.510533	10.89707	34.10742	1733499	793701.1	0.261095	0.201746	4.770162	986.7103	148.1998	0.479507	5.906343	44.32861	1004117	343837.3	0.345504	136697.7	8.52831
	9X9	1285.06	210.7822	0.489056	10.35401	37.16886	1740767	750104.2	0.245723	0.190665	5.385653	988.2468	142.5407	0.460479	6.398274	48.06767	1028782	326340.6	0.320061	141016.7	9.938126
	11X11	1286.615	203.8148	0.472319	10.7588	39.84974	1756741	717062.9	0.232764	0.182266	6.002069	989.3329	138.4356	0.446727	6.706556	51.07276	1043197	314309.7	0.304002	142164.5	11.01583
Median	3x3	1282.783	273.5801	0.635886	11.96503	21.98556	1370427	945201.3	0.393309	0.171638	2.102147	986.5348	187.9933	0.608368	7.382378	27.53849	838140.9	426975.1	0.514008	70480.05	3.853265
	5x5	1286.86	234.4138	0.543125	12.50609	30.13675	1597355	762874.8	0.272344	0.138529	4.384258	991.3305	160.5914	0.517178	8.829257	38.10591	966528.7	342486.1	0.35753	118127.4	7.964226
	7x7	1284.946	217.2604	0.504131	10.61239	34.97911	1600837	696153.5	0.247984	0.126413	5.287914	991.9229	149.4209	0.480917	8.50508	44.06899	984310.4	313351.5	0.321206	115883.6	9.867351
	9X9	1282.894	206.9259	0.480919	9.105984	38.4372	1592339	655348.1	0.234694	0.119004	5.903737	991.8152	142.7733	0.459571	8.076324	48.2578	990789.6	297548.4	0.303013	112739.8	11.08786
	11X11	1281.537	199.611	0.46441	8.145116	41.21858	1587710	623123.1	0.223804	0.113152	6.49224	990.898	138.468	0.446126	7.416735	51.21051	988144.6	286788.8	0.292837	107600.5	11.8718
Frost2	3x3	1277.232	264.9786	0.61857	8.122188	23.23366	1270469	1055929	0.473954	0.454704	1.447635	980.7654	178.9272	0.582435	3.643054	30.04537	870488.9	437652.9	0.507284	92073.75	3.956096
	5x5	1280.246	235.7297	0.548996	8.899149	29.49567	808372	1201138	0.84732	0.517235	0.452935	983.1872	158.0486	0.513205	4.471847	38.69823	839697.4	403417.9	0.484749	67471.07	4.332468
	7x7	1278.858	222.3979	0.518509	7.669746	33.0661	731784.6	1219668	0.950438	0.525214	0.359984	983.5295	149.2307	0.484404	4.389691	43.43686	761147.9	420585	0.557531	24065.01	3.275145
	9X9	1275.699	214.273	0.500803	5.793621	35.44556	726368.2	1227726	0.963851	0.528684	0.350034	982.6208	144.0044	0.467871	3.807282	46.56079	713395.8	431636.2	0.610481	4175.193	2.731652
	11X11	1275.02	208.4711	0.487502	5.302762	37.40609	724072.9	1232368	0.970562	0.530683	0.34521	982.0099	140.3235	0.456196	3.429142	48.9746	702974	430899.1	0.618473	10458.65	2.661506
Frost4	3x3	1275.155	265.9824	0.621925	6.850203	22.98371	949508.1	1222028	0.733919	0.206474	0.603719	980.3377	179.5452	0.584702	3.404447	29.81287	832703.2	462580	0.560507	72833.76	3.24046
	5x5	1272.724	238.1032	0.5578	4.76504	28.57184	737450.6	1272274	0.983814	0.214963	0.335973	980.4831	159.1444	0.518189	3.09342	37.95749	735170.5	469960.7	0.644998	9788.892	2.447107
	7x7	1269.006	226.3219	0.531754	2.548235	31.4394	735335.5	1281026	0.993431	0.216442	0.3295	979.1982	150.9122	0.492029	2.298183	42.10101	710082.1	471336.8	0.669742	6747.065	2.269627
	9X9	1266.694	219.6054	0.516915	1.274925	33.27033	735121.8	1286497	0.997964	0.217366	0.326513	977.7248	146.2307	0.477484	1.521075	44.705	707044.7	469169.4	0.669526	8712.218	2.27109
	11X11	1266.396	215.0934	0.506414	1.097764	34.66449	735651.9	1291153	1.000854	0.218153	0.32463	977.1018	143.0487	0.467391	1.19603	46.65646	795950.3	468596.8	0.594016	49656.48	2.885182
Gamma Map																					
	3x3	1277.536	264.5308	0.617378	8.299878	23.32349	1432705	990428.8	0.394214	1.304733	2.092508	980.7082	178.6691	0.581629	3.606643	30.12872	874714.3	445196.7	0.513535	96296.35	3.860368
	5x5	1284.045	234.3784	0.544234	10.94796	30.01409	1527439	893304	0.333504	1.176786	2.923677	983.6938	157.4204	0.510902	4.717371	39.04791	939514.7	388283.6	0.416994	119231	5.854759
	7x7	1284.823	220.0486	0.51065	10.6858	34.09174	1454790	861780.8	0.337802	1.135259	2.849751	986.3316	148.1797	0.479626	5.720906	44.3066	941100.2	375077	0.402132	116008.6	6.295509
	9X9	1285.163	210.7634	0.488973	10.40415	37.18143	1453865	853817.8	0.334893	1.124769	2.899463	987.3415	142.5327	0.460876	5.974434	47.98503	936766	365220	0.393376	110742.6	6.578898
	11X11	1286.16	203.7949	0.472439	10.53949	39.82939	706352.7	1148642	0.927317	1.513153	0.378159	985.4858	138.4769	0.448604	4.962615	50.64611	898852.8	375839.5	0.421889	94002.47	5.719687
Lee																					
	3x3	1277.787	264.5305	0.617256	8.456766	23.33273	1445958	1000973	0.394759	0.627966	2.086732	980.9529	178.6645	0.581469	3.750476	30.14531	888964.3	440218	0.499652	104006.2	4.077867
	5x5	1284.173	234.3938	0.544215	11.01966	30.01615	1647344	881709.5	0.305215	0.553145	3.490741	984.0575	157.4342	0.510758	4.905981	39.06994	960348.3	383178.9	0.402585	128845.4	6.281371
	7x7	1285.226	220.0692	0.510538	10.89604	34.10674	1594279	844649.3	0.302119	0.529895	3.562672	986.7086	148.2053	0.479525	5.905516	44.32516	968754.8	363732.3	0.378837	126589.6	7.093557
	9X9	1285.602	210.7888	0.488865	10.62342	37.19784	1400541	846347.5	0.344602	0.530961	2.738384	988.2455	142.5512	0.460514	6.397926	48.06046	954352.5	353440.1	0.373673	115877.2	7.29098
	11X11	1286.613	203.8264	0.472346	10.75876	39.84511	1269887	868912.4	0.39019	0.545117	2.135886	988.762	138.4545	0.447046	6.448326	50.99991	894462.1	363267.7	0.409779	88623.47	6.062758

Table 2.1: SSI, ENL, SMPI values for various filters with different window size

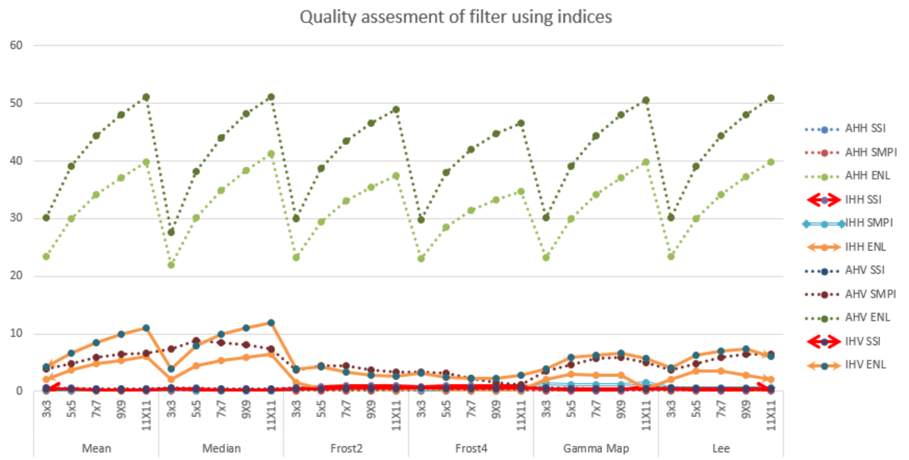

Fig 2.5 Graphical representation of ENL, SSI and SMPI values for various filters

Fig 2.6 (a - f) shows the comparison of various filters of size 7x7 filter size. Images of Figure 2.6 (c-d) are of frost filter with 2 and 4 as damping factors. Using indices, the best filter is preferred for further classification. Table 2.1 shows that the median filter I HH has less SSI value, less SMPI value, and a high ENL value. So median filter 7x7 is used to perform K- mean classification. The classified image is shown in Fig 2.6. Fallow land, vegetation, wetland /water, and buildings are represented in a different color, as shown in the legend.

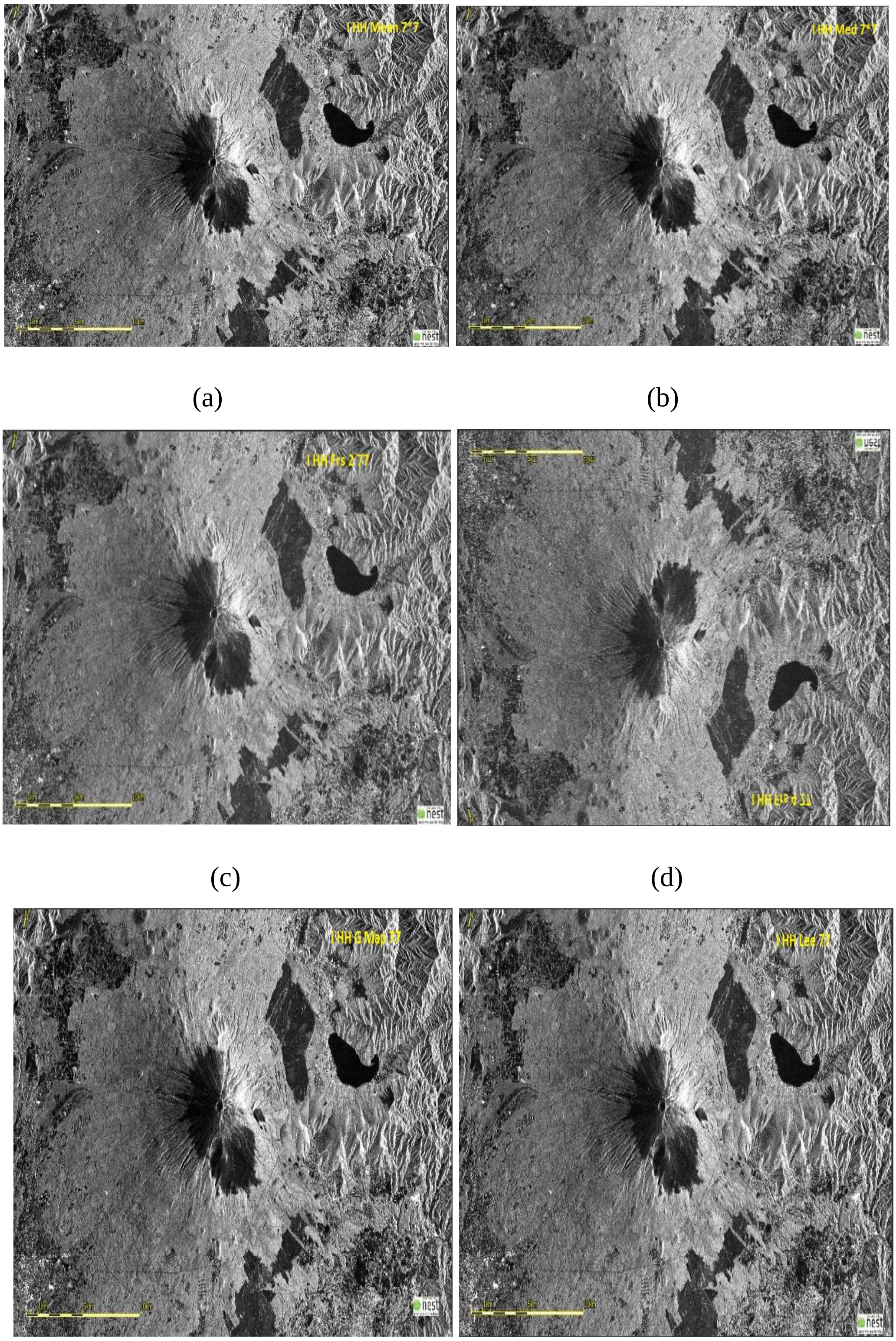

(a) (b)

(c) (d)

(e) (f)

(a): Mean filter, (b): Median Filter, (c): Frost Filter (Df=2), (d): Frost Filter (Df=4), (e): Gamma Map Filter, (f): Lee Filter

Fig. 2.6. Illustration of Intensity images of 7x7 filter window size of various filters.

2.5 Importance of speckle filtering in SAR image classification

2.5.1 Unsupervised classification

In this approach, the identities of land cover types specified as classes within a scene are generally not known prior. When the ground information/surface features are lacking, the unsupervised approach has opted. The computer groups pixels with similar spectral characteristics into unique clusters with statistically determined criteria. Later, the analyst then combines and re-labels the spectral clusters into information classes.

2.5.2 K-Mean Clustering

K-means classification is an unsupervised classifier, where training sites is not required. Clustering algorithm is a cluster analysis method that aims to partition n observations into k clusters in which each observation belongs to the cluster with the nearest mean. The K-means clustering algorithm is also known as C-means clustering and has been applied to various areas, including image and speech data compression. The objective function is defined as

$$W=\sum_{j=1}^{M}\sum_{i=1}^{N}\left|(E_i^{(j)}-V_j)^2\right| \qquad (1.5)$$

Where $(E_i^{(j)}-V_j)^2$ is a distance measured between a data point $E_i^{(j)}$ and the cluster V_j is an indicator of the n data points' distance from their respective cluster centers.

The below Figure 2.7 (a - e) shows the subset of Amazon Forest, Fig 2.7 (a) is an optical image acquired from Google Maps, 2.7 (b) is a Microwave image with Speckle, 2.7 (c) is the Mean filter 3*3 window size image, 2.7 (d) is the Mean Filter 5*5 window size image, 2.7 (e) is the Mean Filter 7*7 window size image. We opted for Intensity HH pol data because of its less SSI value compared to Intensity HV pol data. We observe that as window size increases, speckle value decreased from 3*3 window size to 7*7 window size (0.686337 to 0.535655) as shown in Fig [2.9, 2.10]. Similarly, we opted for 7*7 window size and Mean filter, based on SSI values. For classification, less Speckle free data is preferred, so a mean filter image is selected for K mean classification [34].

(a) Optical image

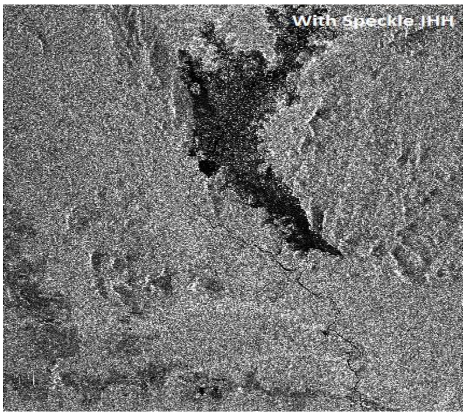

(b) Microwave image with speckle

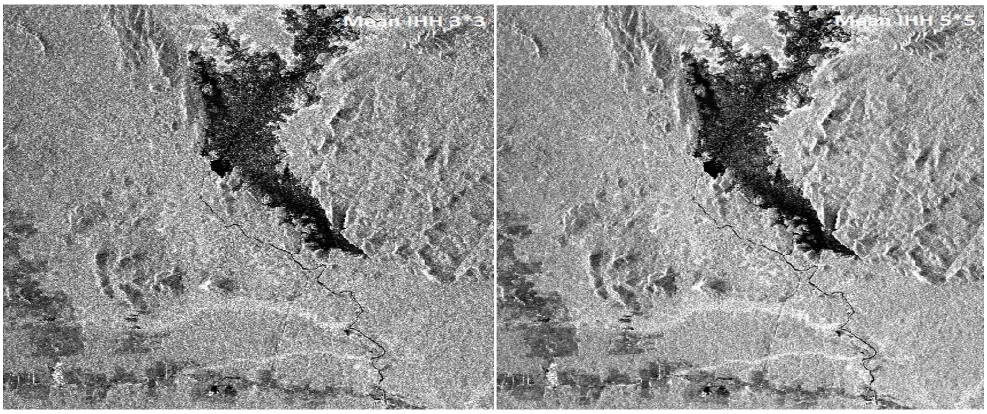

(c) Mean Filter I HH 3*3 (d) Mean Filter I HH 5*5

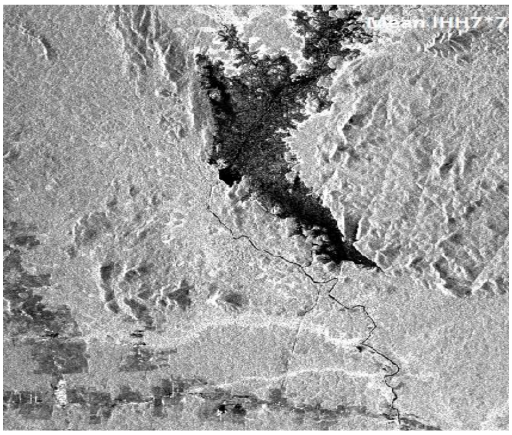

(e) Mean Filter I HH 3*3

Fig. 2.7 Speckle Filtering with different window sizes for Mean filter Intensity HH pol data.

The below Figure 2.8 (a) is the classified image without speckle filtering, due to the presence of speckle analyst cannot classify the image. Figure 2.8 (b, c, d) represents k mean classified images for the Mean filter for 3*3, 5*5, 7*7 window size. We can observe the difference in 3*3, 5*5, and 7*7 window sizes, i.e., red ellipse part is not classified correctly because of speckle presence. As window size increases, classification can be done more accurately due to reducing the Speckle in it. Mean filter 7*7 classified image gave the right information in classifying the image such as light green indicates deforested part, light blue indicates water, red shows forest, respectively. Hence window size plays a vital role in the classification of an image. As the window size increases, smoothing of the image can happen; even edges and linear features may disappear [35]. So the selection of window size plays a crucial role in classification. The classified image results are verified with Google maps.

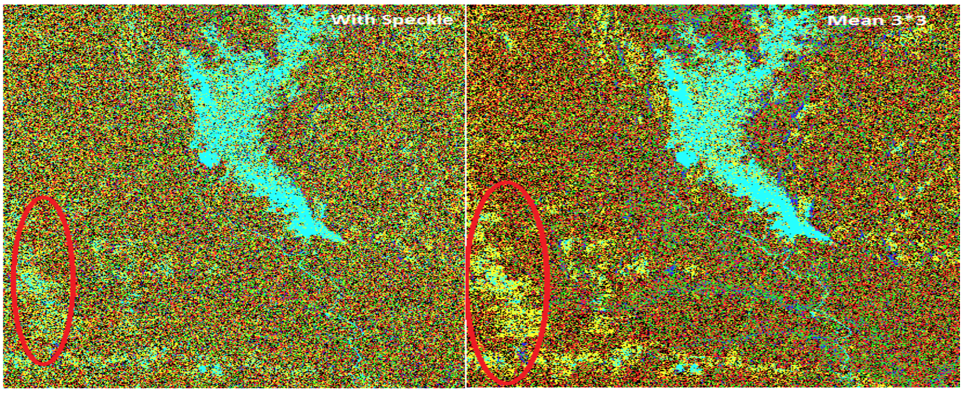

(a) Microwave image with Speckle (b) K Mean Classified I HH 3*3

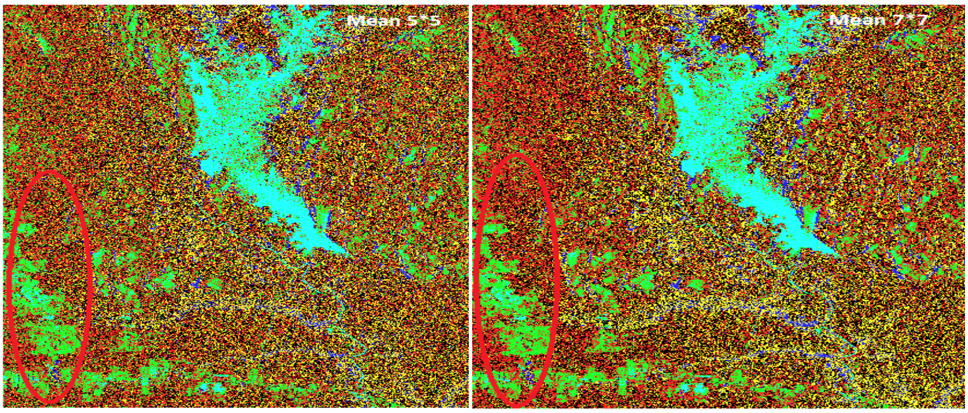

(c) K Mean Classified I HH 5*5 (d) K Mean Classified I HH 7*7

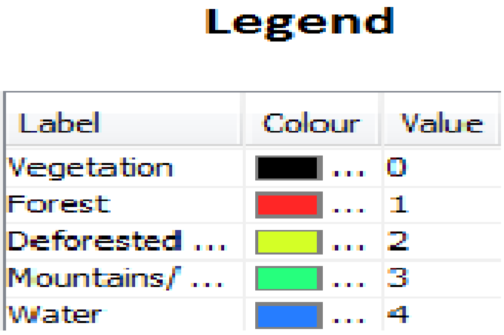

Legend

Label	Colour	Value
Vegetation	⬛ ...	0
Forest	🟥 ...	1
Deforested ...	🟨 ...	2
Mountains/ ...	🟩 ...	3
Water	🟦 ...	4

Fig. 2.8 K Mean Classified image.

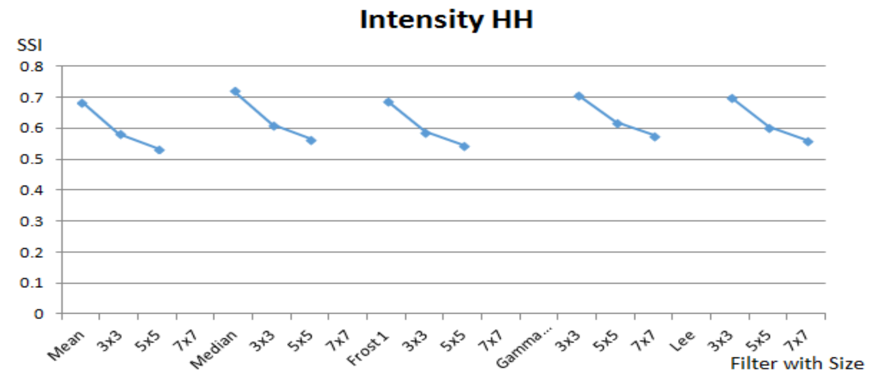

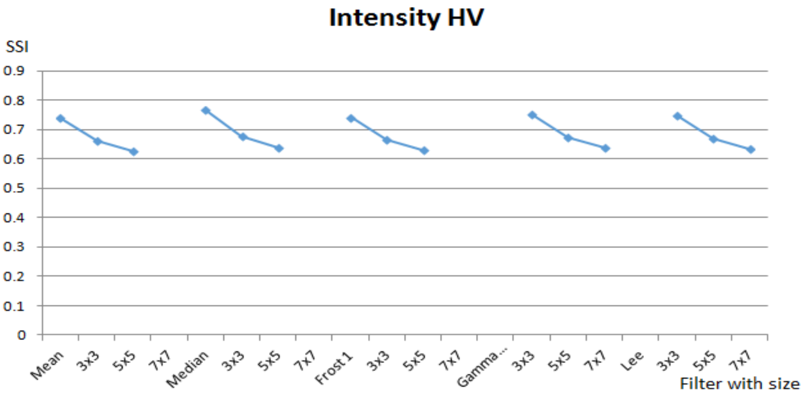

Fig. 2.9. Graphs for various filter with different window size with SSI values.

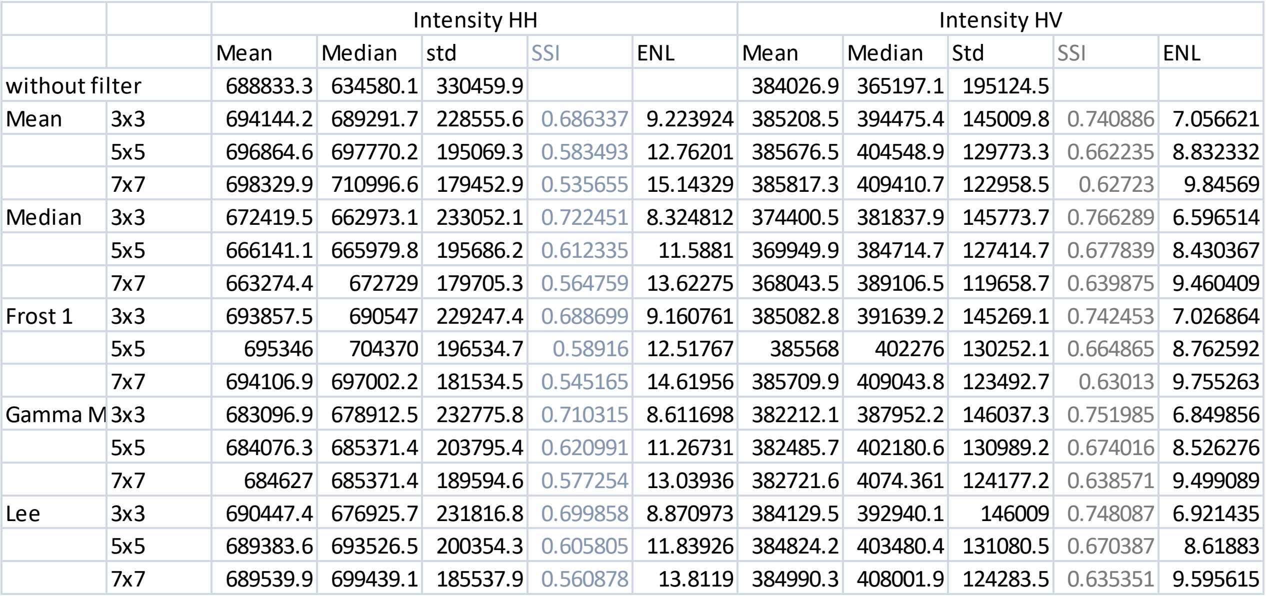

		Intensity HH					Intensity HV				
		Mean	Median	std	SSI	ENL	Mean	Median	Std	SSI	ENL
without filter		688833.3	634580.1	330459.9			384026.9	365197.1	195124.5		
Mean	3x3	694144.2	689291.7	228555.6	0.686337	9.223924	385208.5	394475.4	145009.8	0.740886	7.056621
	5x5	696864.6	697770.2	195069.3	0.583493	12.76201	385676.5	404548.9	129773.3	0.662235	8.832332
	7x7	698329.9	710996.6	179452.9	0.535655	15.14329	385817.3	409410.7	122958.5	0.62723	9.84569
Median	3x3	672419.5	662973.1	233052.1	0.722451	8.324812	374400.5	381837.9	145773.7	0.766289	6.596514
	5x5	666141.1	665979.8	195686.2	0.612335	11.5881	369949.9	384714.7	127414.7	0.677839	8.430367
	7x7	663274.4	672729	179705.3	0.564759	13.62275	368043.5	389106.5	119658.7	0.639875	9.460409
Frost 1	3x3	693857.5	690547	229247.4	0.688699	9.160761	385082.8	391639.2	145269.1	0.742453	7.026864
	5x5	695346	704370	196534.7	0.58916	12.51767	385568	402276	130252.1	0.664865	8.762592
	7x7	694106.9	697002.2	181534.5	0.545165	14.61956	385709.9	409043.8	123492.7	0.63013	9.755263
Gamma M	3x3	683096.9	678912.5	232775.8	0.710315	8.611698	382212.1	387952.2	146037.3	0.751985	6.849856
	5x5	684076.3	685371.4	203795.4	0.620991	11.26731	382485.7	402180.6	130989.2	0.674016	8.526276
	7x7	684627	685371.4	189594.6	0.577254	13.03936	382721.6	4074.361	124177.2	0.638571	9.499089
Lee	3x3	690447.4	676925.7	231816.8	0.699858	8.870973	384129.5	392940.1	146009	0.748087	6.921435
	5x5	689383.6	693526.5	200354.3	0.605805	11.83926	384824.2	403480.4	131080.5	0.670387	8.61883
	7x7	689539.9	699439.1	185537.9	0.560878	13.8119	384990.3	408001.9	124283.5	0.635351	9.595615

Fig. 2.10. Tabulation for IHH and IHV Data with SSI values.

2.6 Conclusion

This chapter presents a comparative study between different speckle filters with different filter window size and their impact on speckle reduction. Amplitude/Intensity) images with different polarizations have been used for speckle reduction.

For the best speckle free image, K means the classification is applied. Fig 2.9 and Fig 2.10 show that the mean filter with window size 7*7 Intensity HH images shows the lowest SSI value. From this work, we can make out the importance of Speckle filtering for image classification [36-38]. The selection of the best speckle reduced image is mainly based on values like speckle suppression index (SSI), an equivalent number of looks (ENL), Speckle Suppression, and Mean Preservation Index (SMPI). The classified image is verified using Google maps. The following conclusions can be drawn from this study

- As speckle filter window size increases, Speckle in an image decreases. Similarly, as the filter window increases, smoothing of the edges and point target takes place.

- The selection of polarization data (HH-HV) can be made using SSI, ENL values, and visual interpretation.
- Selection of Amplitude or Intensity Image can be made using the above mentioned Indices.
- Selection for a Frost filter with less damping factor is preferred as the damping factor increases with filter window size SSI values. The low value of SSI indicates an effective filter.
- Intensity HH image for Median filter with 7*7 window has less SSI, SMPI, and high ENL value. Low SMPI value indicates better speckle reduction with mean preservation.

Chapter 3

Characterization of Targets using Polarimetric Target Decomposition Theorems

Contributions and citations of this chapter

Publication: 2

Citations: 5

3.1 Introduction

This chapter deals with the different types of polarimetric decomposition techniques. Various decomposition techniques are applied to the datasets to understand the polarized wave's scattering mechanism with each target in the scene. Quad pol Radarsat-2 data and Hybrid-pol RISAT-1 were opted for this study. Robust m chi, m delta decomposition, and pseudo three-component decomposition on Hybrid-pol data were utilized.

3.2 Polarimetric Decomposition

The process of extracting information about the scattering process using various techniques from full polarimetric SAR data is known as target decompositions. The first objective of decomposition theory is to express the scattering mechanism in the resolution cell is a sum of independent elements aiming to associate a physical mechanism to each type of scattering [39]. The main aim of target decompositions theorems is to interpret based on physical constraints, which are changed based on wave polarization. The average scattering is expressed as the sum of independent elements with each component.

There are two methods for model-based decomposition theorems: coherent and incoherent target decomposition. Coherent is suitable for coherent local target characterization, incoherent is for distributed target characterization.

3.2.1 Coherent Decomposition

This theorem was developed to characterize polarized scattered wave in which the information is contained in the scattering matrix. The scattering matrix is expressed as a sum of the elemental scattering matrix by using coherent averaging. Coherent averaging results in the generation of Speckle [40]. Krogager (1990) and Boerner (1996) contributed major work on coherent decomposition. Later, Corr and Rodrigues (2002) and Touzi and Charbonneau (2002) published many other decomposition methods.

3.2.2 Incoherent Decomposition

Most of the targets on the earth's surface are disturbed heterogeneously scattered. Therefore incoherent decomposition provides good results. Incoherent decomposition is further categorized into Eigen value/Eigen vector decomposition, model-based decomposition, and Hybrid Eigen value/Model-Based Decompositions. Polarimetric decomposition can be classified into four main types [41-46].

- Coherent decomposition based on scattering matrix **S (**Pauli, Touzi, Cameron).
- Model-based decomposition of coherency and covariance matrix (Yamaguchi, Freeman, and Durden).
- Decomposition based on Eigen value or Eigen vector of coherency and covariance (H/A/Alpha, Vanzyl).

3.3 Study area and SAR Datasets

Vancouver is a Canadian province of British Columbia with latitude 49°28′27″ N and longitude 123°12′07″ W in the country of Canada and Que

The data used for this study is RADARSAT- 2 fine-beam polarimetric SAR (PolSAR) data, which contains HH, HV, VH, and VV polarizations. The center frequency at this beam mode is 5.4GHz, i.e., C-band, and the spatial resolution is 8 meters.

3.4 Methodology

Fig.3.1 shows the implementation of flowchart for generating polarimetric decomposed images of RADARSAT-2 full polarimetric data. RADARSAT-2 data are recorded in the form of a Scattering matrix(S) from which the coherency matrix T3 was extracted using Sentinel tool box software. The coherency matrix T3 contains all the polarimetric information. Most of the decomposition parameters were derived from coherency matrix T3, or covariance C3, which contains similar information, but in different form. Initially datasets are calibrated and the T3 matrix is generated for polarimetric speckle filtering and polarimetric decomposition. Polarimetric speckle filtering is performed using a refined lee filter. Filtered datasets are decomposed using several polarimetric decomposition operators. Using Speckle filtered T3 product as input, unsupervised polarimetric classification is performed to similar group pixels into classes. A detailed explanation of polarimetric decomposition, along with a related equation, is provided in subsequent sections.

3.4.1 Coherent Decomposition: Pauli Decomposition

Initially, the Hermitian coherency matrix is extracted for all the raw polarimetric SAR data and then filtered by the Refined Lee filter. The Pauli parameters are directly obtained as the diagonal elements of the coherency matrix T3. The three elements of Pauli decomposition corresponds to a primary scattering mechanism. $S_{hh} + S_{vv}$ represents single bounce scattering [41].

$S_{hh} - S_{vv}$ represents double-bounce scattering, and $S_{hv} + S_{vh}$ represents volume scattering. In comparison to other coherent decomposition methods, the Pauli decomposition is excellent for exposing natural targets but not ideal for highlighting man-made targets. Since the targets' total power is equal to that of the backscattering matrix, it is often used for preliminary representation. The Pauli parameters could present the most contrast between the land-cover/land-use classes representing single bounce is from bare soil, the double bounce is from buildings, and volume scattering is from forests, respectively.

$$[S]=\alpha\begin{bmatrix}1 & 0\\ 0 & 1\end{bmatrix}+\beta\begin{bmatrix}1 & 0\\ 0 & -1\end{bmatrix}+\gamma\begin{bmatrix}0 & 1\\ 1 & 0\end{bmatrix} \tag{3. 1}$$

Where $\alpha = {(S_{hh} + S_{vv})}/{\sqrt{2}}$, $\beta = {(S_{hh} - S_{vv})}/{\sqrt{2}}$ and $\gamma = \sqrt{2}s_{hv}$are the complex quantities

The α, β, γ components are represented as blue, red, green color after decomposition in the RGB image plane.

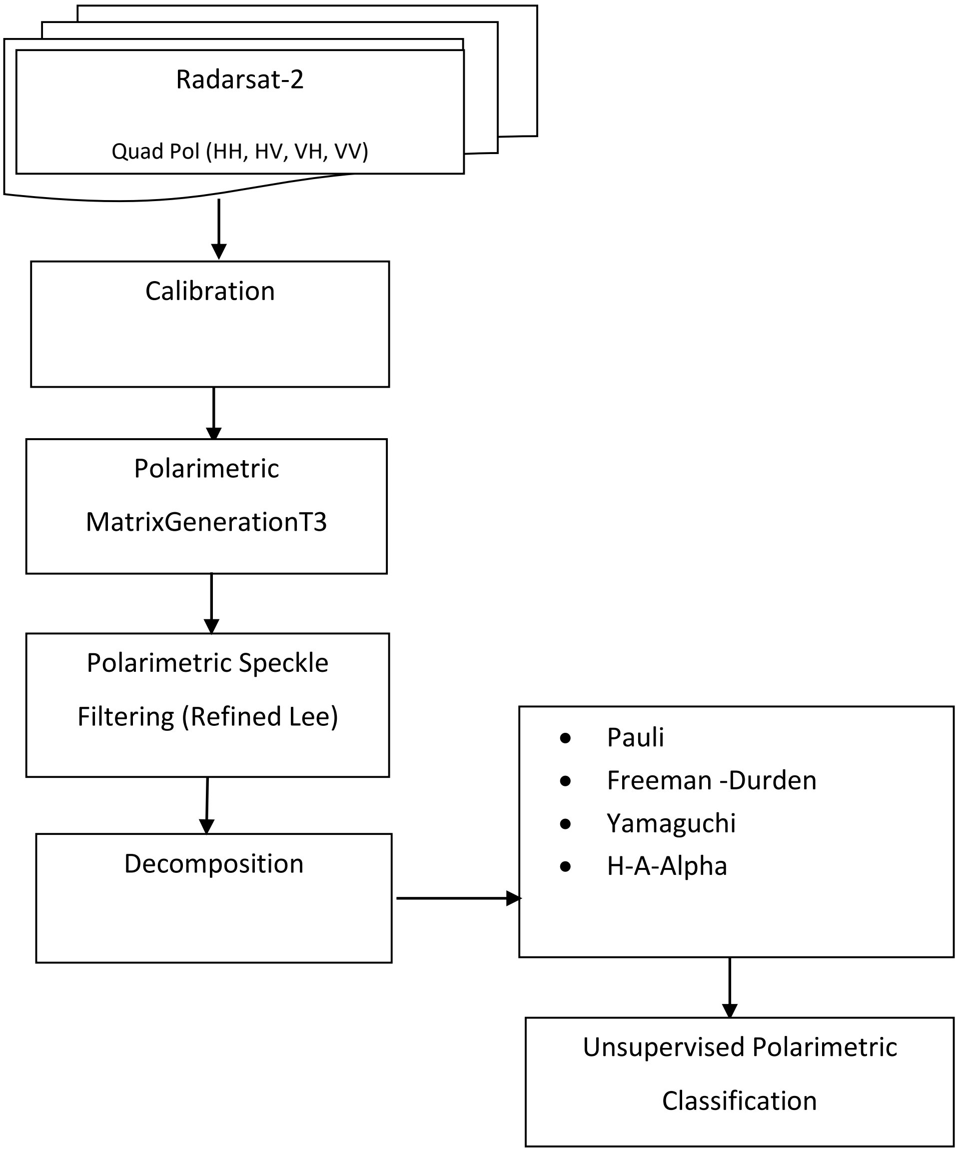

Fig. 3.1. Flowchart of the proposed work.

3.4.2 Model based Decomposition: Freeman- Durden Decomposition

The Freeman-Durden decomposition is a method for fitting a physically based, three component scattering mechanism model to polarimetric SAR observations. The three component scattering mechanism include surface scattering from a rough surface, double-bounce scattering from orthogonal surface, and volume scattering mechanisms from randomly oriented dipoles. The Freeman decomposition possesses similar characteristics to the Pauli-based decomposition, but Freeman decomposition provides a more realistic representation because it uses scattering models with dielectric surfaces. Since the Freeman-Durden method was intended to model the backscattering from forests, it might be invalid for other surface scatterings because of correlation coefficients [42-45].

$$T = P_s T_{surface} + P_d T_{double} + P_v T_{volume} \tag{3.2}$$

$$T_{surface} = \frac{1}{1+|\beta|^2}\begin{pmatrix} 1 & \beta & 0 \\ \beta^* & |\beta|^2 & 0 \\ 0 & 0 & 0 \end{pmatrix}, T_{double} = \frac{1}{1+|\alpha|^2}\begin{pmatrix} 1 & \alpha & 0 \\ \alpha^* & |\alpha|^2 & 0 \\ 0 & 0 & 0 \end{pmatrix}, T_{volume} = \frac{1}{4}\begin{pmatrix} 2 & 0 & 0 \\ 0 & 1 & 0 \\ 0 & 0 & 1 \end{pmatrix}$$

3.4.3 Yamaguchi Decomposition

Yamaguchi, in the year 2005, proposed a new technique which is an addition to Freeman Durden decomposition. Yamaguchi added the fourth component as helix scattering corresponding to non-reflection symmetric cases $\left\langle S_{HH} S_{HV}^* \right\rangle \neq \left\langle S_{HV} S_{VV}^* \right\rangle \neq 0$. This condition appears in heterogeneous (manmade structures). The concept of helix mechanism was developed by krogager in coherent decomposition [46]. Representation of Yamaguchi decomposition in coherency matrix is

$$T = P_s T_{surface} + P_d T_{double} + P_v T_{volume} + P_c T_{helix} \tag{3.3}$$

3.4.4 Eigen value-Eigen vector based Decomposition: H/α / A Decomposition

H/α/A decomposition was proposed by Cloude and Pottier for extracting average parameters from experimental data using a smoothing algorithm[9]. From the coherency matrix, T3 matrix decomposition parameters are generated from an eigenvector analysis. The eigenvectors describe different scattering processes, and the eigenvalues indicate their relative magnitudes. Among all the parameters, the averaged Alpha angle (α) relates directly to the underlying average physical scattering mechanisms. The value of Alpha ranges from 0° to 90°, which indicates the dominant scattering varies from surface scattering mechanism (0°), moving into single scattering (45°) by a cloud of anisotropic particles, and finally reaching dihedral scattering (90°). The Entropy (H) describes the randomness of the scatter. The anisotropy (A) corresponds to the relative power of the second and third Eigen vectors. The elements of the scattering matrix are defined as

$$[S] = \begin{bmatrix} S_{hh} & S_{hv} \\ S_{vh} & S_{vv} \end{bmatrix} \tag{3.4}$$

The coherency matrix is defined as

$$\langle T \rangle = \frac{1}{2}\begin{bmatrix} \left\langle |S_{HH}+S_{VV}|^2 \right\rangle & \left\langle (S_{HH}+S_{VV})(S_{HH}-S_{VV})^* \right\rangle & \left\langle 2S^*_{HV}(S_{HH}+S_{VV}) \right\rangle \\ \left\langle (S_{HH}-S_{VV})(S_{HH}+S_{VV})^* \right\rangle & \left\langle |S_{HH}-S_{VV}|^2 \right\rangle & \left\langle 2S^*_{HV}(S_{HH}-S_{VV}) \right\rangle \\ \left\langle 2S_{HV}(S_{HH}+S_{VV})^* \right\rangle & \left\langle 2S_{HV}(S_{HH}-S_{VV})^* \right\rangle & \left\langle 4|S_{HV}|^2 \right\rangle \end{bmatrix} \tag{3.5}$$

$$[\mathrm{U}_3]\begin{bmatrix}\lambda_1 & 0 & 0\\ 0 & \lambda_2 & 0\\ 0 & 0 & \lambda_3\end{bmatrix}[U_3]^{\dagger}$$

$$[U_3]=\begin{bmatrix}\cos\alpha_1 & \cos\alpha_2 & \cos\alpha_3\\ \sin\alpha_1\cos\beta_1 e^{j\delta_1} & \sin\alpha_2\cos\beta_2 e^{j\delta_2} & \sin\alpha_2\cos\beta_2 e^{j\delta_2}\\ \sin\alpha_1\cos\beta_1 e^{j\gamma_1} & \sin\alpha_2\cos\beta_2 e^{j\gamma_2} & \sin\alpha_3\cos\beta_3 e^{j\delta_3}\end{bmatrix} \tag{3.6}$$

Let λ_1, λ_2, λ_3 be the Eigen values of the coherency matrix and u_1, u_2, u_3 are the corresponding Eigen vectors.

$$u_i=\begin{bmatrix}\cos\alpha_i & \sin\alpha_i\cos\beta_i e^{j\theta_1} & \sin\alpha_i\cos\beta_i e^{j\lambda_1}\end{bmatrix}^T, \tag{3.7}$$

$$H=-\sum_{i=1}^{3} p_i\log_3(p_i), p_i=\lambda_i / \sum_{k=1}^{3}\lambda_k, A=\frac{\lambda_2-\lambda_3}{\lambda_2+\lambda_3}, \alpha=\sum_{i=1}^{3} p_i\alpha_i \tag{3.8}$$

3.5. Results and Discussions

The polarimetric decomposition methods discussed in the previous section are used over RADARSAT-2data, Quebec, and Vancouver city, Canada. All the polarimetric decomposition has their own pro and cons as related to its methodology implemented on the scattering matrix of a quad pol data. As the quad pol data is full polarimetric data retaining coherency between the channels, it is highly essential to apply polarimetric speckle filters preserving the phase information in the signal. Each component in all decomposition signifies the scattering mechanism pertaining to the target properties. However, the attempt of applying decomposition technique to exploit the utilization of full polarimetric data is appreciable as the conception of a smart city in developing countries has initiated its journey.

Fig.3.2 and Fig.3.3 represent the outputs of the images of Quebec and Vancouver city, respectively considered for the study. Google Earth images are shown in Fig.3.2 (a), 3.3(a) as a reference for the images considered. Fig.3.2 (b), 3.3(b) corresponds to Pauli decomposition images, where blue color indicates the single bounce scattering mechanism from targets like water bodies, green indicates volume scattering from vegetation, forest, etc., and red indicates double bounce from building manmade. Fig. 3.2 (c) and 3.3(c) are related to Freeman Durden decomposition images, where red indicates the power scattered by the double-bounce component of the covariance matrix, green indicates the power scattered by the volume scattering component and blue indicates the power scattered by the surface-like scattering component. This study has shown that the coherent decomposition parameters such as helix scattering, which operates on the individual pixels on a coherent basis, can also provide useful information for the land cover classification. Fig. 3.2 (d) and 3.3 (d) are the Yamaguchi decomposition images, which clearly show the helix scattering mechanism in urban areas compared to Freeman Durden decomposition because the urban areas are brighter due to the double bounce effect, which is represented in red color. Fig. 3.2 (e), 3.3(e) corresponds to H-α -A decomposition images, where red color indicates Entropy, green color indicates Anisotropy, and blue color indicates Alpha. As discussed in section 3, the value of α will determine the dominant scattering mechanism for every pixel. The Polarimetric unsupervised H-α Wishart classified images along with H-Alpha Plane plot with 9 classes are depicted in Fig. 2(f), (g) and 3(f), (g). The various classes are divided based on entropy and scattering angles into different targets like bare soil, wetland, water bodies, buildings, vegetation, etc. It is suggested that supervised classification, along with ground truth samples, will improve the classification accuracy. The ocean and the urban area, where much of the land surface is covered by roads and buildings, have a high degree of polarization values because the single scattering and double bounce scattering are dominant in these areas. This type of classification gives comprehensive information on existing resources to develop a better proposal in the establishment of a smart city.

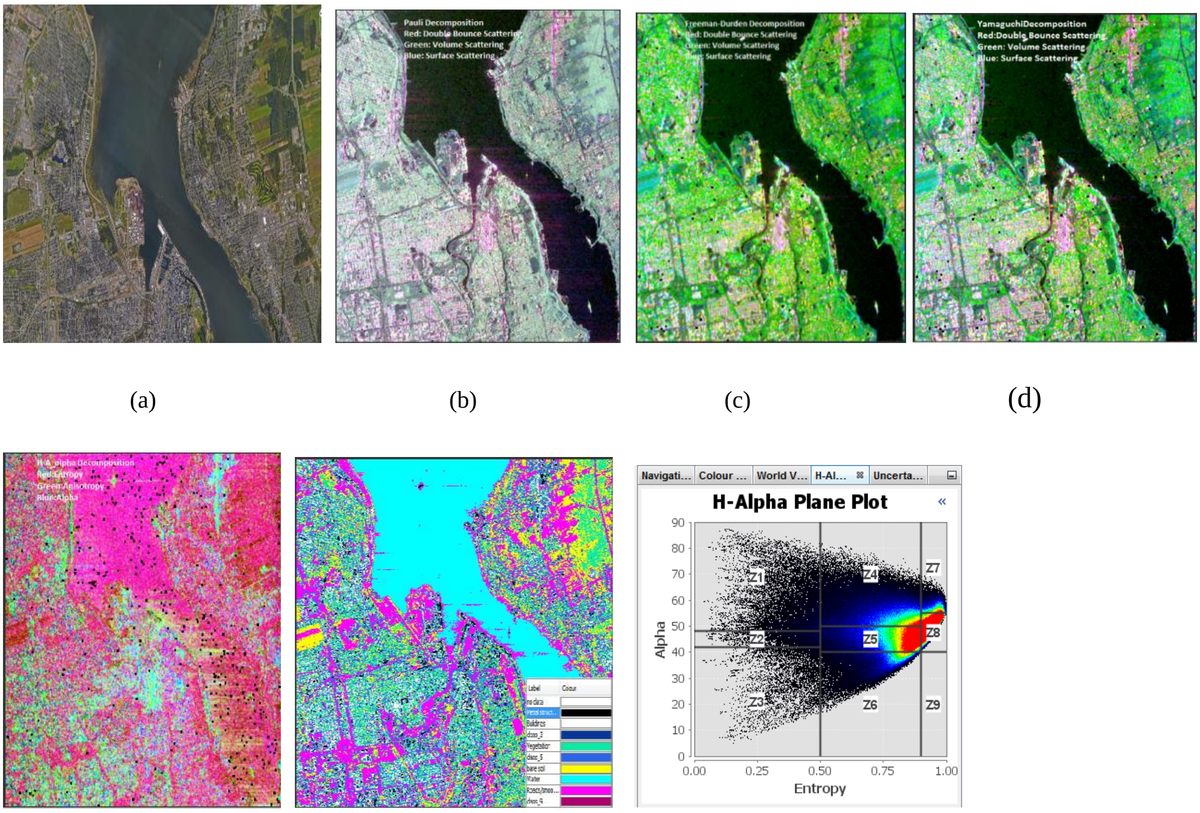

(a) (b) (c) (d)

(e) (f) (g)

Fig. 3.2: (a) Google Earth image of Quebec city ,(b) Pauli Decomposition, (c) Freeman Durden Decomposition, (d) Yamaguchi Decomposition, (e) H-A-α Decomposition, (f)) H-α Wishart Classification, (g)) H-α Plane.

Fig 3.2 output images of Quebec City

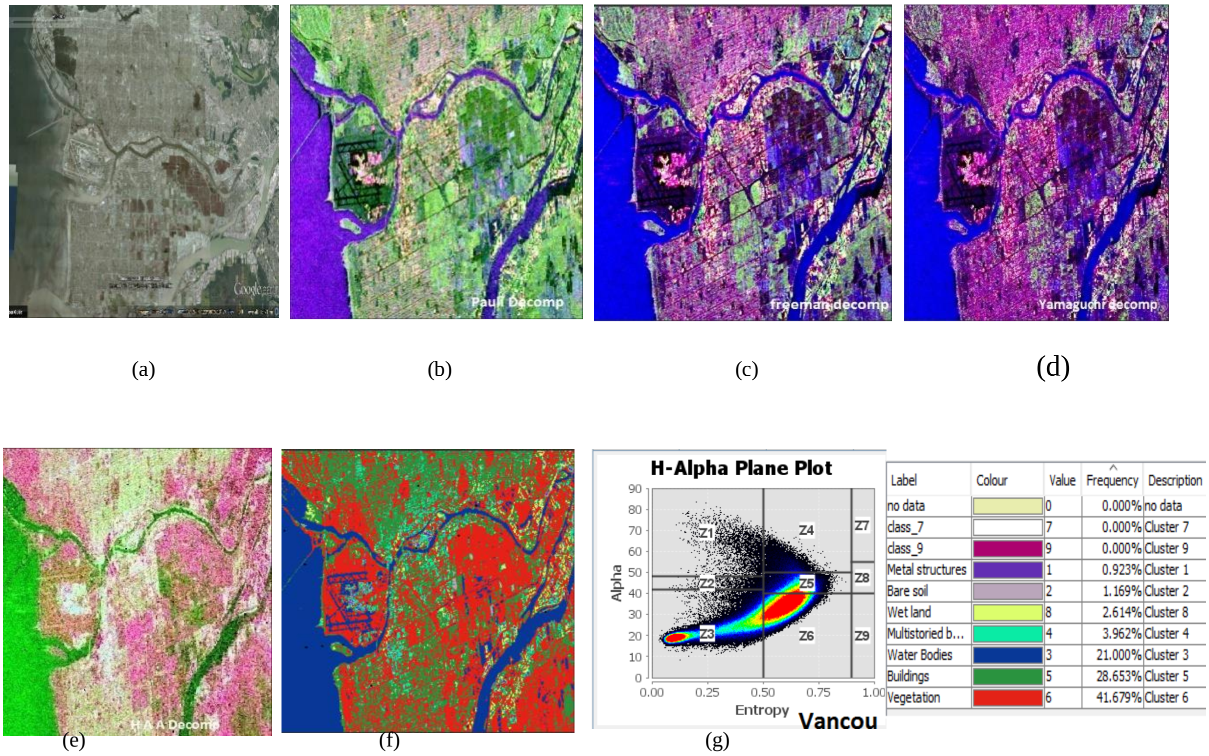

Label	Colour	Value	Frequency	Description
no data	🟨	0	0.000%	no data
class_7	⬜	7	0.000%	Cluster 7
class_9	🟪	9	0.000%	Cluster 9
Metal structures	🟪	1	0.923%	Cluster 1
Bare soil	🟪	2	1.169%	Cluster 2
Wet land	🟨	8	2.614%	Cluster 8
Multistoried b...	🟩	4	3.962%	Cluster 4
Water Bodies	🟦	3	21.000%	Cluster 3
Buildings	🟩	5	28.653%	Cluster 5
Vegetation	🟥	6	41.679%	Cluster 6

(a) (b) (c) (d)

(e) (f) (g)

Fig. 3.3: (a) Google Earth image of Vancouver city ,(b) Pauli Decomposition, (c) Freeman Durden Decomposition, (d) Yamaguchi Decomposition, (e) H-A-α Decomposition, (f)) H-α Wishart Classification, (g)) H-α Plane.

Fig 3.3 Output images of Vancouver city

3.5.1 Robust Hybrid Decomposition

Target Decomposition is only possible for a polarimetric image. Target decomposition cannot be performed for Dual-pol data. As RISAT-1 is a Hybrid polarimetric data, with the help of stokes parameters

Raney Decomposition

Raney decomposition was proposed by Raney. From Raney decomposition, six Raney derived parameters were obtained, i.e., i) Raney odd bounce, ii) Raney double bounce, iii) Raney random, iv) Raney-m, v) Raney-delta, vi) Raney-chi. From these derived parameters, along with the first stokes parameter (S_1), m-delta and m- chi decomposition were performed. Raney decomposition utilizes the first three parameters to construct an RGB composite image. Whereas m-chi decomposition utilizes 'm' and chi parameters from Raney decomposition and (S_1) from the first stokes parameter. Similarly, M-delta decomposition utilizes 'and delta parameters from Raney decomposition and (S_1) from the first stokes parameter.

m-delta(δ) Decomposition:

M delta is one of the child parameters derived from the stokes vector and was also found to be an important tool for polarimetric analysis. This technique was proposed and developed by Raney [47-51] using the principle as the relative phase difference between horizontal and vertical polarized backscatter signal gets the effect of each scattering. In this technique, the total intensity is segmented into polarized and unpolarized using a degree of polarization (m). The polarized part is subdivided into the even bounce and odd bounce by using the relative phase information. The unpolarized part is considered as volume component. In this decomposition from the color-coded image, red indicates single bounce, green represents volume component, and blue represents the double bounce.

$$\begin{aligned}
R &= \sqrt{S_1 m \frac{(1-\sin\delta)}{2}} \\
G &= \sqrt{S_1 (1-\mathrm{m})} \\
B &= \sqrt{S_1 m \frac{(1+\sin\delta)}{2}}
\end{aligned} \tag{3.9}$$

M Chi (χ) Decomposition

M Chi decomposition was proposed/developed by Raney [52-56]. The parameters degree of polarization 'm' and degree of circularity's.' [Circular polarization ratio and degree of linear polarization are the two-child parameters derived from stokes parameters. General decomposition techniques used for quad-pol data do not apply to hybrid polarimetric and dual-pol data because compact pol data and dual-pol data consist of the 2x2 covariance matrix. The degree of polarization' is a natural choice for the first decomposition variable for hybrid dual-pol data. The Poincare elasticity parameter χ is the best choice for the second decomposition variable. M Chi decomposition was tested on lunar orbiter mission, and this method was proven to be an excellent tool for hybrid polarimetric data. M and degree of circularity are the key inputs for m chi decomposition. In hybrid polarimetry for every scattering, the electric field loses its circularity and hence it is a principle of this technique. The unpolarized part is considered as volume component, and polarized part is categorized into odd and even bounce using χ. Blue color indicates single bounce (Bragg scatters), red indicates double bounce and green indicates randomly polarized constitute.

$$Sin(2\chi) = -\frac{S_4}{m} * S_1 \tag{3.10}$$

M chi decomposition can be expressed in a color-coded image where

$$\begin{aligned} B &= \sqrt{S_1 m \frac{(1-\sin\chi)}{2}} \\ G &= \sqrt{S_1(1-m)} \\ R &= \sqrt{S_1 m \frac{(1+\sin\chi)}{2}} \end{aligned} \tag{3.11}$$

Pseudo Three Component decomposition

Three- component compact decomposition was proposed by S.R Cloude, P_V is the volume component, P_S is the surface component and P_D is the dihedral component. Using the geometrical factor $(1 \pm \sin\delta)$ single component is split into two components i.e. dihedral and surface component. The split can be represented in the form of decomposition parameters as shown in eq. 3.12. A pseudo three component decomposition using a geometrical factor is shown in Eqn. 3.13. Where S_1 is the first stokes vector.

$$\tan\delta = \frac{S_4}{S_3} = \frac{\cos 2\alpha_s}{\sin 2\alpha_s \sin\phi} \tag{3.12}$$

$$\begin{bmatrix} P_D \\ P_V \\ P_S \end{bmatrix} = \begin{bmatrix} \frac{1}{2} S_1 m(1-\cos 2\alpha_s) \\ S_1(1-m) \\ \frac{1}{2} S_1 m(1+\cos 2\alpha_s) \end{bmatrix} \tag{3.13}$$

3.5.2 Results

Fig 3.4 (a), is the Raney derived RGB image on Hybrid-pol data, where red color indicates urban settlements, black color indicates water body, green color indicates vegetation, and white color indicates bare soil. Fig 3.4 (a) is the Raney derived RGB image on Dual-pol data, where green color indicates vegetation, black color indicates water bodies and red color indicates urban settlements and paddy fields.

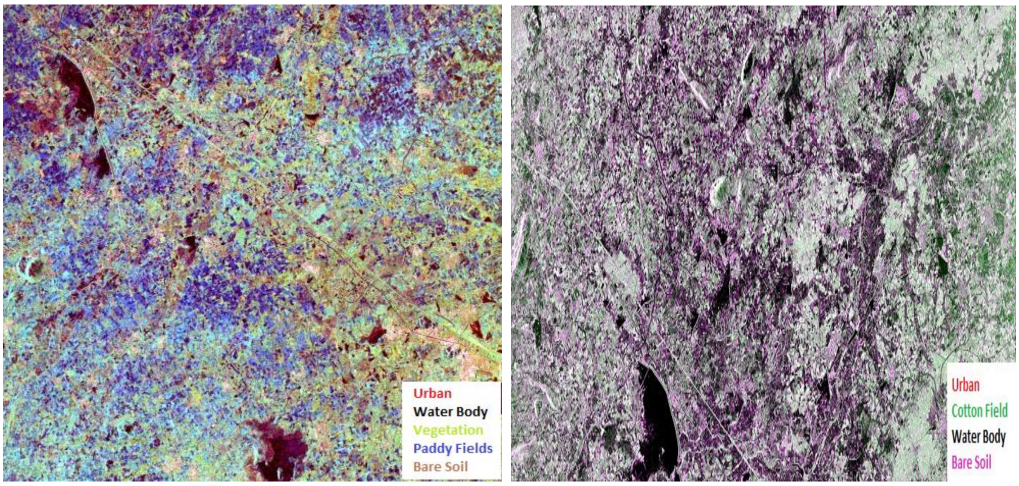

(a) (b)

Fig 3.4 Raney derived RGB image of Hybrid-pol and Dual-pol data

Fig 3.5(a), is the Pseudo compact decomposition performed on Hybrid-pol data. From this decomposition we obtain volume scattering, double bounce scattering and surface scattering. Where green color corresponds to the volume scattering from thick vegetation, red color Corresponds to the surface scattering from crop fields and water bodies, blue color corresponds to the double bounce scattering from urban settlements. Fig. 3.5 (b) and Fig. 3.5 (c) are the m-delta and m-chi decomposed images, respectively. From m-delta and m-chi decompositions, yellow color Corresponds to the double bounce from urban structures, i.e. buildings, green color Corresponds to the volume scattering from vegetation's. The magenta color Corresponds to the surface scattering from crop fields, bare soil and dark blue corresponds to water bodies. It was observed visually that m-delta and m-chi decomposition results were almost similar.

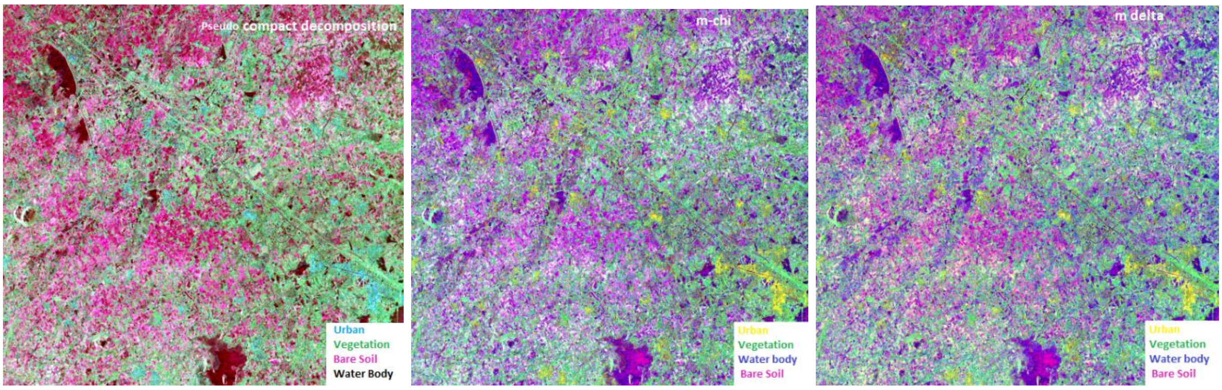

(a) (b) (c)

Fig 3.5 Pseudo compact-Pol, m-delta and m-chi decomposed images of RISAT-1 data

3.6 Conclusions

From this chapter, different polarimetric decomposition methods emphasize their excellence in determining the unique scattering properties pertaining to various terrain features. It was also observed that some polarimetric parameters have a more significant influence in distinguishing between natural and man-made objects. Yamaguchi decomposition performed good results, mainly in urban settlements due to the helix scattering components, followed by Freeman Durden decomposition. The H-α Wishart is used for polarimetric unsupervised classification based on the target scattering properties of land use/ land cover helps in the assessment of available and depleted resources(natural and man-made) for a better livelihood.

The hybrid Robust decomposition techniques were excellent in discriminating various land covers and various crops on hybrid-pol data. Raney RGB, m-delta, m-chi, discriminated cotton field from paddy fields very well.

Chapter 4

Improving the Overall Accuracy on Hybrid-pol Data using Various Machine Learning Algorithms.

Contributions and citations of this chapter

Publication: 2

Citations:

4.1 Introduction

In this chapter, various Supervised and unsupervised algorithms are explained in detail. In this chapter, SVM linear case, nonlinear, multi-class case are described in detail. SVM classifier was applied on Hybrid-pol and dual-pol RISAT-1 data. To validate the performance of SVM classifier on hybrid-pol data, SVM classifier was also applied on optical LISS IV data. The results obtained are almost similar. Further, SVM classifier was applied on dual-pol sentinel- 1B data for land cover, water body mapping and oil spill discrimination. For dual-pol Alos-Palsar-2 data SVM classifier was compared to the Wishart classifier the results obtained were almost similar.

In pixel based image classification- pixels are smaller than targets. Pixel is homogeneous in a target. In Image object based image segmentation: the pixel is smaller than the targets. Objects/classes are not homogeneous. In Sub-pixel classification- Pixel is larger than targets- pixel value is an area weighted combination of the targets. In pixel based classifier, there are different possibilities, and there are various algorithms that can be classified based on the type of learning like supervised and unsupervised. Classification is the task of assigning a given set of data (pixels) to a given class such that the cost of assigning is minimum [57]. The significant steps involved in image classification include feature extraction, selection of training samples, and finally, classifying the data using a suitable classifier. There are two types of classification techniques: parametric and non-parametric.

Furthermore, parametric classification can be performed in two approaches, i.e., supervised and unsupervised classification. In an unsupervised approach, an image is classified automatically by finding the clusters based on specific criteria. In a supervised approach, the analyst has to identify location and land cover type using field data (ground truth). Further, the analyst has to locate these areas on the remote sensing data, and these areas are known as training sites. In supervised technique, selection of training sets without ground truth data makes the analyst difficult and leads to poor classification. The classification procedure usually involves separating the data into training sets and testing sets. Fig 4.1. represents the types of classifier.

4.2 Parametric classifier

In this case, we assume a Gaussian distribution. The parameters, such as mean vector and covariance matrix, are generated from training samples. The size of the training sample does not matter to estimate parameters; as the dimensionality increases for fixed sample size, the accuracy of the parameters decreases. It cannot work effectively in hyper spectral data.

4.3 Non Parametric classifier

Assumption of the data is not required (Gaussian distribution). In this case, the classifier will not employ any statistical parameter to calculate class separation. This approach is suitable for incorporation ancillary data for improving the classification.

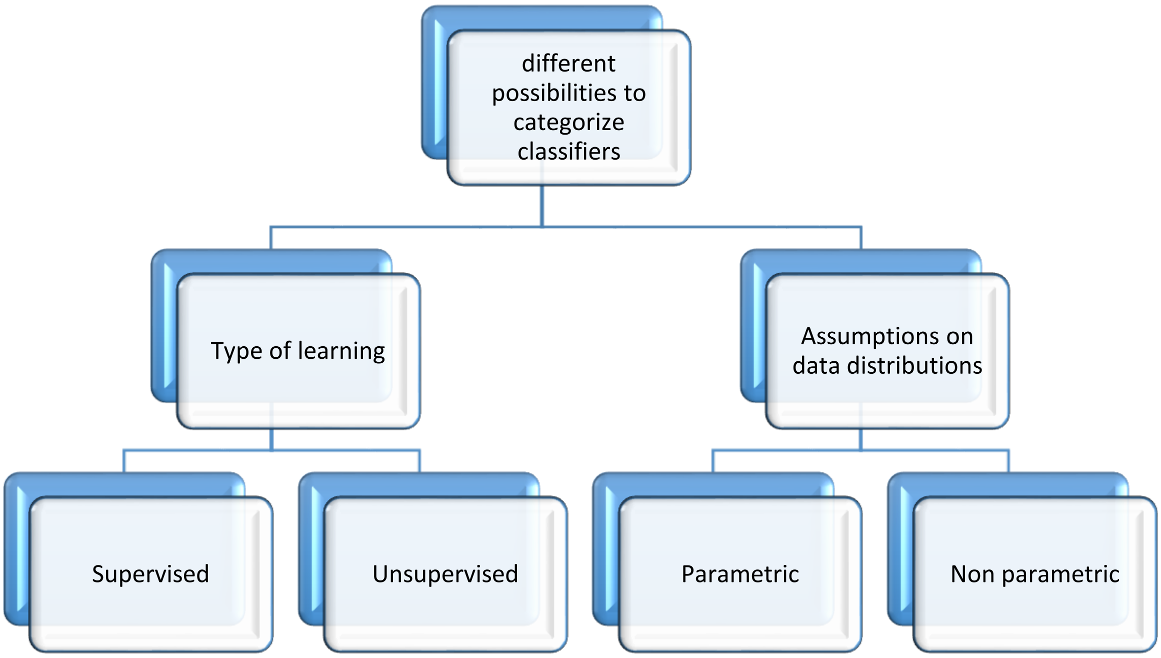

Fig 4.1 Types of Classifiers

4.3.1 Neural networks

Neural Networks' advantage is High computation rates and faster processing of huge volumes of data and better accuracy than conventional classifiers [57-60]. Hence, it's non-parametric; therefore, the assumption is not required for the data's statistical distribution. Unlike in the case of MLC, NN's performance depends on how well you train the data. NN can construct a nonlinear decision boundary; in MLC.

4.3.2 Parallelepiped classification algorithm

In the Parallelepiped decision rule, the candidate pixel's data file values are compared to the upper and lower limit. The limit can either be minimum and maximum data file values of each band in the signature. The mean of each band, plus and minus a number if standard deviation. Any limit that analysts specify or based on the knowledge of data and signatures.

Generally, in every band, there are high and low limits for every signature. Based on the pixels value limit, pixel will be assigned to a signature class. The high and low decision boundaries are defined as

$$L_{ck} = \mu_{ck} - S_{ck}$$
$$and \qquad (4.1)$$
$$H_{ck} = \mu_{ck} + S_{ck}$$

L_{ck} and H_{ck} are the lower and higher limit of class ‘C’ in band K.

μ_{ck} is the mean of the class ‘C’ in band K

S_{ck} is the standard deviation of the class ‘C’ in band K

Therefore, we obtain the lower limit by subtracting μ_{ck} and S_{ck} and higher limit by adding μ_{ck} and S_{ck}.

The parallelepiped algorithms becomes

$$L_{ck} \le BV_{ijk} \le H_{ck} \qquad (4.2)$$

Where BV_{ijk} is the brightness value of the Ith column and jth row in band K.

Advantages

Fast and simple and by giving broad classification, thus narrows down the number of possible classes to which each pixel can be assigned before more time-consuming calculations are made. It’s not dependent on a normal distribution.

Disadvantages

Since Parallelepiped has corners pixels that are far, spectrally from the mean of the signature may be classified.

4.3.3 Minimum Distance to Means Classification Algorithm

This algorithm is commonly used and is computationally simple. It requires mean vectors for each class in each band μ_{ck} from the training data. Euclidean distance is calculated for all the pixels with all the signature means

$$D = \sqrt{\left(BV_{ijk} - \mu_{ck}\right)^2 + \left(BV_{ijl} - \mu_{cl}\right)^2} \qquad (4.3)$$

Where μ_{ck} and μ_{cl} represents the mean vectors for the class c measured in bands k and l. Any unknown pixel will be assigned to one of many types; thus there will be no unclassified pixel.

Advantages

Since every pixel is spectrally closer to either one sample mean or other, so there are no unclassified pixels. The computational requires is fast.

Disadvantages

Pixels which should be unclassified will be classified and it does not consider class variability.

4.3.4 Mahalanobis Decision rule

Mahalanobis distance is similar to the minimum distance, except for the covariance matrix used in the equation. Variance and covariance are figured in such a way that clusters that are highly varied to similarly varied classes.

$$D = \left(X - M_c\right)^T \left(Cov_c^{-1}\right)\left(X - M_c\right) \tag{4.4}$$

Where D is the Mahalanobis distance

C is the particular class

X is the measurement vector of the candidate pixel

M_c is the mean vector of the signature of the class c

Cov_c is the covariance matrix of the pixel in the signature of the class C

Cov_c^{-1} is the inverse of Cov_c

T is the transposition function

Advantages

The algorithm takes variability of classes into account, unlike minimum distance or parallelepiped. It is more useful than minimum distance in cases where statistical criteria must be taken into account.

Disadvantages

The algorithm tends to over classify signatures with relatively large values in the covariance matrix. It is slower when compared to a minimum distance or parallelepiped. As the Mahalanobis distance is parametric, it relies on a normal distribution of the data in each band.

4.3.5 Maximum Likelihood/Bayesian Decision Rule

The maximum likelihood decision rule is based on the probability that a pixel belongs to a particular class [65]. The basic equation assumes that these probabilities are equal for all classes, and the input bands have a normal distribution. If the analyst have a prior knowledge, that the probabilities are not equal for all classes then we can specify weight factor for a particular class. The variation of the maximum likelihood decision rule is known as Bayesian decision rule (Hord, 1982)

$$g_i(x) = \ln p(w_i) - \frac{1}{2}\ln\left|\sum\nolimits_i\right| - \frac{1}{2}(x-m_i)^T \sum_i^{-1}(x-m_i) \tag{4.5}$$

Where

i= class

X= n- dimensional data (n is number of bands)

$p(w_i)$= probability that class (w_i) occurs in the image

$\left|\sum_i\right|$=determinant of the covariance matrix of the data in class (w_i)

m_i= mean vector

4.3.6 Support Vector Machine

SVM is a supervised non-parametric classification approach derived from statistical learning theory that often yields good classification results from the complex and noisy data [61-64]. As SVM classifiers fall under non-parametric classification, estimation of statistical parameters is not involved before classification, and therefore they are more appropriate for classifying Remote Sensing data. [66] The non-parametric approach's advantage is that they do not require one specific statistical distribution model; hence, they are versatile enough to be implemented in various data sets with minimal training sets. [67]. the main objective of SVM is to produce a model based on the training sets which can predict target values of the test sets. SVM classifier is well suited to handle linear non-separable cases using Kernel theory; therefore, SVM classifier was used effectively to hyper-spectral remote sensing data and SAR data.

A brief discussion regarding the SVM classifier can be found in [68-70]. SVM can be performed using either of the three approaches; 1) linear case, 2) Non-linear case 3) Multi-class case. SAR images can be classified into two stages: extraction of appropriate features and labeling the features based on a set of decision rules.

4.3.6.1 Linear Case

Let us consider a two-class classification with N-vectors of a training set from `d'-dimensional feature space for separating two classes. From the Fig. 4.2 (a ,b), two classes (vectors) are represented in red and blue color, the green color line which separates the two classes are called hyperplanes. The vectors which are close to the hyperplane are called as support vectors. The distance between support vectors and the hyperplane is called margin and is equal to 1/\omega whereas w refers to norm of vector. The objective of SVM is to compute optimum hyperplane by maximum margin and y finding minimum

$$\begin{aligned} &f(\mathrm{x}_i) = \omega \mathrm{x}_i + b \\ &\operatorname{sgn}[\mathrm{f}(\mathrm{x}_i)] = \mathrm{Y}_i \\ &Y_i(\omega \mathrm{x}_i + \mathrm{b}) > 0 \end{aligned} \tag{4.6}$$

The membership decision rule is based on the function $\operatorname{sgn}\left[f\left(x_i\right)\right]$

Newline in finding optimum hyperplane, we have to estimate Y_i where $Y_i\left(\omega x_i + b\right) > 0$

The optimization is performed using Lagrangian formalism

$$f(x) = \sum_{i=1}^{N} Y_i \alpha_i (x x_i) + b \tag{4.7}$$

Where α denotes Lagrange multiplier.

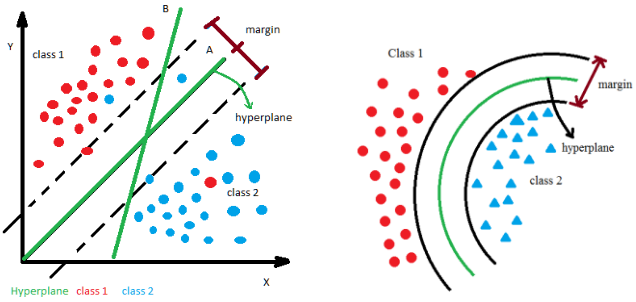

(a) (b)

Fig 4.2 a) linear b) non linear

SVM classifies the data into different classes by determining the set of support vectors that summarizes a hyperplane. SVM has a robust feature which ignores the outliners and finds the best hyperplane with maximum margin.

4.3.6.2 Non-Linear Case

The two classes are represented in red and blue color, the green color line which separates the two cassesbare called hyperline. In this case, the first step is to make a soft margin that adapts noisy data. The second step is the utility of kernel. Kernel is the function that simulates the projection of initial data in a feature space with higher dimensions $\phi = K^n \to H$. In this new space the data is consider as linearly separable by replacing the dot product $\left\langle X_i, X_j \right\rangle with \left\langle \phi(x), \phi(x_i) \right\rangle$

The new function to classify the data are

$$f(x) = sign\left(\sum_{i=0}^{N_s} y_i \alpha_i K \left\langle X_i, X_j \right\rangle + b \right) \tag{4.8}$$

Generally three kernel are used in this approach i) polynomial kernel, 2) sigmoid kernel, 3) RBF kernel. The polynomial kernel is represented as

$$K(X, X_i) = \left(\langle X.X_i \rangle + 1\right)^p \tag{4.9}$$

The sigmoid kernel and RBF Kernal are represented as

$$\begin{aligned} K(X, X_i) &= \tanh\left(\langle X.X_i \rangle + 1\right) \\ K(X.X_i) &= \exp^{-\frac{|X - X_i|^2}{2\sigma^2}} \end{aligned} \tag{4.10}$$

4.3.6.3 Multiclass case

The SVM classifier was designed for binary classification. To handle more than two problems or multi problems, there are different algorithms such as One against All (OAA) and One against One (OAO). OAA algorithm constructs K number of hyperplanes for K classes and separates K-1 classes. OAO algorithms constructs $\frac{k(k-1)}{2}$ hyper planes to separate each pair of classes.

4.4 Unsupervised classification

In this approach, the identities of land cover types to be specified as classes within a scene are generally not know prior. When the ground information/surface features are lacking the unsupervised approach is opted. The computer groups pixels with similar spectral characteristics into unique clusters with statistically determined criteria. Later, the analyst then combines and re-labels the spectral clusters into information classes.

4.4.1 ISODATA Clustering

Iterative Self Organizing Data Analysis Technique (ISODATA) represents a comprehensive set of heuristic procedures that have been incorporated into an iterative classification algorithm. This algorithm is a modification of the K means clustering algorithm, which includes rules for merging and splitting clusters.

ISODATA is iterative because it makes a large number of passes through the remote sensing dataset until specified results are obtained, instead of two passes. Isodata does not allocate its initial mean vectors based on the analysis of the pixels rather, an initial arbitrary assignment of all Comic clusters takes place along ab n dimensional vector that runs between very specific in the feature space.

4.4.2 K-Mean Clustering

K-means classification is an unsupervised classifier, where training sites is not required. Clustering algorithm is a method of cluster analysis which aims to partition of n observations into k clusters in which each observation belongs to the cluster with the nearest mean. K-means clustering algorithm also known as C-means clustering and has been applied to variety of areas including image and speech data compression. The objective function is defined as

$$W=\sum_{j=1}^{M}\sum_{i=1}^{N}\left|(E_i^{(j)}-V_j)^2\right| \tag{4.11}$$

Where$(E_i^{(j)}-V_j)^2$ is a distance measured between a data point$E_i^{(j)}$ and the cluster $V_j$is an indicator of the distance of the n data points from their respective cluster centres.

4.5 Results and Discussions

4.5.1 SVM classifier for RISAT-1 Hybrid-Pol and dual-pol data

Fig. 4.3 (a) and Fig. 4.3 (b) are the SVM classified images on Hybrid-pol RISAT-1 data and Dual-pol RISAT-1 data. Fig. 4.3 (a), 4.3 (b) are the SVM classifier image classified in 4 classes viz. urban, water bodies, vegetation and bare soil. Where red color corresponds to urban, green color corresponds to water body, blue color corresponds to vegetation and yellow color corresponds to bare soil. Fig. 4.4 a) is the optical LISS-IV image and Fig. 4.4 b) is SVM classified image on optical LISS-IV data, where blue color corresponds to water body, green color corresponds to vegetation, red color corresponds to bare soil, yellow color corresponds to urban.

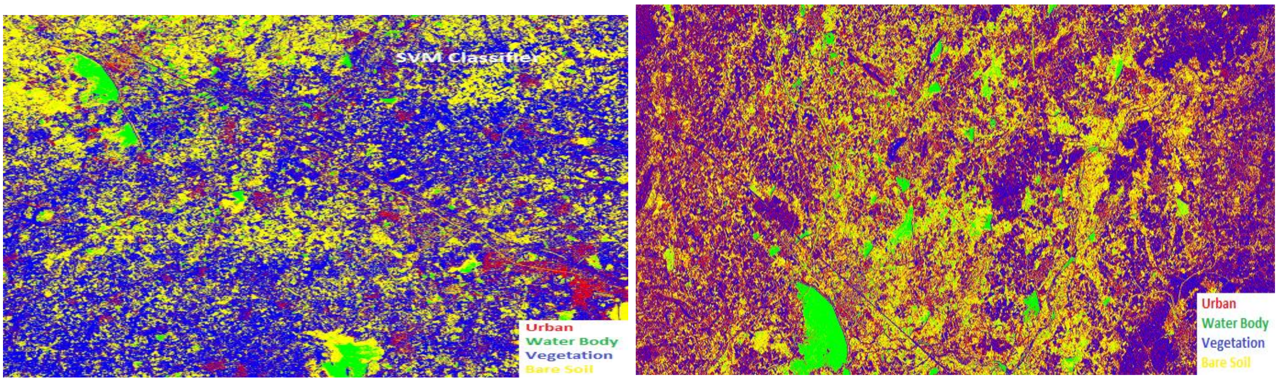

a) SVM classified images on Hybrid-pol RISAT-1 data b) SVM classified images Dual-pol RISAT-1 data

Fig 4.3 Hybrid-pol, Dual-pol RISAT-1 SVM classified images

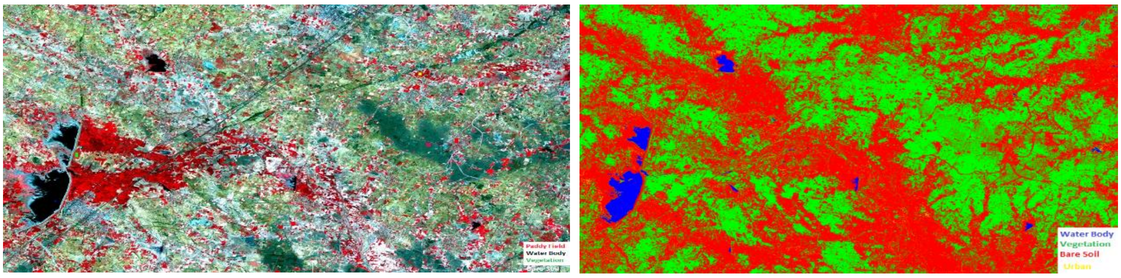

a) Optical LISS-IV b) SVM classified LISS-IV

Fig 4.4 LISS IV image and SVM classified LISS IV image

Table 4.1 represents the confusion matrix obtained for RISAT-1 Hybrid pol data, RISAT-1 Dual-pol data, and LISS –IV data using SVM classifier with RBF kernel parameter. We observe that (OA) 91.58 % for Hybrid pol data is more when compared to Dual-pol data 76.83 %. We also observe that RISAT-1 hybrid pol result and Optical LISS-4 results are almost similar.

	RISAT-1 Hybrid Pol				RISAT-1 Dual Pol				LISS-IV			
	U	WB	V	BS	U	WB	V	BS	U	WB	V	BS
U	80.70	0.00	18.83	0.47	56.66	0.00	35.32	8.02	86.69	0.01	00.00	45.08
WB	0.00	100	0.00	0.00	0.00	96.60	0.00	0.40	0.00	99.99	0.00	0.00
V	5.15	0.14	85.89	8.81	42.02	0.00	57.61	0.37	8.97	0.00	96.90	0.64
BS	0.00	0.17	0.09	99.74	2.89	2.58	1.07	93.46	4.34	0.17	0.06	54.28
OA	91.58%				76.83%				93.59%			

Table 4.1 comparison of Hybrid-pol, dual-pol and LISS-IV data for accuracy assessment using SVM classifier (RBF)

4.5.2 SVM classifier on dual-pol data

SVM classifier for Land cover classification, Water body mapping and Oil Spill Detection on Sentinel1-B data

Results of SVM

Fig 4.5 (a) and Fig 4.5 (b) are the VH and VV sigma naught images. From both figures, we can observe that cross-pol channel VH can be used for land applications, and co-pol channel VV can be used for ocean applications. From Fig 4.5 (b), we can easily identify the ships passage and oil spill. Fig 4.5 (c) and Fig 4.5 (d) are the histograms of VH and VV channels. Fig 4.5 (c) We can clearly observe that we have two peaks in the VH channel histogram, the large peak corresponds to the pixels on the land, and a smaller peak corresponds to the pixel over water surfaces. Fig 4.5 (d) shows three peaks for VV channel, which corresponds to water, land, and oil spill. From the Fig 4.5 (e) magenta color corresponds to VV backscatter and green color corresponds to VH backscatter these areas are likely to be vegetation because of volume scattering. The water bodies appears to have dark response, this is because of specular reflection in VV and VH channels. Magenta color represents crop fields (paddy fields), green color represents thick vegetation (forest), and the black color corresponds to the oil spill on oceans and water bodies on land. The bright response is from the urban area. Fig 4.5 (f) is the water body mapping image, where the white color represents the water bodies and the black color represents the land. As we have opted a VH cross-pol channel oil spill is not visible. Fig 4.5 (g) is the oil spill image, the white color represents oil spill and the black color is the masked area. Fig 4.5 (h) is the SVM classified image, the blue (aqua) color represents the water body, red color represents urban class, pink color represents oil spill, green color represents forest and the dark blue represents crop fields (paddy fields).

Waterbody mapping was performed after radiometric calibration, speckle filtering and terrain correction. From the backscattering values, we observe that the values are different for different classes. From the Fig 4.5 (c) histogram of VH the water body has a sigma naught values of -23 dB to -30 dB, and the land has a sigma naught values between -10 dB to -21 dB. To mask the water bodies, we have to find a suitable threshold value. Therefore by selecting sigma naught values less than -23 dB as threshold water body mapping can be performed.

Oil spill detection was performed after radiometric calibration, speckle filtering, and terrain correction. From the Fig 4.5 (d) histogram of VV channel, we have three peaks that correspond to land, water, and oil spill. The sigma naught values for land are -2 dB to -14 dB, for water, the values are between -16 dB to -24 dB, and for oil spill, the values are between -25 dB to -29 dB. Therefore selecting sigma naught value less than -26 dB as threshold oil spill detection can be performed.

	Water	Oil Spill	Forest	Crop field	Urban	PA
Water	98.67	1.33	0.00	0.00	0.00	98.67
Oil Spill	2.20	96.62	0.00	0.31	0.87	96.62
Forest	0.00	4.24	57.45	7.66	30.64	57.45
Crop field	0.00	0.29	2.01	86.51	11.19	86.51
Urban	0.00	1.66	9.21	13.21	75.95	75.95
OA						83.03

OA: Overall Accuracy, PA: Producer Accuracy

Table 4.2 Confusion matrix

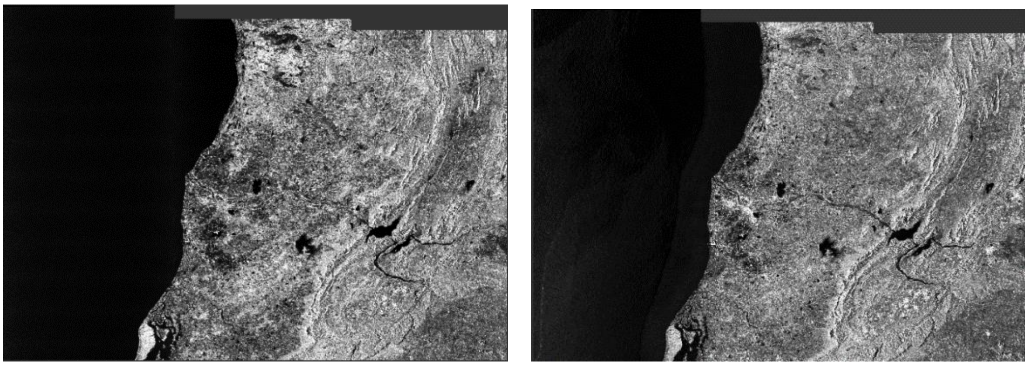

(a) Lee filtered VH Image

(b) Lee filtered VV Image

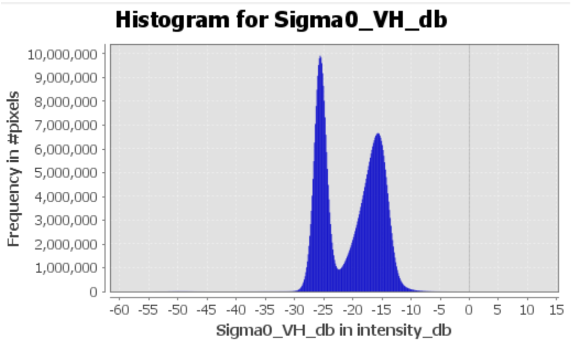

(c) Histogram of VH channel (d) Histogram of VV channel

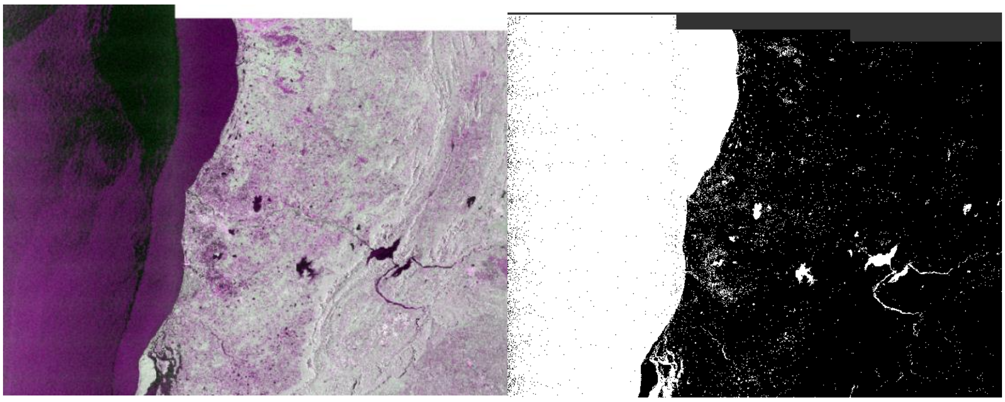

(e) GB (FCC) Image (f) Water Body Mapping Image

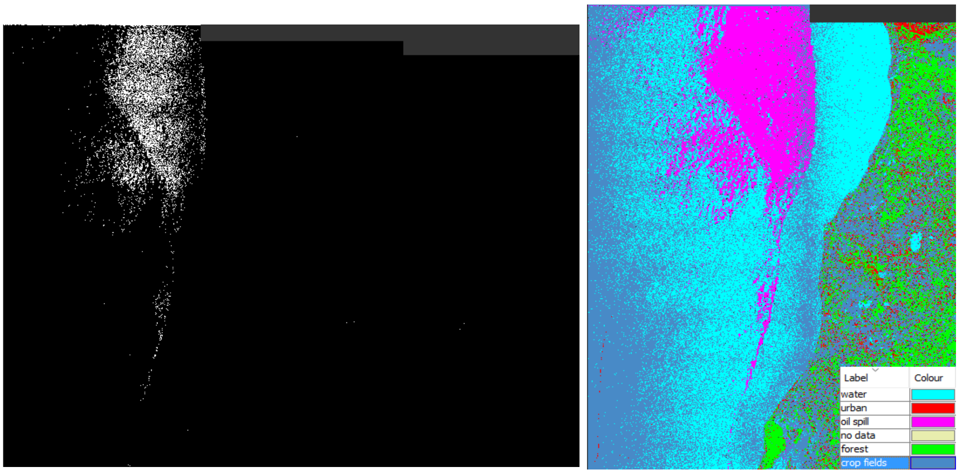

(g) Oil Spill Image (h) SVM Classified Image

Fig 4.5 Results of filtered, waterbody mapping, oil spill detection and SVM classified Images.

Table 4.2 is the confusion matrix obtained from the classification output for accuracy assessment. SVM classified the class water to 98.67% and the remaining 1.33% was classified as oil spill. Oil spill was classified to 96.62% and the remaining 2.20%, 0.3%, 0.87% were classified as water, crop field and urban. Forest was classified to 57.45% and the remaining 4.24%, 7.66%, 30.64% were classified as oil spill, crop fields and urban respectively. The classifier has misclassified urban to forest because of its vertical orientation. The Crop field was classified to 86.51% and the remaining 0.29%, 2.01% and 11.19% as oil spill, forest and urban respectively. The urban class was classified to 75.95% and the remaining 1.66%, 9.21% and 13.21% was classified as oil spill, crop field and forest. The Producer Accuracy (PA) for water, oil spill, forest, crop field and urban are 98.62%, 96.62%, 57.45%, 86.51% and 75.95%. The overall accuracy for SVM classifier was 83.03%. For validation the classified results were compared to the optical Sentinel 2A and Google Earth.

4.5.3 Comparison of SVM vs Wishart classifiers

Results

Fig 4.6 (a) is the SLC image of level 1.1 without multilooking, Fig 4.6 (b) is the multilooked image, 5 looks in range and 1 look in azimuth direction. Fig 4.6 (c) is the refined lee filtered image with window size 3x3. Fig 4.6 (a-c), magenta color corresponds to urban class, green color corresponds vegetation class, blue color corresponds crop fields, and black color corresponds to water body. Fig 4.6 (d) is the SVM classified image, where red color corresponds to urban class, green color corresponds water body class, blue color corresponds crop fields, and yellow color corresponds to forest, and orange color corresponds to bare soil. Fig 4.6 (e) is the Wishart classified image, where red color corresponds to urban class, green color corresponds water body class, blue color corresponds crop fields, and yellow color corresponds to forest, and orange color corresponds to bare soil. From Fig 4.6 (d) and Fig 4.6 (e), the urban class was better classified using SVM classifier.

From the Table 4.3, SVM has classified the urban class 98.37% better than Wishart classifier 96.85%. SVM and Wishart classifiers classified water bodies to 100%. Wishart classifier has classified crop field class to 94.4% better than SVM classifier 92.75%. SVM has classified the forest class to 81.71% better than Wishart classifier 72.21%. Wishart classifier has classified bare soil class to 91.90 % better than SVM classifier 82.61%. On a whole SVM and Wishart supervised classifier, Overall Accuracy were almost similar (91.08% and 91.07%).

	U		WB		C F		F			B S	
	W	S	W	S	W	S	W	S		W	S
U	96.8	98.3	0.0	0.0	3.1	0.6	0.0	0.6		0.0	0.2
WB	0.0	0.0	100	100	0.0	0.0	0.0	0.0		0.0	0.0
C F	0.0	0.0	0.0	0.0	94.4	92.7	2.9	0.6		2.6	6.6
F	0.0	0.0	0.0	0.0	0.6	0.0	72.2	81.7		27.1	18.2
BS	0.0	0.2	0.0	0.5	0.4	4.6	7.6	12.0		91.9	82.6
OA	Wishart: 91.076			SVM: 91.088							
U:Urban, W: Water Body, CF: Crop Fields, F: Forest, BS: Bare Soil, OA: Overall Accuracy, W: Wishart Classifier, S: SVM Classifier											

Table 4.3. Confusion Matrix for Accuracy Assessment

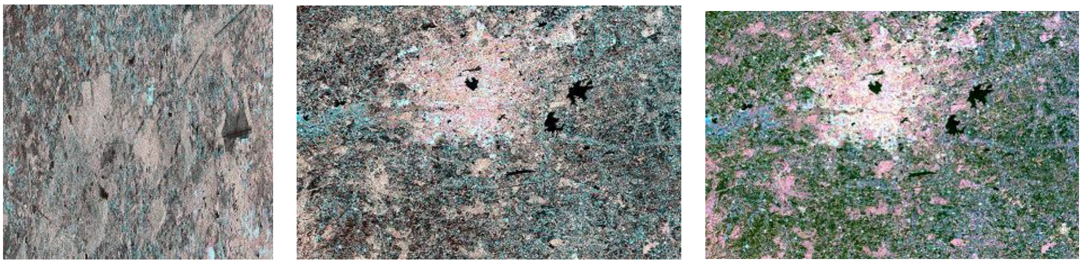

Fig 4.6 (a) SLC

Fig 4.6 (b) Multilooked

Fig 4.6 (c) Refined Lee Filtered

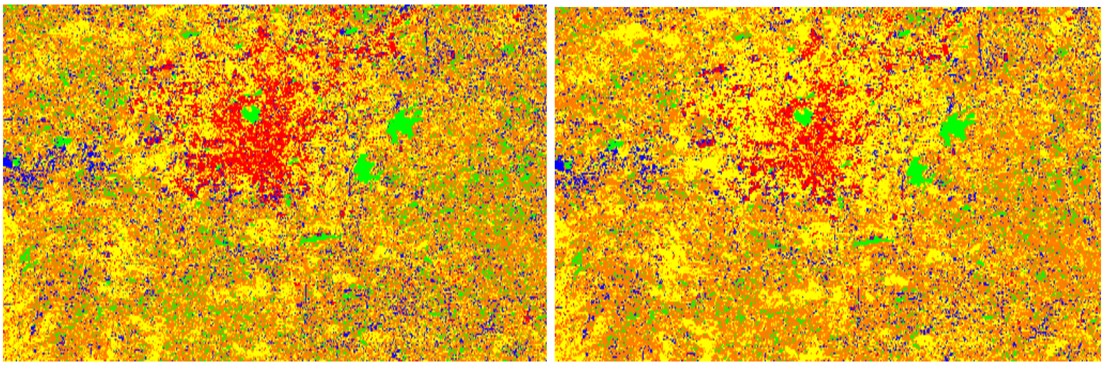

Fig 4.6 (d) SVM classifer image

Fig 4.6 (e) Wishart Clasifer

Fig 4.6 Processing of Alos-Palsar -2 dual-pol data

4.6 Conclusion:

SVM classifier gave an excellent overall accuracy on RISAT Hybrid-Pol data and on optical LISS-IV data. SVM has been classified into four classes with an OA of 91.58 % and 93.59%, respectively.

SVM, when applied on dual-pol systems when co and cross-polarization are available, co polarization (VV) channel enables better results for ocean applications. Similarly, Cross polarization (VH) enables better results for land application. From this study, we have observed the importance of co and cross-polarization. We have observed that the VV channel histogram has three peaks, but we have only two peaks in the VH histogram. The VV histogram shows that we have another peak for oil spill other than land and water peaks. This study has successfully presented water body mapping, oil spill detection, and land cover classification using sentinel 1B data. SVM has classified the dataset to an accuracy of 83.03%. The validation for the classified results was verified with optical data (Sentinel 2A and Google Earth).

When SVM was applied on L-band Alos palsar data and compared with Wishart classifier, from this study, we have explored the performance of L-band Alos palsar-1 data using SVM and Wishart classifier on metropolitan areas. In order to know the available natural resources around the city Hyderabad, LULC was performed. As L-band has more penetrating capability, the results for the SVM and Wishart classifier are almost similar. From Table 4.2, SVM has classified urban class well when compared to the Wishart classifier. The (OA) achieved on the data were 91.08% and 91.07% for SVM and Wishart classifier. The preprocessing was carried on POLSARPRO 5.0 version. The classified results were validated using Google Earth images and Ground Truth information.

Chapter 5

Exploring the Capability of Compact Polarimetry (Hybrid-pol) C-band RISAT-1 data over Dual-pol for land cover classification and crop identification.

Contributions and citations of this chapter

Publication: 2

Citations: 9

5.1 Introduction

This chapter specifies the credibility of compact polarimetry circular transmission over linear dual-pol and quad-pol data for land cover and Crop identification. This chapter aims to study and record the response of circular components from the targets over linear transmission. The second objective is to compare the three modes of Compact polarimetry.

5.1.1 Motivation: The motivation of this chapter came from the contributions of Raney et al., Souyris et al, Charbonneau et al., and M.E Nord et al.

5.1.2 Significance of Study: To explore the potential of compact polarimetry (hybrid-pol) for various applications.

5.1.3 Significance of the datasets and frequency: RISAT-1 is the only mission to have Hybrid Polarimetric architecture on board, and C-band has good signal penetration into the targets.

5.1.4 Novelty: In the literature, comparisons were made from the simulated hybrid-pol data. As the RISAT-1 has Dual-pol, Hybrid-pol data availability on the study area, investigations were performed.

5.1.5 Type of target: Rural

5.1.6 Application: Land Cover and Crop Discrimination

5.2 Radar Polarimetry

Radar polarimetry is the science of acquiring, processing, and analyzing the electromagnetic field's polarization state and is concerned with the utility of polarimetry for radar application. With recent advances in polarimetry, many upcoming SAR-based space-borne missions are planned to overcome the trade-off, such as polarimetry, resolution, and swath width [71-73]. From the past two decades, the concept of polarimetric SAR and its application has been an active research field. Radar polarimetry can be performed on two platforms, i.e., Space-borne and Airborne SAR systems, by providing high-resolution data in single, dual, and quad-pol data for the radar community. In general, a single pol system transmits and receives only one polarization, viz. horizontal (H) or vertical (V). Similarly, a dual-pol SAR transmits one polarization and receives the backscatter in a pair of orthogonal polarization viz. transmit (H) and receives (H, V) vice versa. In quad-pol SAR, two orthogonal polarizations H and V, are coherently transmitted and received. Complete polarimetric scattering information can be obtained from the target from quad-pol SAR, and hence, better analysis and classification can be performed [10].

5.3 Compact Polarimetry Overview

In a quad-pol SAR systems a pulse is first transmitted on one polarization, and all orthogonally polarized signals are received before the next signal is transmitted. Similarly, SAR transmits two orthogonal polarized pulses alternatively and receives backscattered signal simultaneously using two orthogonally polarized antenna thus by capturing all polarization information. This process doubles, pulse repletion frequency (PRF) and halves the swath width which is the limitation to the fully quad-pol SAR systems.

These limitations will have an adverse effect on the revisit time, which is an important factor for earth observation missions [74-75]. The tradeoffs between conventional single-pol linear systems and quad-pol systems is a dual-pol system, in which a single polarization is transmitted and receives two orthogonal polarizations, by overcoming the drawbacks of conventional linear polarization systems. To achieve better swath width and to reduce average peak power with simple architecture Compact polarimetry (Dual Partial Polarimetric mode) has been proposed [17]. The dual partial polarimetric mode was proposed by Souyris [17]. The information from the compact-pol SAR is almost similar to that of fully polarimetric SAR from the azimuthally symmetric scattering targets and was proved by Souyris et al. Raney et.al [13] drew a similar conclusion and also promoted the use of Hybrid SAR for its simpler architecture in contrast to the conventional SAR. Compact polarimetry is a technique which allows construction of pseudo quad-pol data from dual-pol SAR. Recently Compact polarimetry has gained more importance than fully polarimetric SAR by its advantages such as larger swath width, less power, and simple architecture. Compact polarimetry has proven its potential in distinguishing oil slicks, ship detection and in crop monitoring. Compact polarimetry has three modes as shown in Table 5.1and Fig. 5.1.

S.No	Mode	Tx/Rx(Transmitting/Reception)
1	π/4	45°/ (H, V)
2	CTLR (Hybrid)	RC/ (H,V)
3	DCP	RC/ (RC,LC)

H = Horizontal, V = Vertical, RC = Right Circular, LC = Left Circular

Table 5.1: Compact Polarimetry Modes

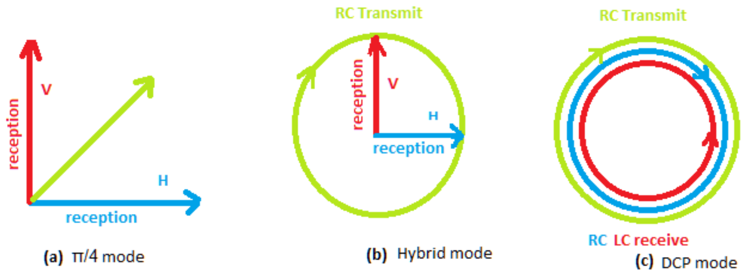

(a) π/4 mode (b) Hybrid mode (c) DCP mode

Figure 5.1: Illustration of CP modes

5.3.1 CP-Modes

$(\frac{\pi}{4})$ mode:

The $(\frac{\pi}{4})$ mode was one of the first partial polarimetric concepts to appear in the radar imaging literature developed by Souyris et.al [17]. In this mode, SAR transmits a linear polarized field at an angle of 45 concerning Horizontal or vertical orientation and receives Horizontal and vertical components [12, 13]. The covariance matrix is obtained from the Eqn. 5.1.

$$[C_{\pi/4}] = \frac{1}{2}\begin{bmatrix} |S_{HH}|^2 & (S_{HH}.S_{VV}^*) \\ (S^*_{HH}.S_{VV}) & |S_{VV}|^2 \end{bmatrix} + \frac{1}{2}\begin{bmatrix} |S_{HV}|^2 & |S_{HV}|^2 \\ |S_{HV}|^2 & |S_{HV}|^2 \end{bmatrix} + \frac{1}{2}\begin{bmatrix} 2\Re(S_{HH}.S_{HV}^*) & S_{HH}.S_{HV}^* + S^*_{VV}.S_{HV} \\ S^*_{HH}.S_{HV} + S_{VV}.S^*_{HV} & 2\Re(S_{VV}.S_{HV}^*) \end{bmatrix} \quad (5.1)$$

5.3.2 Dual circular polarimetric (DCP)

In this mode, right circular polarization is transmitted and both left and right circular polarization are received. Stacy and Preiss demonstrated that dual circular polarization could be implemented with slight modification from original compact polarimetry algorithm. The covariance matrix was obtained from the Eqn. 5.2.

$$[C_{DCP}] = \frac{1}{4}\begin{bmatrix} |S_{HH} - S_{VV}|^2 & -i(S_{HH} - S_{VV}) \\ i(S_{HH} + S_{VV}).(S_{HH} - S_{VV})^* & |(S_{HH} + S_{VV})|^2 \end{bmatrix} + \frac{1}{4}\begin{bmatrix} 4|S_{HV}|^2 & 0 \\ 0 & 0 \end{bmatrix} + \frac{1}{4}\begin{bmatrix} 4\Im((S_{HH} - S_{VV}).S_{HV}^*) & 2(S_{HH} + S_{VV})^*.S_{HV} \\ 2(S_{HH} + S_{VV}).S^*{}_{HV} & 0 \end{bmatrix}$$

..(5.2)

5.3.3 Circular Transmit Linear Receive (CTLR) Polarimetry

CTLR is popularly known as Hybrid polarimetry. In Hybrid polarimetry, only one polarization will be transmitted, and other orthogonal polarization will be received along with relative phase which is different from dual polarimetry systems. In this mode, Circular (right or left) component is transmitted and Linear component is Received (CTLR). In dual polarimetry systems, relative phase information is not available. Hybrid Polarimetry is the optimum architecture for applications related to planetary explorations and earth observations. SAR systems transmitting linear component may not be able to excite target response from linear structures as they are orthogonally oriented to the incident electric field [74-75]. Quad-pol SAR system is restricted in terms of incidence angle. In this case, by transmitting a linear component volume scattering is overestimated due to the change in orientation angle shift during reception of the signal from the target [76-78]. Therefore illuminating circularly polarized signal can overcome the limitation of linear transmitted systems. However, transmitting a circular component will not be affected by ionospheric distortions (Faraday rotation) and are free from the polarization orientation angle shift [79]. Hence, overestimation of volume scattering can be reduced when compared to quad-pol SAR system and another advantage of transmitting circular polarization is to reduce the range ambiguities [13]. Among circular transmit systems, Hybrid-pol is preferred over DCP because its performance is limited to weaker cross-polarized links and it is affected by additive noise and by crosstalk from stronger like polarized signal [13]. From hybrid-pol data, an equivalent covariance or coherency matrix may be reconstructed to produce pseudo quad-pol data. From the Eqn. 5.3 covariance matrix of hybrid-pol data was obtained.

$$[C_{CTLR}] = \frac{1}{2}\begin{bmatrix} |S_{HH}|^2 & i(S_{HH}.S_{VV}^*) \\ -i(S_{HH}.S_{VV}^*) & |S_{VV}|^2 \end{bmatrix} + \frac{1}{2}\begin{bmatrix} |S_{HV}|^2 & -i|S_{HV}|^2 \\ i|S_{HV}|^2 & |S_{HV}|^2 \end{bmatrix} + \frac{1}{2}\begin{bmatrix} -2\Im(S_{HH}.S_{HV}^*) & S_{HH}.S_{HV}^* + S^*{}_{VV}.S_{HV} \\ S^*{}_{HH}.S_{HV} + S_{VV}.S^*{}_{HV} & 2\Im(S_{VV}.S_{HV}^*) \end{bmatrix} \quad (5.3)$$

5.4 Hybrid Polarimetric SAR Architecture

Hybrid Polarimetry architecture is shown in Fig. 5.2. The hardware realization of hybrid polarimetry is in-complex as compared to that of linear full polarimetric systems. Both in active and passive case, the dual polarized antenna will transmit circular polarization only if H and V components are driven simultaneously. In this system, the same signal is transmitted through horizontal and vertical antenna such that phase 90° is maintained. Simultaneously during the reception, an additional pair of 90° hybrids in the receive paths is equired after the antenna or along each of receive chains. Hybrid polarimetry architecture has numerous advantages such as the generation of Stokes parameter from dual-pol data, less risk of crosstalk, calibration, less flight hardware, quad polarization transformation [13].

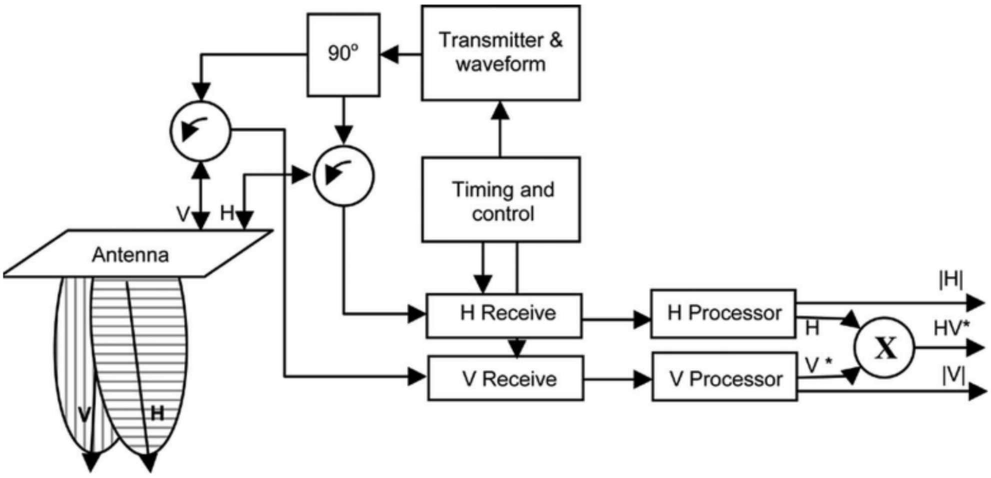

Figure. 5.2: Hybrid polarimetry Architecture @ Raney 2007 et al.

5.5. Study area and Datasets

In this study we have used RISAT-1 Hybrid pol data and Dual pol data and optical resourcesat-2 data for validation of classifed image as shown in Table 5.2 .

Mission/ Sensor	Polarization	Band /Freq	Mode	Incidence Angle	Res Rg	Res Az	Date of Acq Dd/mm/YYYY
RISAT-1	Dual Pol	C/ 5.04	FRS-1	46.59	3.33	1.80	5/12/2015
RISAT-1	Hybrid pol	C/ 5.04	FRS-1	39.57	3.33	1.80	05/07/2016
Resourcesat-2	3 bands	-	-	-	-	-	09/04/2016
Google Earth							

Table 5.2: Datasets

5.5.1 Ground truth

Ground truth data was collected on 4th and 5th of July 2016. Detailed information such as water level, crop yield progress, weather conditions were also recorded. On 4th and 5th July the study area was covered with clouds and had rainfall, during the time of acquisition. For better classification accuracy, ground coordinates for various target class were recorded with the help of hand-held GPS of Trimble Company. With the help of ground coordinates, training sites are given for supervised classification. Based on the ground truth, we have identified four classes (Urban, Water Body, Vegetation, Bare Soil).

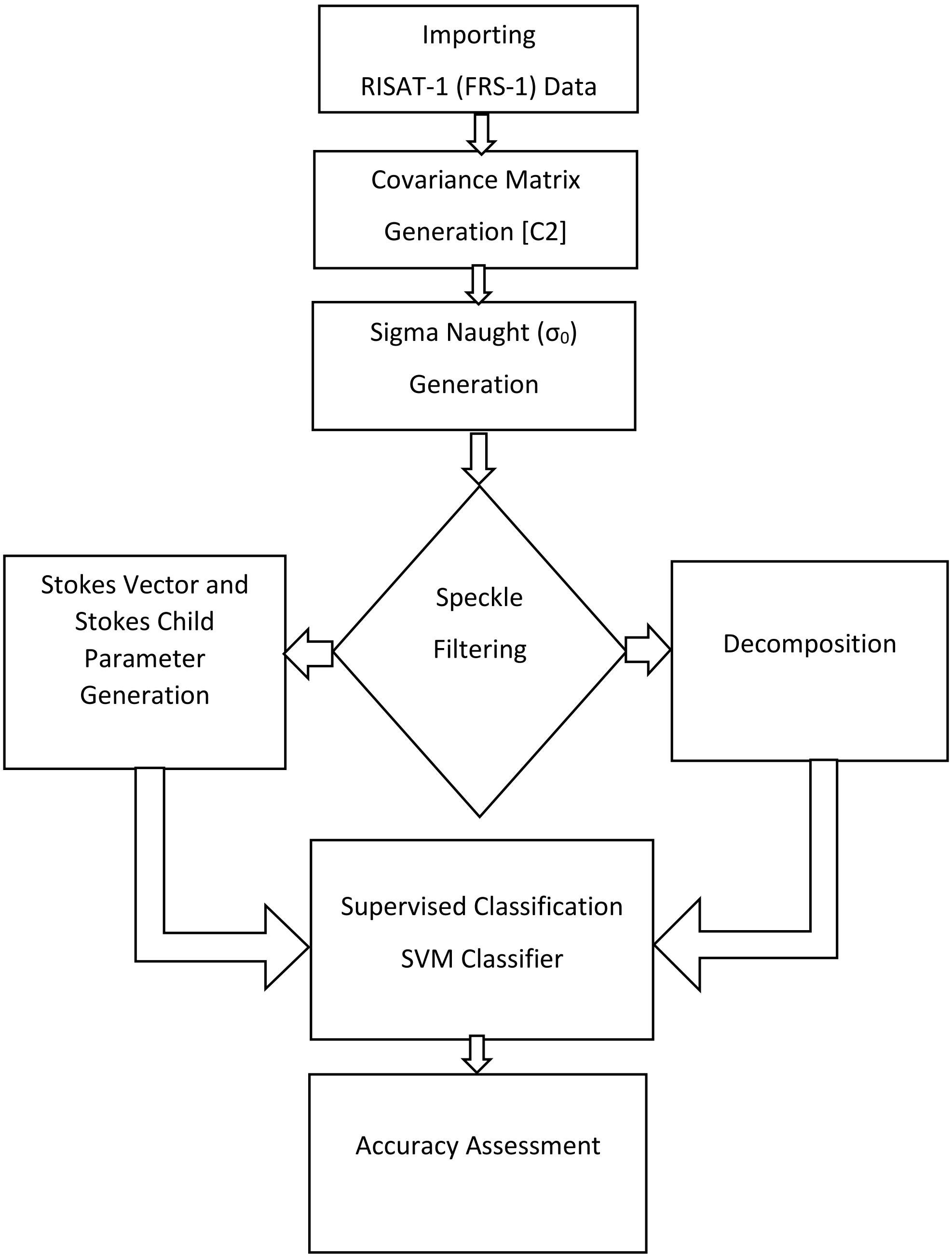

Fig. 5.3 Flow chart of the proposed work

5.6 Methodology

The flow chart of the propesed work in this chapter is shown in Fig 2.3.

5.6.1 Sigma naught image generation

Sigma naught image is generated using the equation (5.4).

Radiometric calibrations (backscatter calibration)

$$\sigma^0 \left(db \right) = 20\log_{10} \left(DN_p \right) - K_{db} + 10\log_{10} \left(\frac{Sin\left(i_p \right)}{Sin\left(i_c \right)} \right) \tag{5.4}$$

$\sigma^0 \left(db \right)$ = radar backscatter coefficient in dB

$\left(DN_p \right)$ Is the digital number are the image pixel gray-level count for the pixel p

K_{db} Is calibration constant in dB

i_p Incidence angle for the pixel position p

i_c Incidence angle at the scene centre

The calibration constant are obtained from the

Calibration of RH and RV channel

$$\begin{aligned} RH_{calib} &= RH_P{}^{*} sqrt\left[\left(10^\wedge(-KdB_{RH} / 10 \right)^{*} \left\{ \mathrm{Sin}\left(i_p \right) / \mathrm{Sin}\left(i_{center} \right) \right\} \right] \\ RV_{calib} &= RV_P{}^{*} sqrt\left[\left(10^\wedge(-KdB_{RV} / 10 \right)^{*} \left\{ \mathrm{Sin}\left(i_p \right) / \mathrm{Sin}\left(i_{center} \right) \right\} \right] \end{aligned} \tag{5.5}$$

RH_P RV_P are pixel values of original complex images

KdB Is the calibration constant of dB

i_p Incidence angle of the pixel position

i_{center} Incidence angle at the scene centre

Using the equation 5.4 and 5.5 backscattered coefficient σ^0 is processed

Hybrid-pol data has a 2*2 covariance matrix with phase information stokes vectors and child parameters are derived from the equation 5.6.

5.6.2 Stokes vector

$$\begin{aligned}
S_0 &= \left\langle |RH|^2 + |RV|^2 \right\rangle = \left\langle \left(I_{RH}^2 + Q_{RH}^2 \right) + \left(I_{RV}^2 + Q_{RV}^2 \right) \right\rangle \\
S_1 &= \left\langle |RH|^2 - |RV|^2 \right\rangle = \left\langle \left(I_{RH}^2 + Q_{RH}^2 \right) - \left(I_{RV}^2 + Q_{RV}^2 \right) \right\rangle \\
S_2 &= 2\Re \left\langle RH \cdot RV^* \right\rangle = 2 \cdot \left\langle I_{RH} \cdot I_{RV} + Q_{RH} \cdot Q_{RV} \right\rangle \\
S_3 &= -2\Im \left\langle RH \cdot RV^* \right\rangle = -2 \cdot \left\langle Q_{RH} \cdot I_{RV} - I_{RH} \cdot Q_{RV} \right\rangle
\end{aligned} \tag{5.6}$$

Where $|RH|^2$ Intensity of RH

$|RV|^2$ Intensity of RV

Class	Urban	Water body	Vegetati on	Bare soil
Sigma RH(dB) Hybrid Pol	-7.76	-20.69	-10.82	-11.31
Sigma HH(dB) Dual Pol	-2.09	-17.58	-18.59	-19.45
Sigma RV(dB) Hybrid Pol	-8.24	-18.33	-8.45	-13.15
Sigma HV(dB) Dual Pol	-15.61	-25.52	-16.52	-10.72

Table. 5.3 Sigma naught values for hybrid pol (RH, RV) and dual pol (HH, HV) RISAT-1 data

The values in Table 5.3, are the Sigma naught values of Hybrid-pol (RH, RV) and Dual-pol (HH, HV) RISAT-1 data. The training and testing samples of Hybrid-pol RISAT-1are shown in Table 5.4

Class	Training samples	No of Polygons	Test Samples	No of Polygons
Urban	4699	02	10097	05
Water Body	3355	04	9582	08
Vegetation	5005	02	17154	09
Bare Soil	1147	02	2403	03
OA	95.31%		91.58%	

Table 5.4: Training and Testing for Hybrid Pol RISAT-1 data

5.7 Results

Fig. 5.4 (a), is the Google Earth image, green color indicates vegetation, White Color indicates settlements, green color indicates water-bodies and brown color indicates bare soil. Fig 5.4 (b), is the FCC image of LISS-IV data, where red color indicates paddy fields, black color indicates water body, green color indicates vegetation, and white color indicates bare soil. Fig 5.4 (c), is the Raney derived RGB image on Hybrid pol data, where red color indicates urban settlements, black color indicates water body, green color indicates vegetation, and white color indicates bare soil. Fig 5.4 (d), is the Raney derived RGB image on Dual pol data, where green color indicates vegetation, black color indicates water bodies and red color indicates urban settlements and paddy fields.

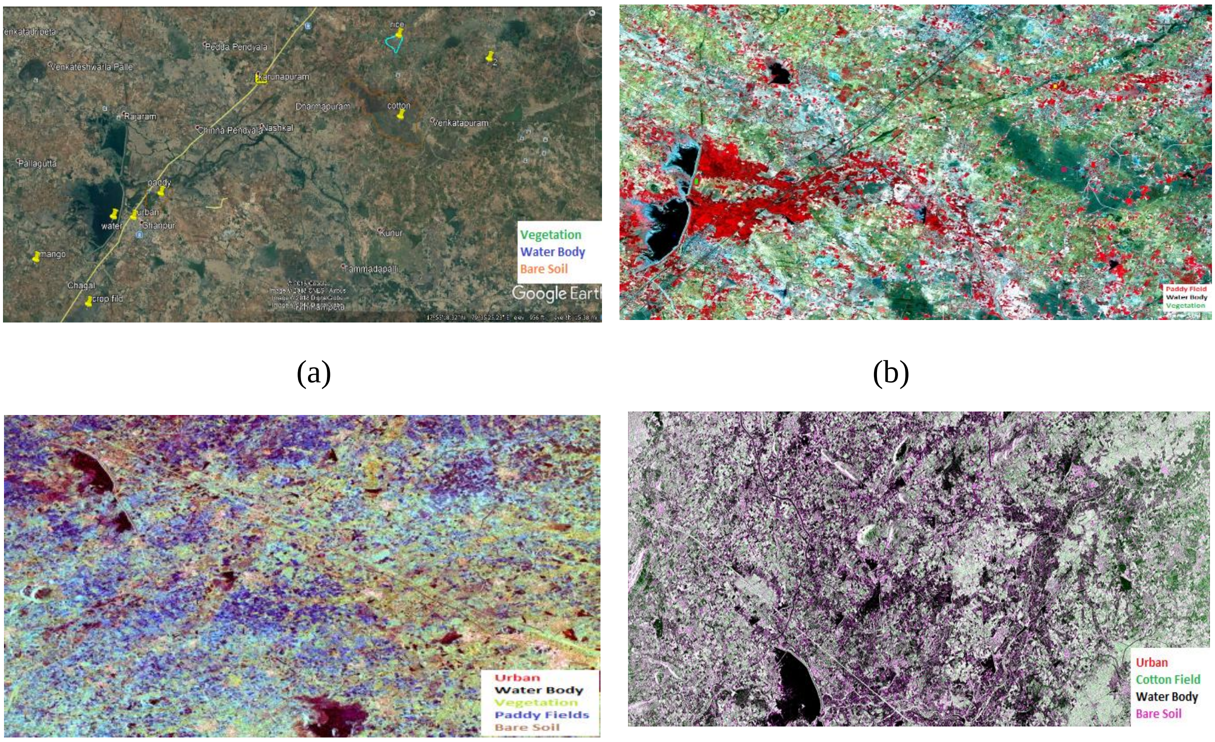

(a) (b)

(c) (d)

Fig 5.4 Images of Optical and Raney derived parameters of the Area of Interest. (a) Google Earths image. (b) Resourcesat-2 LISS- IV image (c) Raney derived RGB image on hybrid pol data. (d) Raney derived RGB image on dual pol data.

SVM parameterization

In this paper, the method of SVM is implemented by using the library LIBSVM on Polsarpro tool [97]. In this study, OAO approach has been retained with RBF kernel. The kernel parameters are tuned in the range of $C=\{8,16,32,64,128,256\}$ and $\gamma=\{0.03,0.06.0.12,0.25,0.5,1,2\}$. The cost parameter C and kernel parameter γ were optimized using cross-validation for obtaining best possible classification accuracy [80-82]. From fivefold cross validation, we have obtained the values of C=64, γ=0.5 with an accuracy 93.55 using grid search within a given set. While tuning the kernel parameters we have observed, as the values of C and γ increases the accuracy also increases. With a large values of C and γ

there is a tendency for the SVM to over fit to the training data. The cross validation procedure prevents the over fitting problem.

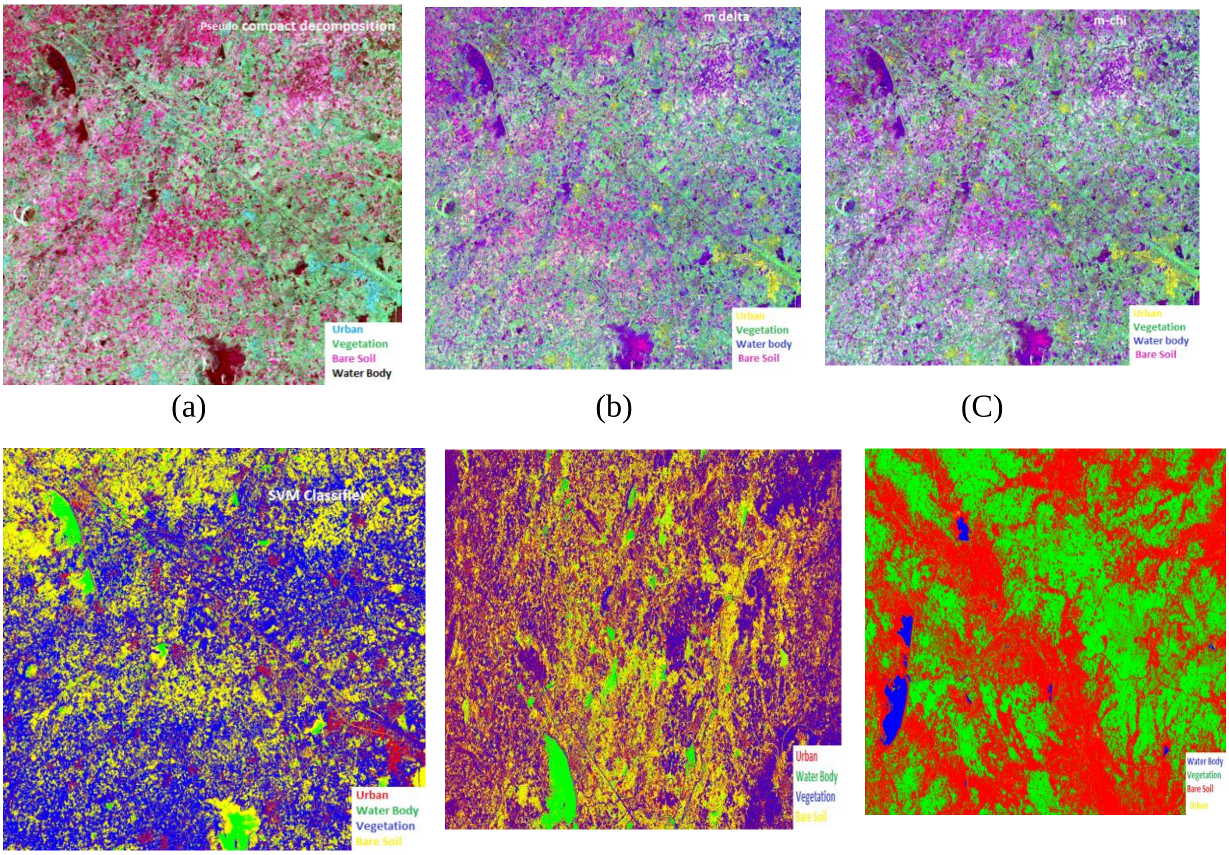

(a) (b) (C)

(d) (e) (f)

Fig 5.5 Processed images of SAR and optical data

Figure 5.6 Ground truth collection

Fig. 5.5 (a), is the Pseudo compact decomposition performed on Hybrid-pol data. From this decomposition, we obtain volume scattering, double bounce scattering and surface scattering. Where green color corresponds to the volume scattering from thick vegetation, red color corresponds to the surface scattering from crop fields and water bodies, blue color corresponds to the double bounce scattering from urban settlements. Fig. 5.5 (b) and 5.5 (c) are the m-delta and m-chi decomposed images, respectively. From m-delta and m-chi decompositions, yellow color corresponds to the double bounce from urban structures, i.e., buildings, green color corresponds to the volume scattering from vegetation’s. The magenta color corresponds to the surface scattering from crop fields, bare soil and dark blue corresponds to water bodies. It was observed visually that m-delta and m-chi decomposition results were almost similar. Fig. 5.5 d) and 5.5 (e) are the SVM classified images on Hybrid-pol RISAT-1 data and Dual-pol RISAT-1 data, where red color corresponds to urban, green color corresponds to water body, blue color corresponds to vegetation and yellow color corresponds to bares soil. Fig. 5.5 (e) is the SVM classified image on optical LISS-IV data, where blue color corresponds to water body, green color corresponds to vegetation, red color corresponds to bare soil, yellow color corresponds to urban [83-87]. The Table 5.5 represents the performance of kernel parameters for Land cover classification using SVM classifier. In this study, we have compared all kernel parameters (linear, polynomial, RBF) on the test data. In this paper, the method of SVM is implemented by using the library LIBSVM on Polsarpro tool. In this study, OAO approach has been retained with RBF kernel. The kernel parameters Cost Parameter (C) and kernel parameter (Gamma) are tuned. Table 5.6 represents the confusion matrix of the Hybrid-pol, dual-pol and LISS-IV data. Table 5.6 represents the cost parameterization effect with respect to accuracy.

	RBF				P ‘2’				L				CP
	U	WB	V	BS	U	WB	V	BS	U	WB	V	BS	
U	80.70	0.00	18.83	0.47	75.16	0.26	22.43	2.15	78.44	0.00	20.00	1.55	10097
WB	0.00	100	0.00	0.00	0.00	100	0.00	0.00	0.00	100	0.00	0.00	9582
V	5.15	0.14	85.89	8.81	3.64	0.32	86.41	9.63	4.34	0.18	85.95	9.53	17154
BS	0.00	0.17	0.09	99.74	0.00	0.17	0.17	99.39	0.00	0.17	0.35	99.48	2403
OA	92.34%				90.24%				90.96 %				

Kernel Types RBF: Radial Basis Function; P ’2’: Polynomial; L: Linear U: Urban Class; WB: Water Body, V: Vegetation; BS: Bare Soil

Table 5.5 Confusion matrix for Hybrid pol RISAT-1 SAR data using various Kernel parameters on test set

	RISAT-1 Hybrid Pol				RISAT-1 Dual Pol				LISS-IV			
	U	WB	V	BS	U	WB	V	BS	U	WB	V	BS
U	80.70	0.00	18.83	0.47	56.66	0.00	35.32	8.02	86.69	0.01	00.00	45.08
WB	0.00	100	0.00	0.00	0.00	96.60	0.00	0.40	0.00	99.99	0.00	0.00
V	5.15	0.14	85.89	8.81	42.02	0.00	57.61	0.37	8.97	0.00	96.90	0.64
BS	0.00	0.17	0.09	99.74	2.89	2.58	1.07	93.46	4.34	0.17	0.06	54.28
OA	92.34%				76.83%				93.59			

Table 5.6 Comparison of Hybrid pol, dual Pol and LISS IV data for accuracy assessment using SVM classifier (RBF kernel).

S.No	*C*	(γ)	Accuracy (%)
1	8	0.5	90.70
2	16	0.5	91.70
3	32	0.5	92.90
4	64	0.5	93.55
5	128	0.5	94.10
6	256	0.5	95.35

Table 5.7 Parameterization of cost parameter

	Alos-palsar Quad-Pol					RISAT-1 Hybrid-Pol				
	W	C	U	P	M	W	C	U	P	M
W	98.67	1.33	0.00	0.00	0.00	99.54	0	0	0	0.46
C	2.20	96.62	0	0.31	0.87	0.05	47.35	8.25	27.07	17.26
U	0	4.24	57.45	7.66	30.64	0.85	15.58	23.83	14.60	45.14
P	0	2.29	2.01	86.51	11.19	0	31.86	10.28	38.15	19.71
M	0	1.66	9.21	13.21	75.92	3.27	11.85	9.16	6.18	69.55
OA	83.03% (1656,1271,966,2091,2346)					55.6% (3053,2150,4096,2451,2752)				
Classes W:Water, C:cotton, U:urban, P:Paddy, M:Mango										

Table 5.8 Confusion matrix of RISAT-1 Hybrid-pol and Dual-pol for crop discrimination

Hybrid-pol data has discriminated the crops very well. For crop discrimniation, five land targets were identified namely Water, cotton, urban, paddy and Mango. SVM has classifed five classes very well in Hybrid-pol data than in Dual-pol data. The two seasonal crops cotton and paddy were clearly discriminated and classified in Hybrid-pol data. In dual-pol data, cotton and paddy were not discriminated and classified with respect to Hybrid-pol data. From Table 5.8, Hybrid pol data has obtained OA of 83.03% and dual-pol data has obtained OA of 55.6 %.

5.8 Polarimetric synthesis of Compact Polarimetry (CP) and the comparison of CP modes

In this chapter, a compact polarimetry mode is simulated from quad-pol Alos-Palsar-2 SAR data. By symmetry assumptions a quad pol data can be synthesized to a compact pol data. This chapter presents the comparisons of three modes of compact Polarimetry and to study the compact pol mode interaction with the targets.

5.8.1 Methodology

In order to study the three modes of compact polarimetry, we need to acquire quad-pol then simulate/ synthesis to compact-pol data [88-93]. Quad-pol data has to be synthesis to $(\frac{\pi}{4})$ mode, Hybrid mode and DCP mode. All the CP mode have to undergo multilooking, Speckle filtering, decomposition, classification, accuracy assessment then should be compared. Multilooking (6: 1 range and azimuth direction) is performed to reduce the speckle content and also allows us to obtain square pixel. Performing multilooking for a several time degrades the image quality. Lee filter with window size 7*7 reduced the speckle effectively, so decomposition is performed on the filtered image. HAA decomposition is performed to understand the scattering response of the target. As, the decomposed image consist valuable information, SVM classifier is performed. Accuracy assessment is done using confusion matrix. The flow chart of the proposed work is shown in Fig. 5.7.

5.8.2 Study Area and SAR Data

For this study we have opted Amazon forest, Brazil. The study area consists of the deforested part, short vegetation and dense vegetation. We have opted Alos palsar-1 quad-pol data. We would like to record the response of circular transmission on intracting the targets. The below images are the SLC level 1.1 images

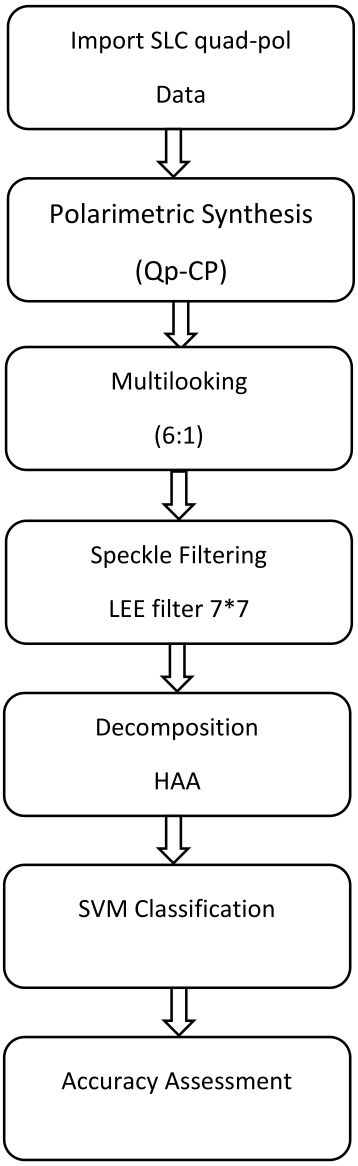

Figure 5.7 Flow chart of proposed section

5.9 Results and Discussion

Figure 5.8 is the SLC quad pol image with four channels, HH, HV, VH, and VV. Speckle in the images are clearly evident. Once multilooked is performed on the images, speckle is reduced in the images as shown in Figure 5.9.

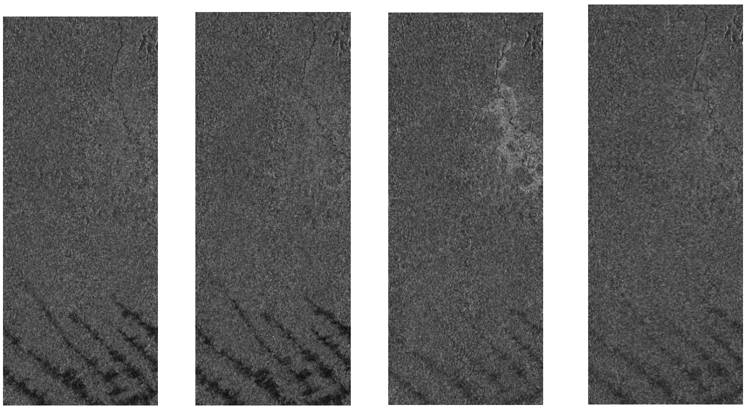

a(HH) b (HV) c (VH) d (VV)

Figure 5.8 Quad Polarization channels of Alos palsar-1 data

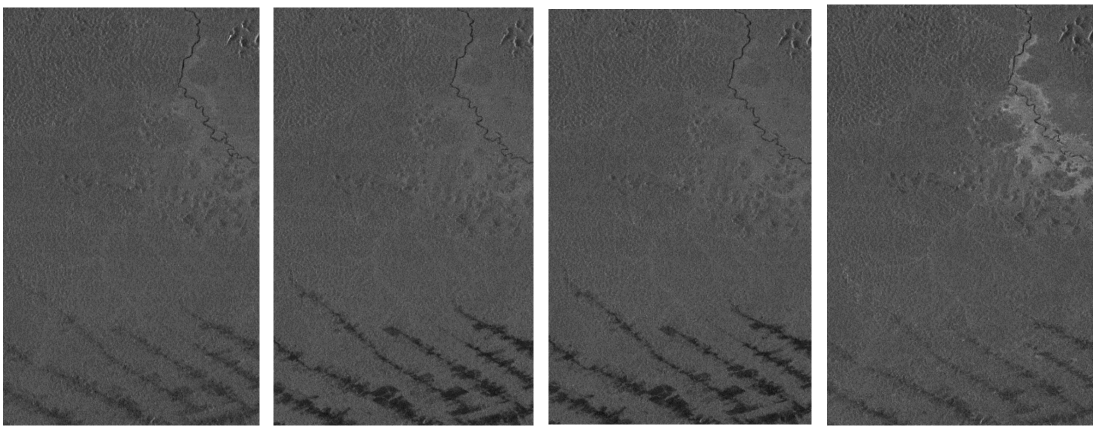

a(HH) b (HV) c (VH) d (VV)

Figure 5.9 Multilook Quad Polarization channels of Alos palsar-1 data

The Figure in 5.10 represents three chanels in ($\frac{\pi}{4}$) mode, cross pol HV channel gave a brighter response from short vegetation and the deforested area also gave specular reflection. Figure 5.11 represents three channels of elliptical mode. Visually we can make out the difference between ($\frac{\pi}{4}$) mode and elliptical mode. Figure 5.12 represents the three channel in $(\frac{\pi}{2})$ mode. Figure 5.13 represents the comparison of SVM classifier over $(\frac{\pi}{4})$ mode, elliptical mode and $(\frac{\pi}{2})$ mode. Visually elliptical mode gave good results, the short vegetation was very well classified in elliptical mode.

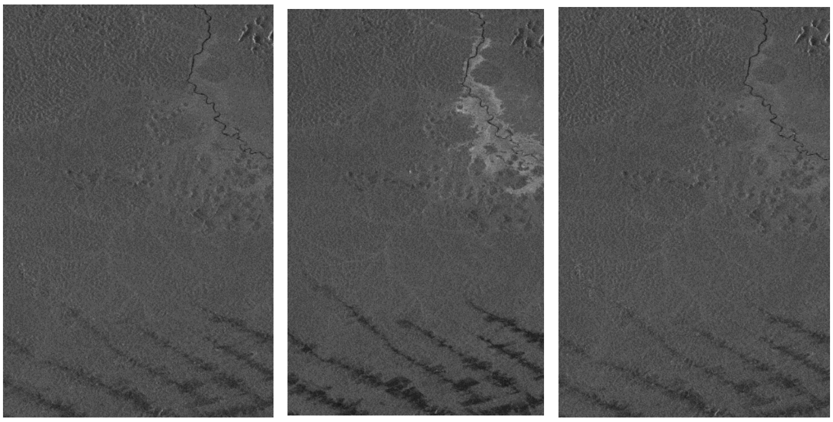

HH HV VV

Figure 5.10 Three channel image of $(\frac{\pi}{4})$ mode

Table 5.2: represents the SVM classifier Comparison of CP Modes, $(\frac{\pi}{4})$ mode gave OA of 86.31%, elliptical mode gave an OA of 85.78% and $(\frac{\pi}{2})$ mode gave an OA of 86.35 % as shown in Table 5.9. Where red color represents forest land, green color represents deforested land and blue color represents short vegetation. Short vegetation was better classified by elliptical mode. From the results all modes OA are almost equal.

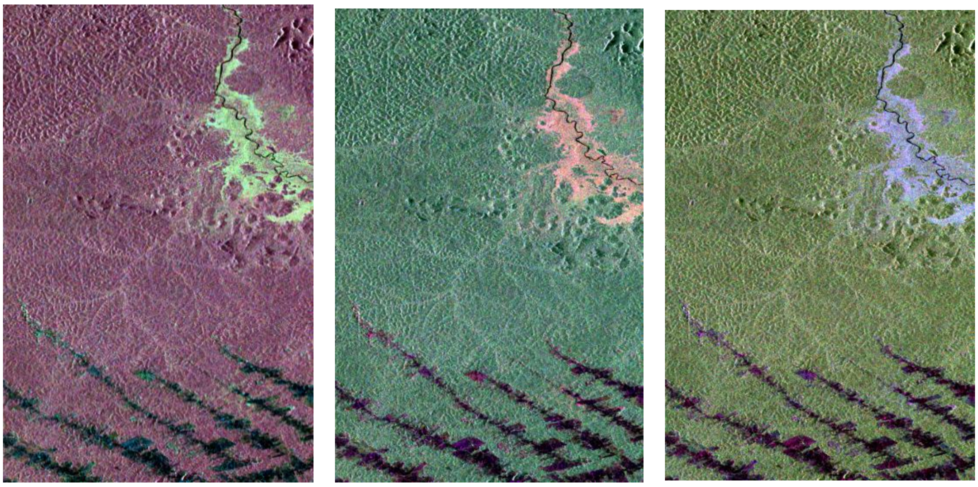

HH HV VV

Figure 5.11 Three channel image of elliptical mode

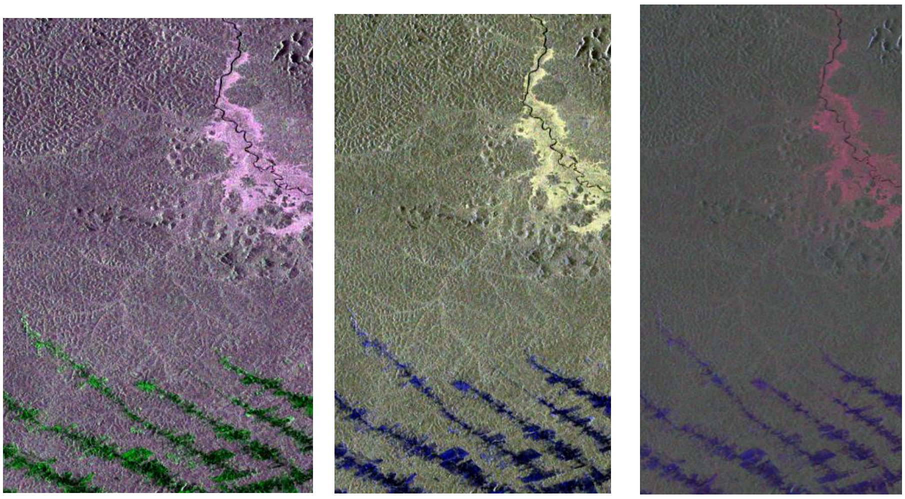

Figure 5.12 Three channel image of ($\frac{\pi}{2}$) mode

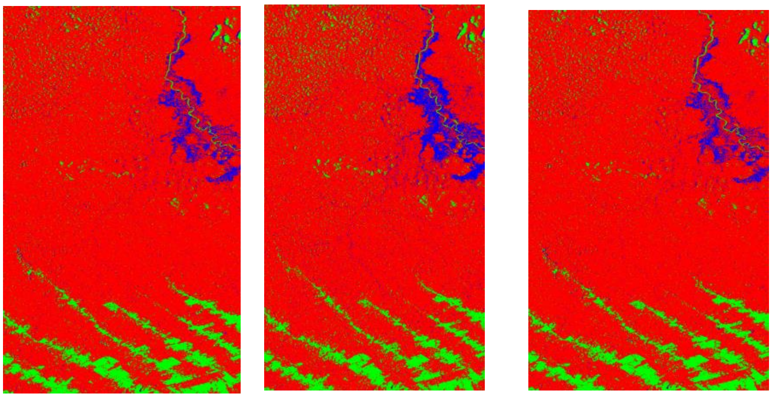

($\frac{\pi}{4}$) Elliptical ($\frac{\pi}{2}$)

Figure 5.13 SVM Classifier Comparission on CP modes

	Pi/4 mode			Elliptical mode			Pi/2 mode			CP
	F	DF	SV	F	DF	SV	F	DF	SV	
F	97.23	6.66	80.90	94.27	9.42	64.67	96.72	0.16	0.62	4419
DF	0.88	93.29	0.00	2.24	90.42	0.00	0.88	93.07	0.00	1757
SV	1.89	0.05	19.10	3.49	0.16	35.33	2.24	0.55	21.72	225
CE/OE	17.45/2.77	1.88/6.71	2.00/80.90	16.36/5.73	4.79/9.58	32.1/64.67	17.05/3.28	1.88/6.93	32.82/78.28	6401
PA/UA	97.23/82.55	93.29/98.12	19.10/68.00	94.27/83.64	90.42/95.21	35.33/67.87	96.72/82.95	93.07/98.12	21.72/67.18	
KC	0.73			0.72			0.73			
OA	86.31%			85.78%			86.28 %			

F: Forest; DF: Deforested ; SV: Short Vegetation; CP: Class Population; OA: Overall Accuracy; CE: Commission Error; OE: Omission Error; PA: Producer Accuracy; UA: User Accuracy; KC: Kappa Coefficient

Table 5.9 Comparison of CP Modes using SVM classifier

Chapter 6

Exploring the Capability of Compact Polarimetry (Hybrid-Pol) C-band RISAT-1 data over dual-pol and quad-pol for Land Cover Classification.

Contributions and citations of this chapter

Publication: 2

Citations:

6.1 Introduction

This chapter specifies the capability of compact polarimetry (Hybrid-pol) of RISAT-1 over dual-pol RISAT-1 and quad-pol Alos-PALSAR-2 data for land cover classification. The objective of this chapter is to compare the information content and penetration capability into the targets among the datasets.

6.1.1 Motivation: The motivation of this chapter came from the contributions of Raney et al., Thomas Aisworth et al., and Rajib Kumar et al.

6.1.2 Significance of Study area: The test site (San Francisco) used for this study is a Standard test site, approved by NASA, CSA, JAXA, and ESA. For a comparative analysis, the test site should be the same.

6.1.3 Significance of the datasets and frequency: RISAT-1 is the only mission to have Hybrid Polarimetric architecture on board. Alos Palsar-2 data is the only available L-band with quad-pol configuration. RISAT-1 and Alos palsar-2 data availability of Test site made to opt.

6.1.4 Novelty: In the literature, no one has attempted to compare RISAT-1, C-band, Hybrid-pol data with ALOS Palsar-2, L-band, quad-pol data. Moreover, the Hybrid-Pol recorded in the literature were simulated from quad-pol data.

6.1.5 Type of target: Urban

6.1.6 Application: Land Cover

6.1.7 Significance of frequency: L band and C-band has more penetration capability

Boularbah souissi et al. [96] used ESAR DLR polarimetric data in fully polarimetric mode and radarsat-2 in their study. From quad pol, CP mode was simulated. The authors have presented an initial comparison of polarimetric information content between QP and CP imaging modes. They have used an automated statistical clustering method based on Expectation Maximization. It was reported in case 1: that all modes almost have the same Overall Accuracy (95.47% for QP, 90.93% for C2, and 88.2% for CP). Case 2: all modes have different OA Accuracy (90.41% for QP, 64.53% for C2, and 75% for CP). It was reported that CP performance was very poor when compared to QP and C2.

Rajib Kumar et al. [21] used NASA/JPL AIRSAR L-band quad-pol data. From quad-pol data, hybrid-pol data was simulated by symmetrical assumptions $\left(S_{HV} = S_{HV}\right)$. From simulated hybrid-pol, Pseudo-quad-Pol was simulated. It was observed that Pseudo-quad-Pol values are matching with original quad-pol values. It was also found that the scattering mechanism for hybrid-pol data is less but comparable to quad-pol data.

Rajib Kumar et al. [16] used airborne multi-polarization GTRI data for comparing the information content of quad-pol with simulated hybrid-pol data. The authors concluded that the information contained in Hybrid-pol imagery is found to be comparable to that of quad-pol data.

T.L Anisworth et al. [19] used airborne AIRSAR L-band quad-pol data. Compact-Pol (pi/2) and CTLR modes are simulated from quad-pol data. Wishart maximum likelihood classifier was applied on all modes to compare the several class type accuracy. On the whole, quad-pol gave a good percentage of the training area and are correctly classified. It was found that CTLR and pi/2 mode almost gave similar results. The linear dual-pol yields the lowest results.

6.2 Why is hybrid-pol so special?

Hybrid-pol has the same feature as full-pol but has a half data rate. Full-pol has less than optimal ambiguity performance across the entire swath width because the pulse rate is too high. Therefore the full-pol is best suited for selected areas and applications, whereas the dual-pol mode has better uniform performance across the swath.

If a full-pol system is used all the time, it has some practical limitations on the performance. While operating in full-pol, we have to switch from H to V on the next pulse and receive both the polarization. In order to get the images in two polarizations and to get the images adequately sampled, we have to pulse the radar at twice the rate to get twice the data. As the missions are planned for global observation in ascending and descending pass over all land surface, water and ice surfaces, radars are imaging over a 50% of its orbiting time. If we continuously image using full-pol all the time we would have more data than we could get to the ground station. Hybrid-pol has many of the characterization of the full-pol not quite as rich but rich. In hybrid-pol we don’t have to pulse the radar at double rate. The other issues of full-pol are noise properties, called ambiguities that are little higher than one would like at the certain part of the swath. So several space agencies decided to operate mostly in dual-pol mode and to have optimal imaging performance. Therefore Hybrid-Pol data has the advantage of being a dual-pol in terms of swath width, power consumption, and almost the same as quad-pol in terms of information content.

6.3 Penetration Depth and Polarization

Like polarization back scatter toward the sensor results from single refraction from canopy component such as the leaves, stems, branches and trunk. These returns are generally very strong and are recorded as bright signals in like polarized radar imagery (HH or VV). This is often called canopy scattering. Conversely, if the energy is scattered multiple times with in a diffuse volume such as a stand of pine tree (i.e., from a needle to a stem, to the trunk, to a needle), the energy may become depolarized. This is often called volume scattering. A radar can measure the volume of depolarized volume scattering that takes place. E.g., it is possible to configure a radar to send a vertically polarized pulse of energy. Some of this energy becomes depolarized in canopy and exists towards the sensor in the horizontal domain. The depolarized energy may then be recorded by the sensor VH mode – vertical send and horizontal receive.

6.3.1 Penetration depth vs Frequency

Longer the microwave wavelength, the greater the penetration into the plant canopy. Surface scattering takes place at the top of the canopy as the energy entreats with the leaves\needle\stems. Volume scattering by the leaves, stems, branches and trunk takes place throughout the stand, and surface scattering can occur again at the soil surface [98]. A comparison of the repose of X-, C- and L-band microwave energy incident to the same canopy. The stronger wave length x band 3 cm energy is attenuated most by surface scattering at the top if the canopy by the foliage and small branches the c band 5.8 cm energy experiences surface scattering at the top of the canopy as well some volume scattering in the heart of the stand. Little energy reaches the ground. L-band 23.5 cm microwave energy penetrates farther into the canopy, where volume scattering among the leaves, stems, branches and trunk cause the beam to become depolarized [99]. Also, numerous pulses may be transmitted to the ground where surface scattering from the soil vegetation boundary layer may takes place longer p-band radar would afford the greater penetration thought he vegetation and mainly reflect of large stems and the soil surface.

6.4 Datasets used

The Datasets used in this study as shown in Table 6.1

SAR Mission	**RISAT-1**	**RISAT-1**	**Alos-palsar 2**
Frequency	C-Band (5.35 GHz)	C-Band (5.35 GHz)	L-Band (1.2 GHz)
Polarization	Dual -Pol	Hybrid-Pol	Quad-Pol
Country	India	India	Japan
Agency	ISRO	ISRO	JAXA
Incidence angle	26.35°	26.35°	8-70°
Swath	25 km	25 km	50 km
Resolution (m) (Azimuth, Range)	2.34, 3.3	2.34, 3.3	4.3 , 5.1
Altitude	530.789 km	530.789 km	639 km

Table 6.1 Datasets used in this study

6.5 Methodology

For RISAT_1 hybrid-pol data processing, Hybrid-Pol is imported to Polsarpro tool. The covariance matrix $\left(C_2\right)$ is generated and radiometric calibration is performed. The Stokes vector and stokes child parameters are generated. To remove speckle, speckle filtering was performed using refined lee filter 7*7 window size. Raney decomposition was performed on the filtered data resulting in six Raney derived parameters i.e. i) Raney odd bounce ii) Raney double bounce iii) Raney Random iv) Raney m v) Raney - delta, vi) Raney chi. M delta decomposition is performed using the Raney m parameter, Raney delta and Stokes first parameter. For land cover classification supervised classifier SVM with multi case approach was performed. Similarly, for Alos palsar-2 quad-pol data processing quad-pol data is imported to Polsarpro tool, and refined lee filter 7*7 window size is opted for speckle filtering. Yamaguchi four component decomposition is performed on the filtered image. For land cover classification supervised classifier SVM with multi case approach was performed. For RISAT-1 dual-pol data processing dual-pol data is to be imported to Polsarpro tool, and covariance matrix $\left(C_2\right)$ is generated. Refined lee filter 7*7 window size is opted for speckle filtering. Raney decomposition is performed and SVM with multi case approach was applied. Overall

Accuracy is performed for three SVM classified for comparing the information content, scattering response. The Flow chart of the proposed work is shown in. Fig 6.1.

6.5.1 Details of Test Site

The test site consists of two forest zones, three urban areas and one water body. In this work five classes are identified as targets viz. SOMA, Golden Gate Park, Water body, NOMA, Richmond. South of Market (SOMA) is an urban area occupied with tall buildings, Golden Gate Park a forest place full of vegetation and tall trees, Water body is a Sea, North of Market (NOMA) is an urban area occupied with large building with different orientation, and Richmond is a residential area with gardens in between and some medium buildings.

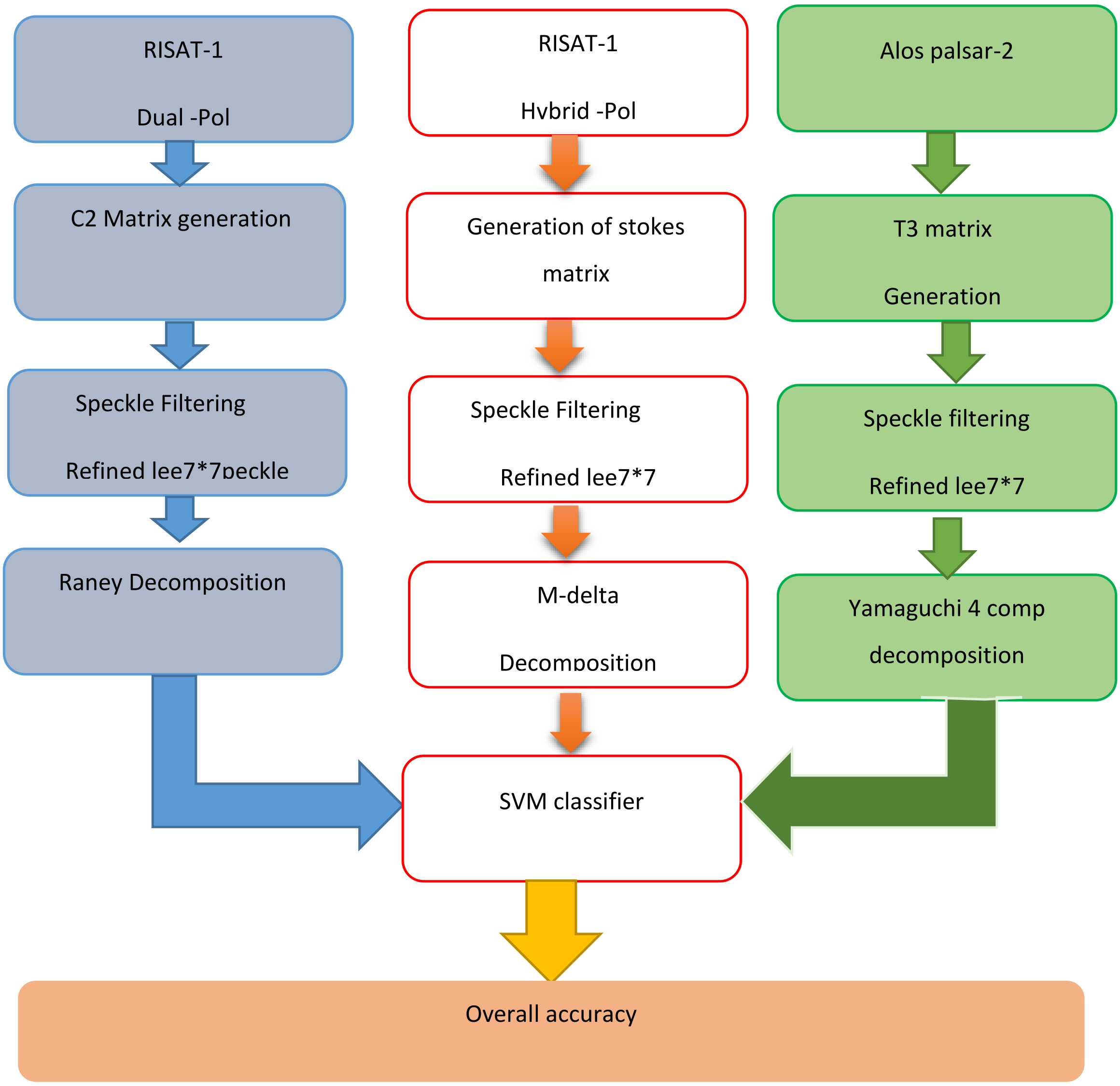

Fig 6.1 Flow chart of the work

6.6 Results and discussions

The quad-pol Alos palsar-2 data contains the full information when compared to Risat-1 hybrid-pol and dual-pol data. Alos palsar-2 quad-pol data has covariance matrix $\left(C_3\right)$ of 3*3, Hybrid-pol RISAT-1 data has a covariance matrix $\left(C_2\right)$ 2*2 with phase information, and dual-pol RISAT-1 has a covariance matrix $\left(C_2\right)$2*2 without phase information [100]. Figure 6.2 a) is the Yamaguchi four component decomposed image of Alos-palsar-2 quad-pol data, 6.2 b) is the m delta decomposed image of RISAT-1 hybrid-pol data, 6.2 c) is the Raney decomposed image of dual-pol RISAT-1 data. Fig 6 a) green color corresponds to vegetation class, red color corresponds to urban class and blue color corresponds to Water body (Sea), here SOMA an urban area was decomposed as a vegetation class due to multiple scattering. Fig 6 b) green color corresponds to vegetation class, red color corresponds to urban class and blue color corresponds to Water body (Sea), here SOMA is decomposed as a vegetation class due to multiple scattering but less compared to Yamaguchi four component decomposition. Fig 6 c) green color corresponds to vegetation class, red color corresponds to urban class and blue color corresponds to Water body, here water body is also decomposed as an urban class.

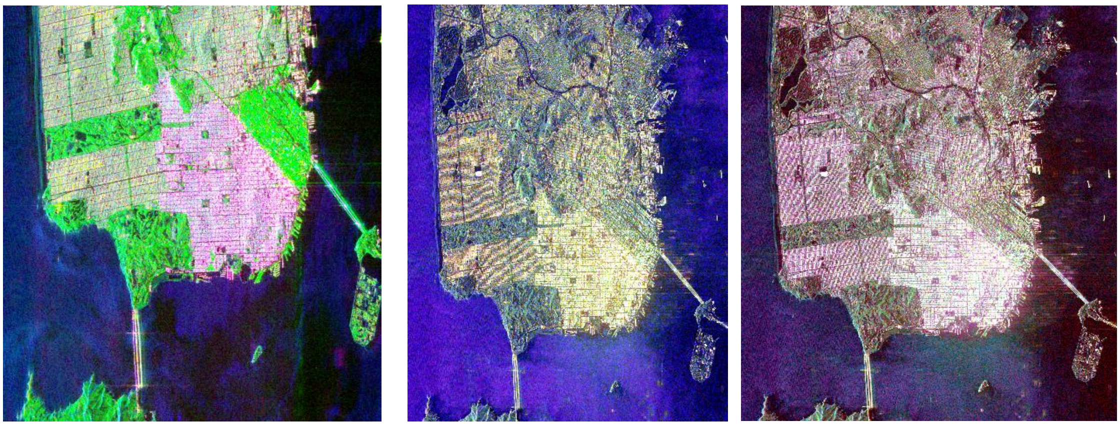

a) Yamaguchi quad-pol data b) M delta hybrid-pol data c) Raney Dual-pol data

Fig 6.2 Decomposition images on quad-pol, hybrid-pol and dual-pol data

Supervised classifier, SVM with multi class approach classified alos palsar quad-pol data very effectively with an Overall Accuracy of 85.80%. SVM classified Risat-1 hybrid-pol data with an Overall Accuracy of 69.79%. SVM classified Risat-1 dual-pol data with an Overall Accuracy of 49.98%. From Table 6.2, SOMA was classified very in quad-pol data very well when compared to hybrid-pol and dual-pol data. Golden Gate Park is similarly classified in quad-pol and hybrid-pol data. In dual-pol data Golden Gate Park is poorly classified. Water class is well classified in all data. NOMA is effectively classified in quad-pol data, less effectively classified in hybrid-pol data, and very poorly classified in dual-pol data. Richmond class is also classified effectively in in quad-pol data, less effectively classified in hybrid-pol data as shown in Fig 6.3. Dual-pol data is classified better than hybrid-pol data. From the results below hybrid-pol data is an intermediate between quad-pol and dual-pol data.

	Alos-palsar Quad-Pol					RISAT-1 Hybrid-Pol					RISAT-1 Dual-Pol				
	S	G	W	N	R	S	G	W	N	R	S	G	W	N	R
S	60.83	34.51	2.60	0.40	1.67	42.13	21.85	0.04	8.81	27.16	45.85	16.17	8.06	3.27	22.66
G	3.56	88.38	6.18	0.04	1.84	0.09	81.63	16.07	0	2.20	0.09	49.73	44.81	0	5.37
W	0	0	100	0	0	0	0.00	100	0	0	0	0.17	99.81	0	0.2
N	0.32	0.11	0	90.96	8.60	10.35	0.81	0.02	57.88	30.95	4.17	14.56	7.36	7.53	66.38
R	0.42	13.78	2.01	4.27	79.52	3.33	38.21	3.78	4.93	49.96	0.97	29.46	2.85	4.95	61.77
OA	85.80%					67.79%					49.98%				
S: SOMA, G: Golden Park, W: Water, N: NOMA, R: Richmond															

Table 6.2 Confusion matrix of three datasets

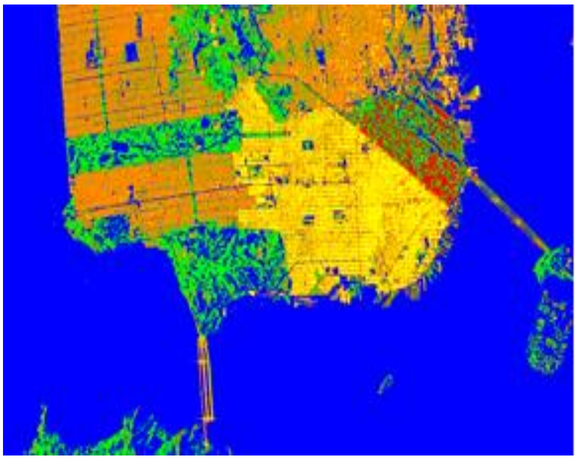

a) Alos quad-pol

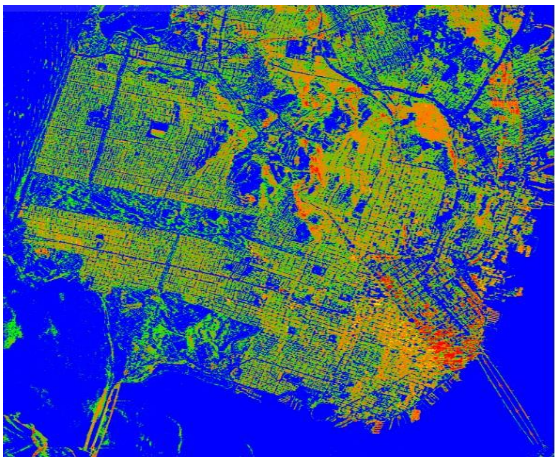

b) RISAT-1, Hybrid- pol

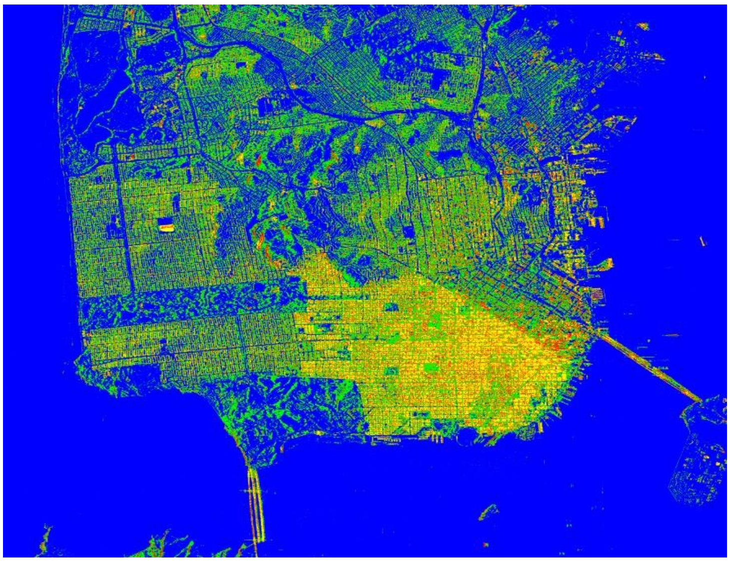

c) RISAT-1 Dual- pol

Fig 6.3 Supervised classified images on quad-pol, hybrid-pol and dual-pol data

6.7 Conclusions

In this chapter a comparative study on C-band dual-pol RISAT-1, Hybrid-pol, RISAT-1, L-band quad-pol Alos-PALSAR-2 with respect to information content and signal penetration is performed. The information content and penetration capability of L-band quad-pol Alos-PALSAR-2 recorded the highest overall accuracy 85.80% due to more signal penetration. The results of C-band Hybrid-pol, RISAT-1 were promising and the overall accuracy is recorded as 69.79%. The results of C-band dual-pol, RISAT-1 were very poor and was recorded with an overall accuracy 49.98%.

The difference between L-band quad-pol AlosPALSAR-2 and C-band Hybrid-pol, RISAT-1 OA was due to poor target decomposition in C-band hybrid-pol. Thus NOMA class and Richmond class were not classified accurately when compared to L-band quad-pol AlosPALSAR-2. We can conclude that hybrid-pol data will be an intermediate between quad-pol and dual-pol. Thus opting Hybrid-pol data using L-band can increase the overall classification accuracy. In future a comparison of L-band hybrid-pol data and L-band quad-pol data elaborate the capability of hybrid-pol data.

Chapter 7

Conclusions

7.1 Conclusions

In hybrid polarimetry, to characterize the return signal, Stokes parameters are sufficient. Hybrid-pol (compact polarimetry) SAR is a new SAR mode, with a combination of wider swath along with coherent dual polarization with relative phase information. Therefore, Hybrid-pol (compact polarimetry) SAR is always the best choice when transmitted power and swath width are the main constraints. From this work, we studied the importance of speckle filtering for image classification and the impact of speckle filter window size in speckle reduction in SAR images. This study also investigated the capability of m-delta, m-chi decomposition, Raney decomposition, and Pseudo Three-Component decomposition techniques for Land cover Classification. We have characterized and classified various ground target classes in the data very well. The m-chi decomposition approach has been proven to be robust even though the transmitting signal is not perfectly circular polarized. This study evaluated the potential of Compact polarimetric (Hybrid-pol) for meeting the Earth observation missions. Besides, this study has demonstrated the potential of Compact-pol for crop identification and crop classification. SVM classifier has classified the dataset very well, and the results are very satisfactory. In this study, we have obtained (OA) of 92.34% for Hybrid-pol RISAT-1 data using the SVM classifier with RBF kernel. Similarly, SVM with RBF kernel parameter gave an Overall Accuracy (OA) of 76.83% for dual-pol RISAT-1 data. The results obtained from a comparative study of dual-pol vs Hybrid-pol RISAT-1 data for crop discrimination are very promising. The OA of Hybrid-pol data was 83.03% and for dual-pol, data was 54.75%. Thus from this study, we can conclude that Hybrid-pol data is always preferred over Dual-pol data concerning information content. Compact polarimetric SAR contains more polarimetric information than conventional linear dual-pol SAR. Compact polarimetric SAR (Hybrid-pol) achieves comparable polarimetric information to quad-pol SAR. To compare the penetration capability, Alos palsar-2 (L-band) data and RISAT-1 (C-band) data have opted on the standard test site San Francisco city. From this study, using a standard test site, Hybrid-pol RISAT-1 data, and Quad -pol Alos-Palsar-2 data are compared for information content and it was found that Hybrid -pol data is far more superior than linear dual-pol data and comparable to quad-pol data in terms of information content and penetration capability. The overall accuracy for L-band quad-pol AlosPALSAR-2 is 85.80%, C-band Hybrid-pol, RISAT-1 data is 69.79%, C-band dual-pol, and RISAT-1 data is 49.98%.

7.2 Future scope

The SAR remote sensing using compact pol data is been an active field of research with wide applications, many space agencies ISRO, CSA, NASA/JPL, JAXA, ESA are planning with compact-pol architecture such as RISAT-1B, RCM constellation. The possibility of hybrid polarimetry in exploring the Lunar (moon) surface and for planetary studies will be investigated.

In future, a comparison of L-band hybrid-pol data and L-band quad-pol data elaborates the capability of hybrid-pol data over quad-pol data for agriculture application, oil spill detection, and sea ice characterization.

References

[1] https://history.nasa.gov/sputnik.html

[2] https://www.nasa.gov/mission_pages/explorer/explorer-overview.html

[3] http://www.isro.gov.in/Spacecraft/bhaskara-i

[4] http://www.isro.gov.in/list-of-spacecrafts https://www.nrsc.gov.in/Remote_Sensing_Data_Policy?q=Earth_Observation_Missions

[5] http://www.isro.gov.in/sites/default/files/AnnualRepo-rts/2014/EOS.html\

[6] George Joseph.: Fundamentals of Remote Sensing, Universities Press, (2003).

[7] Lillisand, Kiefer, and Chipman. : Remote Sensing and Image Interpretation, John Wiley & Sons, (2012).

[8] Iain H. Woodhouse.: Introduction to Microwave Remote Sensing. CRC Press, (2006).

[9] Jong-Sen Lee, Eric Poitter.: Polarimetric Radar Imaging from basics to applications, CRC Press, (2009).

[10] Wiley, C.A. Synthetic aperture radars—A paradigm for technology evolution. IEEE Trans. Aerosp. Electron. Syst 1985, 21, 440–443.

[11] Moreira, A., Prats-Iraola, P., Younis, M., Krieger, G., Hajnsek, I. and Papathanassiou, K.P., 2013. A tutorial on synthetic aperture radar. IEEE Geoscience and remote sensing magazine, 1(1), pp.6-43

[12] J. A. Richards,: Remote sensing with imaging radar. Berlin, Germany: Springer, (2009).

[13] R. K. Raney, "Hybrid-polarity SAR architecture," IEEE Trans on Geoscience and Remote Sensing, vol. 45, pp. 3397-3404, 2007

[14] R. Touzi compact-hybrid versus linear- dual and fully polarimetric SAR, Proc. of PolInSAR2009, 2009

[15] Chakraborty, Manab & Panigrahy, S & Rajawat, A.S. & Kumar, Raj & Murthy, Tvr & Haldar, Dipanwita & Chakraborty, Abhisek & Kumar, Tanumi & Rode, Sneha & Kumar, Hrishikesh & Mahapatra, Manik & Kundu, Sanchayita. (2013). Initial results using RISAT-1 C-band SAR data. Current Science. 104. 490-501

[16] R. K. Panigrahi and A. K. Mishra, "Comparison of hybrid-polarization with Quad-polarization schemes based on airborne SAR images," 2010 Indian Antenna Week: A Workshop on Advanced Antenna Technology, Puri, 2010, pp. 1-4, doi: 10.1109/AAT.2010.55459532012

[17] J-C Souyris, P.I.R. Fjortoft, S. Mingot and J-S Lee, Compact polarimetry based on symmetric properties of geophysical media: the π/4 mode, IEEE Transactions on Geoscience and Remote Sensing, vol. 43, no. 3, March 2005, pp. 634-645

[18] Michael E. Nord, Thomas L. Ainsworth, Jong-Sen Lee, Nick J. S. Stacy, Comparison of Compact Polarimetric Synthetic Aperture Radar Modes, IEEE Transactions On Geoscience and Remote Sensing, vol. 47, no. 1, January 2009.

[19] Ainsworth, T.L., Kelly, J.P. and Lee, J.S., 2009. Classification comparisons between dual-pol, compact polarimetric and quad-pol SAR imagery. ISPRS Journal of Photogrammetry and Remote Sensing, 64(5), pp.464-471.

[20] Charbonneau, F.J., Brisco, B., Raney, R.K., McNairn, H., Liu, C., Vachon, P.W., Shang, J., DeAbreu, R., Champagne, C., Merzouki, A. and Geldsetzer, T., 2010. Compact polarimetry overview and applications assessment. *Canadian Journal of Remote Sensing*, *36*(sup2), pp.S298-S315

[21] Rajib Kumar Panigrahi, Amit Kumar Mishra, Comparison of hybrid-Pol with a quad-Pol scheme based on polarimetric information content, *International Journal of Remote Sensing*, Vol. 33, No. 11, 10 June 2012, 3531–3541

[22] Haldar, D., Das, A., Mohan, S., Pal, O., Hooda, R.S. and Chakraborty, M., 2012. Assessment of L-band SAR data at different polarization combinations for crop and other landuse classification. *Progress In Electromagnetics Research*, *36*, pp.303-321

[23] Lardeux, C., Frison, P.L., Tison, C., Souyris, J.C., Stoll, B., Fruneau, B. and Rudant, J.P., 2009. Support vector machine for multifrequency SAR polarimetric data classification. IEEE Transactions on Geoscience and Remote Sensing, 47(12), pp.4143-4152.

[24] Yekkehkhany, B., A. Safari, S. Homayouni, and M. Hasanlou. "A comparison study of different kernel functions for SVM-based classification of multi-temporal polarimetry SAR data." The International Archives of Photogrammetry, Remote Sensing and Spatial Information Sciences 40, no. 2 (2014): 281

[25] J. W. Goodman. : Some fundamental properties of speckle, Journal of Optical Society, 66 (11) (1976), 1145-1150.

[26] Jong Sen Lee.: A Simple Speckle Smoothing Algorithm for Synthetic Aperture Radar Images, IEEE Journals & Magazines, 13(1) (1983), 85-89.

[27] Fang Qiu, Judith Berglund, R. John Jensen, Pathik Thakkar, and Dianwei Ren.: Speckle Noise Reduction in SAR Imagery Using a Local Adaptive Median Filter. GIScience and Remote Sensing, 41 (2004), 244-266

[28] Argenti, F., Lapini, A., Bianchi, T. and Alparone, L., 2013. A tutorial on speckle reduction in synthetic aperture radar images. *IEEE Geoscience and remote sensing magazine*, *1*(3), pp.6-35.

[29] Qiu, F., Berglund, J., Jensen, J.R., Thakkar, P. and Ren, D., 2004. Speckle noise reduction in SAR imagery using a local adaptive median filter. *GIScience & Remote Sensing*, *41*(3), pp.244-266.

[30] Lee, J.S., 1986. Speckle suppression and analysis for synthetic aperture radar images. *Optical engineering*, *25*(5), p.255636..

[31] Lee, J.S., Wen, J.H., Ainsworth, T.L., Chen, K.S. and Chen, A.J., 2008. Improved sigma filter for speckle filtering of SAR imagery. *IEEE Transactions on Geoscience and Remote Sensing*, *47*(1), pp.202-213.

[32] Lee, J.S., Jurkevich, L., Dewaele, P., Wambacq, P. and Oosterlinck, A., 1994. Speckle filtering of synthetic aperture radar images: A review. *Remote sensing reviews*, *8*(4), pp.313-340..

[33] Lee, J.S., Grunes, M.R. and De Grandi, G., 1999. Polarimetric SAR speckle filtering and its implication for classification. *IEEE Transactions on Geoscience and remote sensing*, *37*(5), pp.2363-2373.

[34] Touzi, R., 2002. A review of speckle filtering in the context of estimation theory. *IEEE Transactions on Geoscience and Remote Sensing*, *40*(11), pp.2392-2404.

[35] Lee, J.S., Grunes, M.R., Schuler, D.L., Pottier, E. and Ferro-Famil, L., 2005. Scattering-model-based speckle filtering of polarimetric SAR data. *IEEE Transactions on Geoscience and Remote Sensing*, *44*(1), pp.176-187.

[36] Foucher, S. and López-Martínez, C., 2014. Analysis, evaluation, and comparison of polarimetric SAR speckle filtering techniques. *IEEE transactions on image processing*, *23*(4), pp.1751-1764.

[37] Lee, J.S., Ainsworth, T.L., Wang, Y. and Chen, K.S., 2014. Polarimetric SAR speckle filtering and the extended sigma filter. *IEEE Transactions on geoscience and remote sensing*, *53*(3), pp.1150-1160.

[38] Touzi, R. and Lopes, A., 1994. The principle of speckle filtering in polarimetric SAR imagery. *IEEE Transactions on Geoscience and Remote Sensing*, *32*(5), pp.1110-1114.

[39] Cloude, S.R. and Pottier, E., 1996. A review of target decomposition theorems in radar polarimetry. *IEEE transactions on geoscience and remote sensing*, *34*(2), pp.498-518.

[40] Cloude, S.R., 1985. Target decomposition theorems in radar scattering. *Electronics Letters*, *21*(1), pp.22-24.

[41] Cloude, S.R., 1992. Uniqueness of target decomposition theorems in radar polarimetry. In *Direct and inverse methods in radar polarimetry* (pp. 267-296). Springer, Dordrecht.

[42] Krogager, E., 1990. New decomposition of the radar target scattering matrix. *Electronics Letters*, *26*(18), pp.1525-1527.

[43] Touzi, R., 2006. Target scattering decomposition in terms of roll-invariant target parameters. *IEEE Transactions on geoscience and remote sensing*, *45*(1), pp.73-84.

[44] Turkar, V. and Rao, Y.S., 2011. Applying coherent and incoherent target decomposition techniques to polarimetric SAR data. In *Proceedings on the IJCA International Conference on Technology Systems and Management* (pp. 23-29).

[45] Du, L.J. and Lee, J.S., 1996, May. Polarimetric SAR image classification based on target decomposition theorem and complex Wishart distribution. In *IGARSS'96. 1996 International Geoscience and Remote Sensing Symposium* (Vol. 1, pp. 439-441). IEEE.

[46] Yamaguchi, Y., Moriyama, T., Ishido, M. and Yamada, H., 2005. Four-component scattering model for polarimetric SAR image decomposition. *IEEE Transactions on Geoscience and Remote Sensing*, *43*(8), pp.1699-1706.

[47] Yamaguchi, Y., Sato, A., Boerner, W.M., Sato, R. and Yamada, H., 2011. Four-component scattering power decomposition with rotation of coherency matrix. *IEEE Transactions on Geoscience and Remote Sensing*, *49*(6), pp.2251-2258.

[48] Kumar, A., Das, A. and Panigrahi, R.K., 2019. Hybrid-pol decomposition methods: A comparative evaluation and a new entropy-based approach. *IETE Technical Review*, pp.1-13.

[49] Kumar, A., Panigrahi, R.K. and Das, A., 2016. Three-component decomposition technique for hybrid-pol SAR data. *IET Radar, Sonar & Navigation*, *10*(9), pp.1569-1574.

[50] Guo, S., Li, Y., Hong, W., Wang, J. and Guo, X., 2016. Model-based target decomposition with the π/4 mode compact polarimetry data. *Science China Information Sciences*, *59*(6), p.062307.

[51] Raney, R.K., Cahill, J.T., Patterson, G.W. and Bussey, D.B.J., 2012. The m-chi decomposition of hybrid dual-polarimetric radar data with application to lunar craters. *Journal of Geophysical Research: Planets*, *117*(E12).

[52] Raney, R.K., 2007, January. Decomposition of hybrid-polarity SAR data. In *PolIn-SAR 2007: Proceedings of the 3rd International Workshop on Science and Applications* (pp. 22-26).

[53] Raney, R.K., 2007, July. Comments on hybrid-polarity SAR architecture. In *2007 IEEE International Geoscience and Remote Sensing Symposium* (pp. 2229-2231). IEEE.

[54] Kumar, A., Das, A. and Panigrahi, R.K., 2019. Hybrid-pol decomposition methods: A comparative evaluation and a new entropy-based approach. *IETE Technical Review*, pp.1-13.

[55] Uppala, D., Kothapalli, R.V., Poloju, S., Mullapudi, S.S.V.R. and Dadhwal, V.K., 2015. Rice crop discrimination using single date RISAT1 hybrid (RH, RV) polarimetric data. *Photogrammetric Engineering & Remote Sensing*, *81*(7), pp.557-563.

[56] Uppala, D., Venkata, R.K., Poloju, S., Venkata Rama, S.M. and Dadhwal, V.K., 2016. Discrimination of maize crop with hybrid polarimetric RISAT1 data. *International Journal of Remote Sensing*, *37*(11), pp.2641-2652.

[57] Chen, C.T., Chen, K.S. and Lee, J.S., 2003. The use of fully polarimetric information for the fuzzy neural classification of SAR images. *IEEE Transactions on Geoscience and Remote Sensing*, *41*(9), pp.2089-2100.

[58] Uhlmann, S. and Kiranyaz, S., 2014. Classification of dual-and single polarized SAR images by incorporating visual features. *ISPRS journal of photogrammetry and remote sensing*, *90*, pp.10-22.

[59] Mishra, P., Singh, D. and Yamaguchi, Y., 2011. Land cover classification of PALSAR images by knowledge based decision tree classifier and supervised classifiers based on SAR observables. *Progress In Electromagnetics Research*, *30*, pp.47-70.

[60] Hara, Y., Atkins, R.G., Yueh, S.H., Shin, R.T. and Kong, J.A., 1994. Application of neural networks to radar image classification. *IEEE Transactions on Geoscience and Remote Sensing*, *32*(1), pp.100-109.

[61] Shah Hosseini, R., Entezari, I., Homayouni, S., Motagh, M. and Mansouri, B., 2011. Classification of polarimetric SAR images using Support Vector Machines. *Canadian Journal of Remote Sensing*, *37*(2), pp.220-233.

[62] Lee, J.S. and Jurkevich, I., 1989. Segmentation of SAR images. *IEEE transactions on Geoscience and Remote Sensing*, *27*(6), pp.674-680.

[63] Turkar, V., Deo, R., Rao, Y.S., Mohan, S. and Das, A., 2012. Classification accuracy of multi-frequency and multi-polarization SAR images for various land covers. *IEEE Journal of Selected Topics in Applied Earth Observations and Remote Sensing*, *5*(3), pp.936-941.

[64] Fukuda, S. and Hirosawa, H., 2001, July. Support vector machine classification of land cover: Application to polarimetric SAR data. In *IGARSS 2001. Scanning the Present and Resolving the Future. Proceedings. IEEE 2001 International Geoscience and Remote Sensing Symposium (Cat. No. 01CH37217)* (Vol. 1, pp. 187-189). IEEE.

[65] Frost, V.S. and Yurovsky, L.S., 1985. Maximum likelihood classification of synthetic aperture radar imagery. *Computer vision, graphics, and image processing*, *32*(3), pp.291-313.

[66] Nyoungui, A.N., Tonye, E. and Akono, A., 2002. Evaluation of speckle filtering and texture analysis methods for land cover classification from SAR images. *International Journal of Remote Sensing*, *23*(9), pp.1895-1925.

[67] Hu, H. and Ban, Y., 2008. Urban land-cover mapping and change detection with radarsat sar data using neural network and rule-based classifiers. In *XXI Congress of International Society for Photogrammetry and Remote Sensing (ISPRA). july, 2008. Beijing, China* (pp. 1549-1553).

[68] Ohki, M. and Shimada, M., 2018. Large-area land use and land cover classification with quad, compact, and dual polarization SAR data by PALSAR-2. *IEEE Transactions on Geoscience and Remote Sensing*, *56*(9), pp.5550-5557.

[69] Haldar, D., Das, A., Mohan, S., Pal, O., Hooda, R.S. and Chakraborty, M., 2012. Assessment of L-band SAR data at different polarization combinations for crop and other landuse classification. *Progress In Electromagnetics Research*, *36*, pp.303-321.

[70] Mohan, S., Das, A., Haldar, D. and Maity, S., 2011, September. Monitoring and retrieval of vegetation parameter using multi-frequency polarimetric SAR data. In *2011 3rd International Asia-Pacific Conference on Synthetic Aperture Radar (APSAR)* (pp. 1-4). IEEE.

[71] Raney, R.K., 2006. Dual-polarized SAR and stokes parameters. *IEEE Geoscience and Remote Sensing Letters*, *3*(3), pp.317-319.

[72] S. R. Cloude, D. G. Goodenough, and H. Chen, "Compact Decomposition Theory," IEEE Geoscience and Remote Sensing Letters, vol. 9, pp. 28-32, 2012.

[73] Raney, R.K., Cahill, J.T., Patterson, G.W. and Bussey, D.B.J., 2012. The m-chi decomposition of hybrid dual-polarimetric radar data with application to lunar craters. *Journal of Geophysical Research: Planets*, *117*(E12).

[74] Dubois-Fernandez, P.C., Souyris, J.C., Angelliaume, S. and Garestier, F., 2008. The compact polarimetry alternative for spaceborne SAR at low frequency. *IEEE Transactions on Geoscience and Remote Sensing*, *46*(10), pp.3208-3222.

[75] Atteia, G.E. and Collins, M.J., 2013. On the use of compact polarimetry SAR for ship detection. *ISPRS Journal of Photogrammetry and Remote Sensing*, *80*, pp.1-9.

[76] Souissi, B., Ouarzeddine, M. and Belhadj-Aissa, A., 2014. Optimal SVM classification for compact polarimetric data using Stokes parameters. *Journal of Mathematical Modelling and Algorithms in Operations Research*, *13*(4), pp.433-446.

[77] Srikanth, P., Ramana, K.V., Deepika, U., Chakravarthi, P.K. and Sai, M.S., 2016. Comparison of various polarimetric decomposition techniques for crop classification. *Journal of the Indian Society of Remote Sensing*, *44*(4), pp.635-642.

[78] Goswami, J.N. and Annadurai, M., 2009. Chandrayaan-1: India's first planetary science mission to the moon. *Current science*, pp.486-491.

[79] Raney, R.K., Spudis, P.D., Bussey, B., Crusan, J., Jensen, J.R., Marinelli, W., McKerracher, P., Neish, C., Palsetia, M., Schulze, R. and Sequeira, H.B., 2010. The lunar mini-RF radars: Hybrid polarimetric architecture and initial results. *Proceedings of the IEEE*, *99*(5), pp.808-823.

[80] Drucker, H., Wu, D. and Vapnik, V.N., 1999. Support vector machines for spam categorization. *IEEE Transactions on Neural networks*, *10*(5), pp.1048-1054.

[81] Trisasongko, B.H., Panuju, D.R., Paull, D.J., Jia, X. and Griffin, A.L., 2017. Comparing six pixel-wise classifiers for tropical rural land cover mapping using four forms of fully polarimetric SAR data. *International Journal of Remote Sensing*, *38*(11), pp.3274-3293.

[82] Yekkehkhany, B., Safari, A., Homayouni, S. and Hasanlou, M., 2014. A comparison study of different kernel functions for SVM-based classification of multi-temporal polarimetry SAR data. *The International Archives of Photogrammetry, Remote Sensing and Spatial Information Sciences*, *40*(2), p.281.

[83] Jayasri, P.V., Niharika, K., Joseph, M., Ryali, H.U.S., Sarma, C.R., Kumari, E.S. and Prasad, A.V.V., 2018. Implementation of RISAT-1 hybrid polarimetric decomposition techniques and analysis using corner reflector data. *Journal of the Indian Society of Remote Sensing*, *46*(6), pp.1005-1012.

[84] Joseph, M., Jayasri, P.V., Dutta, S., Kumari, E.S. and Prasad, A.V.V., 2016, December. Oil spill detection from RISAT-1 imagery using texture analysis. In *2016 Asia-Pacific Microwave Conference (APMC)* (pp. 1-4). IEEE.

[85] Jayasri, P.V., Reddy, C.S., Joseph, M., Sundari, H.U., Kumari, E.S. and Prasad, A.V.V., 2016, December. A case study on utilization of RISAT-1 SAR data for forest burnt area

detection in India. In *2016 Asia-Pacific Microwave Conference (APMC)* (pp. 1-3). IEEE.

[86] Jayasri, P.V., Niharika, K., Yedukondalu, K., Kumari, E.S. and Prasad, A.V.V., 2018. Radar Cross Section Characterization of Corner Reflectors in Different Frequency Bands and Polarizations. *International Archives of the Photogrammetry, Remote Sensing and Spatial Information Sciences*, *42*, p.5.

[87] Chauhan, S., Srivastava, H.S. and Patel, P., 2018. Wheat crop biophysical parameters retrieval using hybrid-polarized RISAT-1 SAR data. *Remote sensing of environment*, *216*, pp.28-43.

[88] Ponnurangam, G.G., Jagdhuber, T., Hajnsek, I. and Rao, Y.S., 2015. Soil moisture estimation using hybrid polarimetric SAR data of RISAT-1. *IEEE Transactions on Geoscience and Remote Sensing*, *54*(4), pp.2033-2049.

[89] Sivasankar, T., Srivastava, H.S., Sharma, P.K., Kumar, D. and Patel, P., 2015. Study of hybrid polarimetric parameters generated from RISAT-1 SAR data for various land cover targets. *Int. J. Adv. Remote Sens. GIS Grogr*, *3*, pp.32-42.

[90] Padalia, H. and Yadav, S., 2017. Evaluation of RISAT-1 SAR data for tropical forestry applications. *Advances in Space Research*, *59*(1), pp.2-11.

[91] Kumar, H. and Rajawat, A.S., 2017. Potential of RISAT-1 SAR data in detecting palaeochannels in parts of the Thar Desert, India. *Curr. Sci*, *113*(10), pp.1899-1905.

[92] Mishra, V.N., Kumar, P., Gupta, D.K. and Prasad, R., 2014, December. Classification of various land features using RISAT-1 dual polarimetric data. International Society for Photogrammetry and Remote Sensing.

[93] Rao, Y.S., Meadows, P. and Kumar, V., 2016, July. Evaluation of RISAT-1 compact polarization data for calibration. In *2016 IEEE international geoscience and remote sensing symposium (IGARSS)* (pp. 3250-3253). IEEE.

[94] Singha, S. and Ressel, R., 2017. Arctic sea ice characterization using RISAT-1 compact-pol SAR imagery and feature evaluation: A case study over Northeast Greenland. *IEEE Journal of Selected Topics in Applied Earth Observations and Remote Sensing*, *10*(8), pp.3504-3514.

[95] Kumar, P., Prasad, R., Mishra, V.N., Gupta, D.K. and Singh, S.K., 2016. Artificial neural network for crop classification using C-band RISAT-1 satellite datasets. *Russian agricultural sciences*, *42*(3-4), pp.281-284.

[96] Boularbah, S., Ouarzeddine, M. and Belhadj-Aissa, A., 2012. Investigation of the capability of the compact polarimetry mode to reconstruct full polarimetry mode using RADARSAT2 data. *Advanced Electromagnetics*, *1*(1), pp.19-28.

[97] El Hajj, M., Baghdadi, N., Bazzi, H. and Zribi, M., 2019. Penetration analysis of SAR signals in the C and L bands for wheat, maize, and grasslands. *Remote Sensing*, *11*(1), p.31.

[98] Lee, J.S., Grunes, M.R. and Pottier, E., 2001. Quantitative comparison of classification capability: Fully polarimetric versus dual and single-polarization SAR. *IEEE Transactions on Geoscience and Remote Sensing*, *39*(11), pp.2343-2351.

[99] Abdikan, S. and Sanli, F.B., 2012. Comparison of different fusion algorithms in urban and agricultural areas using SAR (PALSAR and RADARSAT) and optical (SPOT) images. *Boletim de Ciências Geodésicas*, *18*(4), pp.509-531.

[100] Pandey, Gaurav & Singh, Hari & Bharti, Pradutt & Pandey, Amritanshu & Meshram, Manoj. (2014). High Gain Vivaldi Antenna for Radar and Microwave Imaging Applications. International Journal of Signal Processing Systems. 3. 10.12720/ijsps.3.1.35-39.

[101] Vishwakarma, Rajesh & Ansari, J & Meshram, Manoj. (2006). Equilateral triangular microstrip antenna for circular polarization dual-band operation. Indian J Radio Space Phys. 35.1. Pandey, Gaurav & Singh, Hari & Bharti, Pradutt & Pandey, Amritanshu & Meshram, Manoj. (2014). High Gain Vivaldi Antenna for Radar and Microwave Imaging Applications. International Journal of Signal Processing Systems. 3. 10.12720/ijsps.3.1.35-39.

[102] Collins, M.J., Denbina, M. and Atteia, G., 2012. On the reconstruction of quad-pol SAR data from compact polarimetry data for ocean target detection. *IEEE Transactions on Geoscience and Remote Sensing*, *51*(1), pp.591-600.

[103] https://www.l3harrisgeospatial.com/Software-Technology/ENVI

[104] https://step.esa.int/main/toolboxes/polsarpro-v6-0-biomass-edition-toolbox/

[105] https://step.esa.int/main/toolboxes/snap/

Citations (23)

1. Raney, R.K., 2019. Hybrid dual-polarization synthetic aperture radar. Remote Sensing, 11(13), p.1521.
2. Brisco, B., Mahdianpari, M. and Mohammadimanesh, F., 2020. Hybrid Compact Polarimetric SAR for Environmental Monitoring with the RADARSAT Constellation Mission. *Remote Sensing*, *12*(20), p.3283.
3. Tomar, K.S., Kumar, S. and Tolpekin, V.A., 2019. Evaluation of Hybrid Polarimetric Decomposition Techniques for Forest Biomass Estimation. IEEE Journal of Selected Topics in Applied Earth Observations and Remote Sensing, 12(10), pp.3712-3718.
4. Robertson, L.D., Davidson, A., McNairn, H., Hosseini, M. and Mitchell, S., 2019, July. Compact Polarimetry for Agricultural Mapping and Inventory: Preparation for Radarsat Constellation Mission. In IGARSS 2019-2019 IEEE International Geoscience and Remote Sensing Symposium (pp. 5851-5854). IEEE.
5. Verma, N., Mishra, P. and Purohit, N., 2020. Development of a knowledge based decision tree classifier using hybrid polarimetric SAR observables. International Journal of Remote Sensing, 41(4), pp.1302-1320.
6. Srisumantyo, J.T., Chua, M.Y., Santosa, C.E., fried Panggabean, G., Tomoro, W., Bambang, S., Sumantyo, F.D.S., Kengo, T., Sasmita, K., Mardianto, A. and Supartono, E., 2020. Airborne Circularly Polarized Synthetic Aperture Radar. *IEEE Journal of Selected Topics in Applied Earth Observations and Remote Sensing*.
7. KUMAR, A., 2019. *ANALYSES OF HYBRID-POLSAR DATA FOR LANDCOVER CLASSIFICATION* (Doctoral dissertation, INDIAN INSTITUTE OF TECHNOLOGY ROORKEE).
8. Cui, H.S., 2019, October. Sub-urban land classification using GF-2 images and support vector machine method. In IOP Conference Series: Earth and Environmental Science (Vol. 351, No. 1, p. 012028). IOP Publishing.
9. Kumari, H. and Bhardwaj, A., 2020. Analysis of Polarimetric Mini-SAR and Mini-RF Datasets for Surface Characterization and Crater Delineation on Moon.
10. Jin, Z., Azzari, G., You, C., Di Tommaso, S., Aston, S., Burke, M. and Lobell, D.B., 2019. Smallholder maize area and yield mapping at national scales with Google Earth Engine. Remote Sensing of Environment, 228, pp.115-128.

11. Azzari, G., Grassini, P., Edreira, J.I.R., Conley, S., Mourtzinis, S. and Lobell, D.B., 2019. Satellite mapping of tillage practices in the North Central US region from 2005 to 2016. Remote Sensing of Environment, 221, pp.417-429.
12. Danilla, C., Persello, C., Tolpekin, V. and Bergado, J.R., 2017, July. Classification of multitemporal SAR images using convolutional neural networks and Markov random fields. In 2017 IEEE International Geoscience and Remote Sensing Symposium (IGARSS) (pp. 2231-2234). IEEE.
13. Wang, S., Di Tommaso, S., Faulkner, J., Friedel, T., Kennepohl, A., Strey, R. and Lobell, D.B., 2020. Mapping crop types in southeast india with smartphone crowdsourcing and deep learning. *Remote Sensing*, *12*(18), p.2957.
14. Danilla, C.A.R.O.L.Y.N.E., 2017. Convolutional neural networks for contextual denoising and classification of SAR images.
15. Dasari, K. and Anjaneyulu, L., 2017. Importance of Speckle filter window Size and its impact on Speckle reduction in SAR images. International Journal of Advances in Microwave Technology, 2, pp.98-102.
16. Bangira, T., 2019. Mapping surface water in complex and heterogeneous environments using remote sensing (Doctoral dissertation, Stellenbosch: Stellenbosch University).
17. Kamath, P.R., Senapati, K. and Jidesh, P., 2020. Despeckling of Sar Images Using Shrinkage of Two-Dimensional Discrete Orthonormal S-Transform. *International Journal of Image and Graphics*, p.2150023.
18. PAPILA, İ., SERTEL, E., KAYA, Ş. and GAZIOĞLU, C., 2018. OIL SPILL DETECTION USING REMOTE SENSING TECHNOLOGIES-SYNTHETIC APERTURE RADAR (SAR). Oil Spill along the Turkish Straits, p.140.
19. Sharma, A.K., Hubert-Moy, L., Sriramulu, B., Sekhar, M., Ruiz, L., Bandyopadhyay, S., Mohan, S. and Corgne, S., 2019. Evaluation of Radarsat-2 quad-pol SAR time-series images for monitoring groundwater irrigation. International Journal of Digital Earth, 12(10), pp.1177-1197.
20. MORA, B.S.V., SEGUIMIENTO A LA INUNDACIÓN OCURRIDA DURANTE LA OLA INVERNAL EN EL AÑO 2010 SOBRE LAS COBERTURAS VEGETALES IDENTIFICABLES EN EL MUNICIPIO DE SANTA CRUZ DE MOMPÓS UTILIZANDO IMÁGENES DEL SENSOR PALSAR DEL SATÉLITE ALOS.
21. Valencia, B. and Upegui, E., 2020. Propuesta metodológica para generar mapas de cobertura de la tierra a partir de imágenes de radar ALOS/PALSAR: Estudio de caso

Mompós, Colombia. Revista Ibérica de Sistemas e Tecnologias de Informação, (E28), pp.56-68.

22. Valencia Mora, B.S., Seguimiento a la inundación ocurrida durante la ola invernal en el año 2010 sobre las coberturas vegetales identificables en el Municipio de Santa Cruz de Mompós utilizando imágenes del sensor PALSAR del satélite ALOS.
23. Acar, H., Özerdem, M.S. and Acar, E., 2020. Soil Moisture Inversion Via Semiempirical and Machine Learning Methods With Full-Polarization Radarsat-2 and Polarimetric Target Decomposition Data: A Comparative Study. *IEEE Access*, *8*, pp.197896-197907.

List of publications

List of Journals

i. Dasari, K. and Lokam, A., 2018. Exploring the capability of compact polarimetry (Hybrid Pol) C band RISAT-1 data for land cover classification. *IEEE Access*, *6*, pp.57981-57993.

ii. Dasari, K. and Anjaneyulu, L., 2017. Importance of Speckle filter window Size and its impact on Speckle reduction in SAR images. *International Journal of Advances in Microwave Technology*, *2*, pp.98-102.

iii. Kiran, D. and Anjaneyulu, L., 2016. Eigen Value and Eigen Vector Based Decomposition and Wishart Supervised Classification on Fully Polarimetric SAR Data. *Indian Journal of Science and Technology*, *9*(S1), pp.1-6.

iv. Dasari, K., Lokam, A. and Jayasri, P.V., 2016. A Study on Utilization of Polarimetric SAR Data in Planning a Smart City. *Procedia Computer Science*, *93*, pp.967-974.

v. Kiran, Dasari, & Lokam Anjaneyulu. "Comparison of SVM classifier and wish art classifier on L- band alos-palsar-2 data over metropolitan area." *International Journal of Engineering & Technology* [Online], 7.3.29 (2018): 370-372.

vi. Kiran, Dasari, & Lokam Anjaneyulu Exploring the capability of C- band SENTINEL 1B data for Land cover classification water body mapping and oil spill detection, Journal of Advance Research in Dynamical and Control Systems (JARDCS), 2018 , 12 SP (2018): 359-363.

vii. Dasari, K. and Lokam, A "Comparison of C band RISAT-1 Dual-pol Vs Hybrid Pol data for Land cover classification" was communicated to the Journal of Applied Remote Sensing, ISSN: 1931-3195.

viii. Dasari, K. and Lokam, A "Comparison of Compact Polarimetry modes on L band Alos palsar quad pol data" was communicated to the Journal of Selected Topics on Applied Remote Sensing,

ix. Dasari, K. and Lokam, A Paper entitled “Polarimetric Synthesis of quad pol RISAT-1 data” was communicated to Advanced Electromagnetic Journal,.

x. Dasari, K. and Lokam, A "Comparison of Dual-pol and Hybrid pol of RISAT-1 data for Crop Identification" was communicated to the Journal of Remote Sensing".

xi. Dasari, K. and Lokam, A “ Exploring the capability of Hybrid polarimetry data for urban classification” will be communicated.

xii. Dasari, K. and Lokam, A, comparative study on L-band quad pol vs Hybrid pol vs Pseudo quad pol in the perspective of information content will be communicated to IEEE Transaction on Geoscience and Remote Sensing.

List of conferences

a) Dasari, K., Anjaneyulu, L., Jayasri, P.V. and Prasad, A.V.V., 2015, December. Importance of speckle filtering in image classification of SAR data. In *2015 International Conference on Microwave, Optical and Communication Engineering (ICMOCE)* (pp. 349-352). IEEE.

b) Dasari, K., Anjaneyulu, " The Significance of transmitting a circularly polarized component over a linear polarized component of RISAT-1 data for Landcover Classification" In 2019 POLinSAR Conference ESA, Italy, 2019.

c) Dasari, K., Anjaneyulu, L 2015, May, Feature Extraction and De speckling of SAR Image with K Mean Cluster Analysis. In *2015* International Conference "IEEE Indian Antenna Week" 2015 on May 30 - June 03 at Ajmer Rajasthan India.

d) Dasari, K., Anjaneyulu, L 2015, December, Estimating the Performance of Speckle Filters on RADARSAT-2 and ALOS PALSAR-2 Data . In 2014 the International Conference on Microwaves Antenna Propagation and Remote Sensing (ICMARS-14).